MODELLING THE INITIATION OF A HYDROTHERMAL ERUPTION – THE SHOCK TUBE MODEL

A THESIS PRESENTED IN PARTIAL FULFILMENT OF THE REQUIREMENTS FOR THE DEGREE OF

DOCTOR OF PHILOSOPHY
IN
MATHEMATICS

AT MASSEY UNIVERSITY, MANAWATU CAMPUS
NEW ZEALAND.

Luke Fullard

June 2011

Abstract

Modelling of hydrothermal eruption phenomenon has been a growing topic of research for the past 20 years. To date, models have focussed on the underground quasi-steady flow and on the above ground eruption jet including particle deposition. Very little has been able to be said about the first few seconds of an eruption, nor has much modelling work been done on eruption causes. In this thesis we develop a shock tube model for the initiation of a hydrothermal eruption which aims to answer some of the remaining questions about causality of a hydrothermal eruption.

The new shock tube model reported in this thesis is the first model able to simulate the initiation of a hydrothermal eruption. We take into account the three phases present during the eruption; in the geothermal reservoir below ground, liquid water and water vapour are present, in the above ground flow we also include air. The fact that the flow below ground is moving through a porous medium is accounted for, and new numerical methods using the finite volume framework are developed to solve the arising system of equations. Numerical simulations are described which simulate various eruptions, including ones with steam caps and rapidly developing cracks in the geothermal reservoir. Results from numerical simulations will be able to guide the design of future lab experiments of hydrothermal eruptions. The work of this thesis results in the first model able to simulate the initiation of a hydrothermal eruption.

Acknowledgements

- First and foremost I would like to express my appreciation for my chief supervisor Dr. Tammy Lynch. Thank you for everything! Thank you for providing such an interesting and meaty topic of research. I have learned an immense amount during the last few years and I attribute that to the excellent balance that you managed to strike between allowing me to branch out and explore various aspects of the modelling problem, and keeping me focused and on track to meet all of the goals that we had set. Thank you for your support and encouragement over the last few years, thank you for your guidance, and thank you for spending a lot of time proofing multitudes of reports, papers, and this thesis.

  I would also like to thank my secondary supervisor, Professor Robert McLachlan, for his help during my research, especially in the preparation of various academic papers.

- I extend my warmest thanks to the staff of the Institute of Fundamental Sciences, especially those in the Mathematics department. I could not have asked for a better place to complete my studies, both undergraduate and postgraduate. Thank you for the warm friendly atmosphere and the support you have all always given me. In addition, thank you for the opportunity to get involved with various extracurricular activities which have no doubt helped me to grow myself and my C.V.!

- Thank you to the many graduate and undergraduate students that I have had the pleasure of meeting and working with during the course of my studies. I would especially like to thank Dr. Dion O'Neale who was a PhD student at the beginning of my postgraduate study. Thank you Dion for all your Latex and computer help, and for being a great person to chat to in the hallways!

- A big thank you goes out to the New Zealand Institute of Mathematics and its Applications (NZIMA) for providing me with a scholarship for the first 3 years of my work. Without this support I doubt that I would have been able to successfully complete this work. Also, thank you to the Institute of Fundamental Sciences for various casual positions of employment during my entire student life.

- Thank you to the New Zealand Mathematical Society (NZMS), the Australia and New Zealand Industrial and Applied Mathematics society (ANZIAM), and the IFS postgraduate travel fund for providing financial assistance which allowed me to travel to various conferences and workshops in New Zealand and Australia. I feel that this was a critical part of my professional development.

- I would also like to thank everyone who attended any of my conference talks, especially those at the New Zealand Mathematics Colloquiums. The questions and suggestions given to me at these conferences have improved, and in some cases, provided some direction to my research project.

- Thank you Prof. Robert McLachlan of Massey University for useful discussions during the preparation of Chapter 4.

- For being my technical support go to guys, thank you Daniel Haselden and Daniel Walmsley.

- Thank you to my family. Mum and Dad, you have always been so supportive of me and have always encouraged me to do the best that I can. I am extremely grateful for all the love you have given me over the years and for helping me to grow into the man that I am today. Shaun, you have been a great brother. You are always good for a laugh and we have had some cool adventures together. Just remember, that even though you are bigger than me now, I can still take you! Laura, you always make me smile. I am very lucky to have such a great sister, I love you.

- Thank you to my other family, the members at Palmerston North Victory Christian Church, for all the good times, encouragements, and general support during the last few years. I especially thank my Pastor Joel Miller and my two best mates Ben and Micah.

- To my beautiful wife. Thank you for bringing a huge cheesy smile to my face! The last few months have been the best of my life and I look forward to spending the rest of my life with you. I love you more than you will ever know.

- Finally, thank you to the late Dr. Marijcke Vlieg-Hulstman who passed half way through my PhD studies. I will always remember her enthusiasm for teaching mathematics and the way that she was always keen for a good laugh or for a chat about the latest cricket matches. No matter how hard I tried, I could never get into work earlier than Marijcke! This thesis is dedicated to her memory.

...oh, and thank you to Yuki, for being the coolest little cat in the world!

Contents

List of Figures

List of Tables

Chapter 1

Introduction

Hydrothermal eruptions (sometimes also called hydrothermal explosions) are violent events which occur sporadically in many geothermal fields around the world, some of which are shown in Figure 1.1. They are characterised by the ejection of some solid material and a liquid-vapour water mixture (at or near boiling point conditions). In contrast to other types of eruptions, hydrothermal eruptions derive their energy solely from heat loss and phase changes, [17], which occur when the hydrothermal fluid is exposed to atmospheric pressure [42]. Using slightly modified definitions found in [22], [17], and [70], we make a distinction between hydrothermal eruptions and other ground water eruption types:

- Phreatic eruptions: an eruption which ejects water vapour, liquid water, and rock but no magma. This type of eruption is initiated when cooler groundwater comes to be in contact with a magmatic heat source causing rapid boiling. Examples of such eruptions are the Mount St Helens lava dome, USA, in 1983, where exsolved gas and solid debris were erupted, and the Halemaumau crater, Kiluea Volcano, Hawaii in 1924, where a crater was filled with groundwater following the drainage of a lava lake, see [45].

- Phreatomagmatic eruptions: similar to phreatic eruptions, but some magma is ejected. Houghton et. al. [33] discuss such eruptions at White Island, New Zealand.

- Magmatic-hydrothermal eruptions: in a pre-existing hydrothermal system magma heats the overlying groundwater, causing boiling and an eruption to initiate. In this case, magma may or may not be part of the ejecta. This type of eruption is known to have occurred in New Zealand in 1886, see [32], [63].

- Mixing Eruptions: volcanic debris, already erupted from a vent, contacts ground or surface water, causing a secondary eruption. Also known as a secondary hydroeruption. This type of eruption is known to have occurred in Alaska in 1912 following a volcanic eruption, see [1].

- Hydrothermal eruptions: like geysers, this type of eruption occurs in pre-existing hydrothermal fields with no immediate influence from magma (although the required energy for an eruption is derived from an igneous source deep in the geothermal reservoir, the heat is transferred to the upper layers of the reservoir by conduction and the convection of geothermal water). The authors of [22] believe all eruptions in Yellowstone National Park, USA, in the last $16,000$ years have had no direct influence from magma.

Figure 1.1: *A selection of areas of the world with a high amount of hydrothermal activity. From [70]*

Individual hydrothermal eruptions can last briefly (a few seconds), or as long as several hours and inevitably modify the surrounding area, creating large (sometimes hundreds of meters wide) craters, damaging nearby flora and fauna, and altering the underground flow processes of the containing geothermal field. This type of eruption differs from geyser activity since they are not cyclic and eject relatively large amounts of rock. Geysers eject only trace amounts of solid material and are recurring. Geyser theory and modelling was researched in [44]. Areas with active geothermal reservoirs where hydrothermal eruptions occur include the Taupo Volcanic Zone, New Zealand, Yellowstone National Park, USA, areas of Papua New Guinea, and Iceland. Such systems are not only of interest to study, but are important to

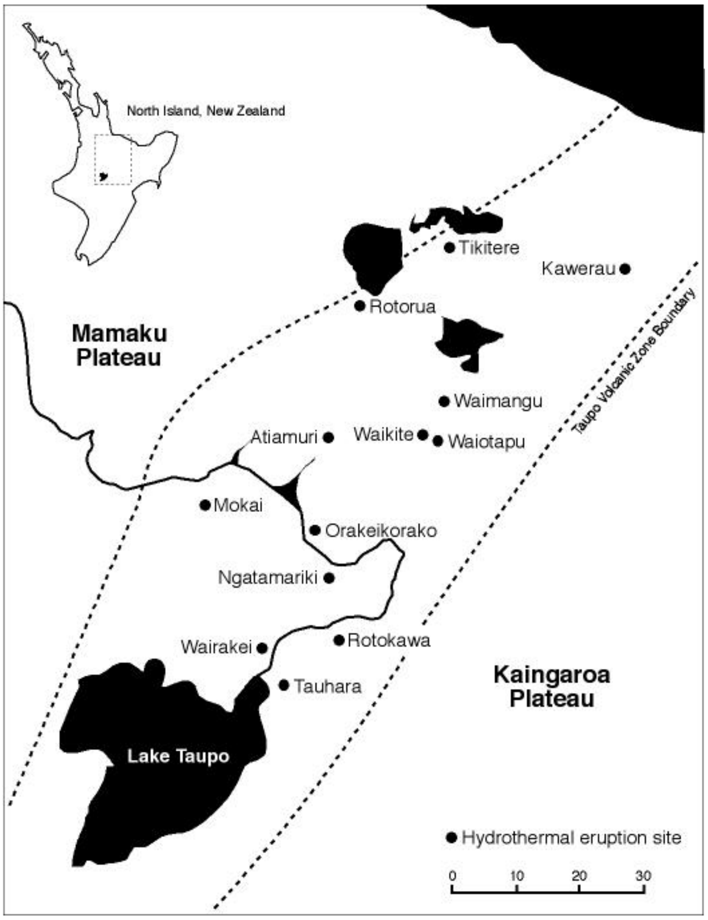

Figure 1.2: *Sites of hydrothermal eruptions in the Taupo Volcanic Zone, New Zealand. From [70].*

understand so that the potential dangers they pose may be identified and, where possible, eliminated, isolated, or minimised. Many geothermal fields are located close by, or in some cases directly underneath, suburban areas. New Zealand examples include Taupo, Rotorua, and areas of the Bay of Plenty, see Figure 1.2. This increases the risk of damage to public property, injury, and even death should an eruption occur in such a setting. An example of a hydrothermal eruption in a built up area is Kuirau Park (2001, 2006), Rotorua, where the eruption jet showered the local hospital with mud and debris thrown from the vent [10]. Furthermore, geothermal areas where hydrothermal eruptions are likely are often popular tourist attractions (for example, Craters of the Moon, Wairakei, NZ, and Yellowstone National Park, USA), where safety of the guests is of upmost importance. Also, in many geothermal areas of the world companies and governments extract energy from the rich underground resources, the Ladolam deposit on Lihir Island, Papua New Guinea is one example [17]. Eruptions in these areas can cause major damage to multi-million dollar plant equipment and pipelines.

This thesis aims to develop a new mathematical model capable of simulating the initiation of a hydrothermal eruption. Understanding how an eruption initiates will provide invaluable knowledge on factors affecting eruptions and could potentially be used to identify areas at a high risk of eruption.

Chapter 2

Literature Review: Eruption Modelling

The current chapter examines recent modelling of hydrothermal eruptions. The conceptual ideas surrounding these eruptions are detailed, as are the mathematical equations solved. Furthermore, a model of the initiation of volcanic eruptions using the shock tube model is discussed as a possible infrastructure to develop a similar model for hydrothermal eruptions.

2.1 Observations of Hydrothermal Eruptions

Due to the unpredictability of hydrothermal eruptions, few have been directly observed. Scientific observations of these events are limited since it is impossible to know when and where the next eruption might occur. Fournier et al. [58] describe changes in the geochemistry of the Porkchop Geyser leading up to the September 1989 hydrothermal eruption at Yellowstone National Park, USA. Various other observations of particular eruptions have been made including Lloyd and Keam [43], Scott and Cody [68], Allis [7] and Bruno et al. [18]. Furthermore, several historic examples have actually been caught on film, incuding Karapiti, NZ, in 1981, and at Waimangu, NZ, 1904 [54]. Investigations into prehistoric eruptions have examined various geological clues left behind by eruptions, such as crater size, shape, and ejected clasts. Browne and Lawless [17] provide an excellent summary of some of these eruptions. Muffler et al. [35] also examines evidence for hydrothermal eruptions at Yellowstone National Park, USA. Evidence for prehistoric hydrothermal eruptions can be difficult to analyse since more recent eruptions and other natural processes, such as glacial and fluvial actions, may modify the eruption area, see [35]. Recent NZ areas where hydrothermal eruptions have occurred include Mt Ruapehu, NZ, where a small hydrothermal eruption in 2006 caused the lake level to rise 1.3m, and Kuirau park, Rotorua, NZ, which had an eruption in 2001 and a further eruption in 2006 [10]. Two small hydrothermal eruptions occurred in 2007 in Rotorua, NZ, one at the Puarenga stream, the other at the former site of Malfroy's geyser in the Government gardens [11], and a hydrothermal eruption at Reporoa, NZ, in 2005 left a 50m crater in a scenic reserve. In 1981 a hydrothermal eruption was witnesed at the Taupo Pony Club, in the Tauhara Geothermal Field, NZ. The eruption jet was witnessed to reach heights of over 100m [68]. Allis [6] reports on various hydrothermal eruptions that have taken place at Craters of the Moon, Wairakei, NZ. Many of these eruptions are likely to have been induced by exploitation of the surrounding geothermal field. As such, understanding the mechanical process of naturally occuring hydrothermal eruptions will supply us with important information to reduce the risk of an eruption in areas of industrial geothermal development.

2.2 Hydrothermal Eruption Background - Causes and Thermodynamic Profiles

When evaluating causality of a hydrothermal eruption, it is clear that there is no one event that triggers every eruption. There are various mechanisms suggested in the literature [17], [22] which are described here:

- *Pressures exceeding lithostatic*: some sort of caprock is present which allows pressures in the geothermal reservoir to build until they exceed the weight and strength of the overlying rock.

- *Slow accumulation of steam and/or gas*: pressures may exceed lithostatic if steam is present in the system and can ascend, transmitting pressures to shallower regions. This mechanism is thought to be important in exploited geothermal fields.

- *Rapid subsurface pressure release*: a geothermal system that follows the *boiling point with depth* temperature (or pressure) relation may be triggered into an eruption by a sudden release of pressure (possibly caused by an earthquake, landslide, draining of lake, deglaciation, or hydrothermal fracturing) at depth, causing flashing of liquid water to water vapour. Such events are known to have occurred in Yellowstone National Park [22].

- *Progressive flashing*: considered to be the most common type of hydrothermal eruption [17]. The geothermal system is assumed to follow the *boiling point with depth* temperature (or pressure) profile, and an initiation event (similar to the rapid subsurface pressure release model) causes flashing of the liquid water to steam at or very close to the ground surface. There is then created a boiling front which propagates downwards, resulting in increased boiling, brecciation, and depressurisation of the underlying system. The lifting power of the created water vapour is what causes the solid material (soil, rocks, mud) to be ejected from a created eruption vent.

Since the progressive flashing model is deemed the most common cause of a hydrothermal eruption, it will be the focus of our modelling efforts.

Initiation triggers. Various eruption initiation mechanisms have been suggested in the literature. For a geothermal reservoir at or near boiling point conditions, (which is realistic according to Christiansen [22]), any sudden decrease of pressure on the system is potentially the trigger for a hydrothermal eruption [35]. Earthquake activity has been suggested to be a potenital candidate for this drop in pressure in [35], [77]. Suppose that a geothermal aquifer below the ground surface is at boiling point conditions. An earthquake may fracture the porous medium creating a crack that fills with vapour. This has the effect of transmitting higher pressures deep in the aquifer up to the surface causing flashing of the fluid and rapid soil and water ejection. Alternative mechanisms which have been proposed for a sudden pressure drop in a geothermal aquifer include a rapid fall in barometric pressure, rapid draining of a glacially dammed lake, the formation of a steam cap, rapid removal of overburden (i.e. during a landslide), large overpressures in the geothermal system, hydraulic fracturing of the geothermal reservoir, mineralisation of confining rocks, see [69], [34], [38], [54], [35], [15]. Evidence from geothermal fields, however, rule some of these mechanisms unlikely. Evidence for mineral deposition was not found in [24], large overpressures in a geothermal system were not found when measured in [54], and in [47] the effect of a gas phase was found to reduce the potential for a hydrothermal eruption. Nevertheless, it is evident that there are many situations in which an eruption could be triggered, the key commonality being a substantial drop in pressure.

Thermodynamic profile. The progressive flashing model requires the underlying fluid to follow the boiling point with depth temperature (or pressure) profile. Note that this fluid could be a mix of liquid water and water vapour, but for the purposes of our hydrothermal eruption model we assume that the underground fluid is initially fully liquid at boiling point conditions. In this situation, the pressure (and by thermodynamics, the temperature and boiling point) is dictated by the weight of the overlying surface and subsurface water. The boiling point with depth curve relies on the equation of state

$$T = T_{sat}(P).$$

The pressure gradient at boiling is given by

$$\frac{dP}{dz} = -\rho(T)g.$$

Clapeyron's equation provides $\left(\frac{dT}{dP}\right)_{sat}$, which is:

$$\left(\frac{dT}{dP}\right)_{sat} = \frac{\left(\frac{1}{\rho_v} - \frac{1}{\rho_l}\right)(T + 273.15)}{h_v - h_l}$$

where subscripts v and l denote vapour and liquid respectively. T is the temperature in degrees Celcius, P is the pressure, ρ the density, and h the enthalpy. g is the acceleration due to gravity. Hence the temperature gradient at saturated (boiling) conditions is

$$\frac{dT}{dz} = \left(\frac{dT}{dP}\right)_{sat} \frac{dP}{dz} = \left(\frac{dT}{dP}\right)_{sat} \left(-\rho_l \left(T_{sat}\right) g\right). \tag{2.1}$$

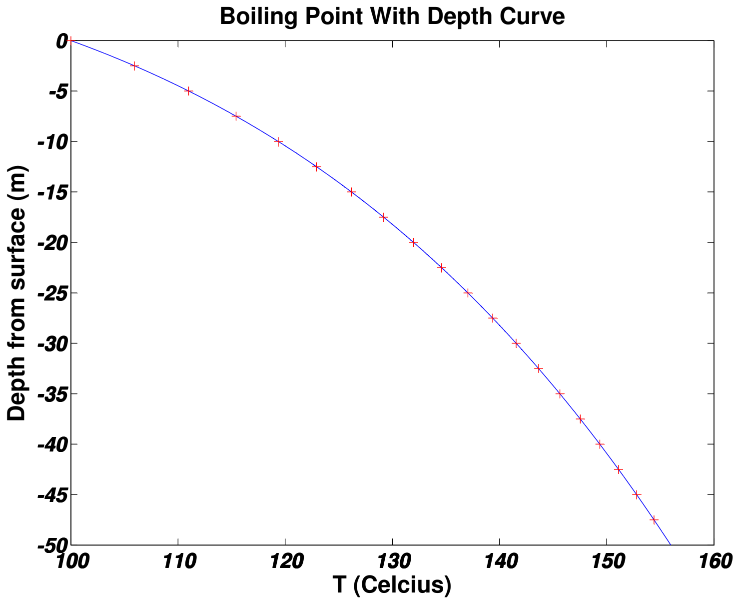

Figure 2.1: *The boiling point with depth temperature profile obtained by integration of equation 2.1.*

Figure 2.1 is obtained by numerical integration of Equation 2.1. This choice of thermodynamic profile is justified in [22] by measured temperatures obtained during drilling in an active area of Yellowstone National Park (see Figure 2.2). The drilling curve, Figure 2.2, shows good agreement with the boiling point with depth profile after around 80 feet. In shallower regions the temperature is significantly lower. This is common in geothermal fields and is likely due to cold water downflow (G. Weir, personal communication, October 4, 2011). This could explain why hydrothermal eruption phenomena are relatively rare, since for an eruption to occur the shallow aquifer water would need to be heated to boiling point or some triggering mechanism would have to cause a pressure reduction deeper in the geothermal aquifer where the fluid follows the boiling point with depth curve.

2.3 Previous Mathematical Modelling of Hydrothermal Eruptions

Prior to the work of McKibbin [46] hydrothermal eruptions were thought to have required large overpressures to produce such large eruptions. It has

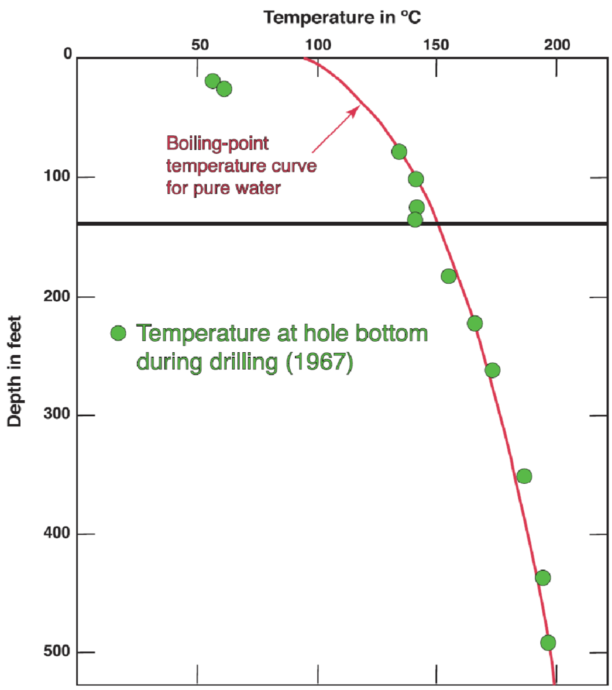

Figure 2.2: *Yellowstone National Park temperature drilling curve. Modified from [22].*

since been accepted that this is not the case, and that the progressive flashing model, as described in Section 2.2, is the most likely cause of a hydrothermal eruption [17]. The model does not require large overpressures, rather, it relies on forces created when liquid water flashes to water vapour. However, other mathematical models have been explored for hydrothermal eruptions. Muffler et al. [35] estimates the energy required for cratering using energy balance arguments. Mastin [45] also uses available energy estimates to approximate the magnitude of ejected materials and the spatial distribution of the debris. Scott [67] uses mass and energy balances to analyse changes in the thermodynamic state of a geothermal reservoir after a hydrothermal eruption. The first mechanistic mathematical model for a hydrothermal eruption was given in [46], the progressive flashing model for a hydrothermal eruption. This will be the topic of the next section of this thesis.

2.4 The Progressive Flashing Model for a Hydrothermal Eruption

The first mathematical model describing the mechanical process of a hydrothermal eruption was reported in McKibbin [46]. This and subsequent work with this model [14], [71], [70] have resulted in the progressive flashing model being regarded as the most likely cause of a natural hydrothermal eruption [17]. The mathematical model actually consists of two separate models, one for the below ground flow, and one for the above ground flow. The conceptual model of McKibbin [46], and the mathematical model for the below and above ground flow are given below.

2.4.1 Conceptual Model

The top down (progressive) flashing model was proposed by McKibbin [46] and subsequently developed in [14],[71],[70]. The model includes the following key mechanisms:

- In geothermal fields, a liquid or a two-phase mixture of water lies below the surface and is heated to boiling point conditions. The pressure and temperature follow a standard saturated pressure-temperature (boiling point with depth) curve.

- Due to an initiation event (discussed in Section 2.2) the saturated fluid is exposed to reduced pressure conditions.

- This pressure reduction allows boiling of the fluid to occur, and the fluid to expand.

- The fluid will move towards regions of lower pressure (the surface), and the movement of this fluid will provide lift to the rock above.

- When the cohesive and weight forces are exceeded by the lift provided by the fluid velocity, the eruption will break the surface and a column of vapour/liquid water mix will be ejected, taking some rock along with it.

- As the fluid and rock are ejected upwards, the depressurization path moves down further into the ground, causing the boiling front to move down further, and more material and fluid to be ejected.

- Some of the ejected material falls back into the eruption column and is re-ejected.

- This process will continue until some terminating mechanism occurs. This may include the hot water recharge running out, cold inflows from other parts of the aquifer, or the boiling front meeting an impermeable layer of rock.

The above assumptions are used to write a mathematical model of the situation. Smith [70] performed a physical experiment in a controlled laboratory environment to test the top down model. It was concluded that *pressure reduction at the surface may trigger an eruption and initiate a downwards-moving boiling front*, which is in agreement with the model.

2.4.2 Below Ground

The below ground flow model has been developed in [46],[14],[71],[70]. The work of this model was summarised in [50] where the model was also extended to two dimensional flow. The assumptions associated with this model (which are based on the conceptual model and thermodynamics) are as follows;

1. The principles of conservation of mass, momentum and energy hold, and are governed by the equations given further on in this Section.

2. The fluid below the flashing zone is motionless.

3. The fluid flowing is a homogeneous mixture of liquid water and water vapour. Due to the fact that the boiling processes occur rapidly, time is not available for the two separate phases to be established in their passage to the surface.

4. The moving fluid is at saturated (boiling) conditions.

5. The process is quasi-steady, that is, the eruption has already been initiated, and is currently in progress, and is modelled as being steady.

6. The fluid lifts particles at the surface, where conditions are atmospheric ($T = 100°C$).

7. Thermal conduction is ignored, i.e., there is no heat transfer between the fluid and rock in the flashing zone. The process is modelled as being adiabatic.

The technique used by McKibbin [46] was to set up all moving quantities relative to a moving reference frame (taken to be the velocity of the so-called flashing front). In this reference frame the flow was assumed to be steady. The above assumptions were coupled with Darcy's law for a fluid flowing through a porous medium, and the conservation of mass, momentum, and energy to produce the following set of equations:

$$V_f = -\frac{k}{\epsilon \mu_f}\left(\frac{dP}{dz} + \rho_f g\right), \tag{2.2}$$

where

$$\frac{dP}{dz} = -\rho_f g - \frac{\mu_f \epsilon V}{k}\left(\frac{\rho_{fd}}{\rho_f} - 1\right). \tag{2.3}$$

V_f is the fluid velocity in the porous medium, V is the velocity of the flashing front, k is the relative permeability of the porous medium, ϵ the porosity of the porous medium, μ_f the dynamic viscosity of the fluid, P the pressure, ρ_f the fluid density, ρ_{fd} the fluid density at the flashing front depth, and g the acceleration due to gravity. The thermodynamic condition that the fluid is at saturation point also permits us to write down a further ODE for a pressure temperature relation;

$$\left(\frac{dT}{dP}\right)_{sat} = \frac{\left(\frac{1}{\rho_v} - \frac{1}{\rho_l}\right)(T + 273.15)}{h_v - h_l}, \tag{2.4}$$

where T is the fluid temperature, ρ_l the liquid water density, ρ_v the water vapour density, h_v the water vapour enthalpy, and h_l the liquid water enthalpy. Once the pressure P and temperature T have been found (by integration of Equations 2.3 and 2.4), we can find all other thermodynamic quantities due to relevant relations found in [62].

Replenishment of ejected water. Smith [70] studied how a geothermal reservoir will recover after the event of a hydrothermal eruption. Two-dimensional isothermal flow equations were used and it was found that the ejected water was replaced by local sources. More details can be found in [70].

2.4.3 Above Ground

In McKibbin and Smith[49] the authors formulated a mathematical model for the fountain of boiling water and rock particles ejected from a hydrothermal eruption. This work was summarised in [50]. The flow was assumed to be a column of circular horizontal cross-section with a vertical axis, see Figure 2.3. As the column of ejected boiling water rises it entrains some of the surrounding air, leading to slowing and cooling of the flow. Furthermore, the speed of the components (liquid water, water vapour, air) were assumed to be at the same velocity (well mixed). Initially, the column of ejected material issues from the ground from a circular region of radius r_0 and entrains air from the surrounding atmosphere at temperature T_a. The jet rises vertically and grows in radius ($r(z)$) at height z above the ground surface. The flow is modelled as being at steady state. The equations of motion are then presented; the conservation of mass gives

$$\frac{dM}{dz} = 2\pi r \rho_{atm} E(w), \tag{2.5}$$

where M is the upwards mass flux given by $M = \rho \pi r^2 w$. ρ , ρ_{atm} are the fluid density and atmospheric density respectively. $r(z)$ is the jet radius at height z. $w(z)$ is the mean vertical speed of the flow. $E(w)$ is the volume entrainment rate per unit surface area of the column, modelled by

$$E(w) = kw(w/w_0)^n, \tag{2.6}$$

where k and n are dimensionless parameters. The subscript 0 indicates values at $z = 0m$ (the ground surface). The conservation of momentum equation is given by

$$\frac{d(Mw)}{dz} = -\rho_a \pi r^2 g, \tag{2.7}$$

where the subscript a denotes the entrained air phase, and g is the acceleration due to gravity. The energy conservation equation accounts for changes in the kinetic and internal energy of the flow;

$$\frac{d(1/2Mw^2 + M_l u_l + M_v u_v + M_a u_a)}{dz} = \rho\pi r^2 gw + \frac{dM_a}{dz} u_{atm}. \tag{2.8}$$

Here the subscripts l, v, a denote the liquid water, water vapour, and air phases respectively. u_i are the specific internal energies of the various phases. By numerically solving the equations in the above model, McKibbin and Smith found that the radius of the column increases with height due to entrainment, and the velocity decreased with height due to gravitational and inertial slowing. Also, the model was used to predict the release height and settling speed of particles from the column. For in depth results and equations, see [49], [48].

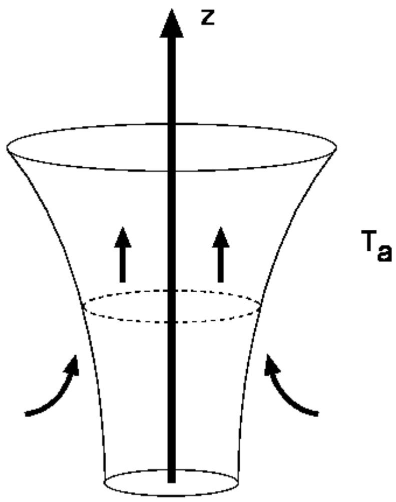

Figure 2.3: *Geometry of the above ground flow. From [49].*

2.5 Volcanic Modelling

The field of explosive volcanic eruptions is an extensively researched area. In recent times, one of the leading researchers in this area has been a mathematical modeller, Kenneth Wohletz. In [79], [78], Wohletz proposes a model for explosive (particularly Plinian) volcanic eruptions based on the Navier-Stokes equations for two-phase compressible flow (with some simplifications).

The use of this model allows for the presence of shock and rarefaction waves. Wohletz [78] describes the initiation of the modelled eruption:

> *Assuming that a high-pressure magma chamber is separated from the atmosphere prior to eruption and that there is a nearly instantaneous failure of the rock overburden capping the chamber, an initial blast phase is predictable using shock tube theory.*

The similarities between an initiation of this type of volcanic eruption and the conceptual model (see 2.4.1) are immediately apparant. Other authors have attempted to use the shock tube model to describe the process of a volcanic eruption [53], [5], [36], [37]. We believe it is possible to use an adapted shock tube model to describe the two-phase flow of liquid water and water vapour in a porous medium as seen in a hydrothermal eruption. In particular, we believe that this type of model may be able to provide us with valuable information about initiation processes for hydrothermal eruptions. Shock tube model theory will be the topic of the next subsection of this report.

2.5.1 The Shock Tube Model and the Euler Equations

The shock tube mathematical model has had many applications in a range of fields in recent times, including volcanic eruption modelling [36], [79], combustion modelling [23], and modelling flashing (boiling) fluid flow [55], [66]. Often, standard shock tube numerical experiments are used to validate numerical codes [65], [64].

The simplest case of a shock tube consists of a horizontal tube with a diaphragm in the center of the tube separating the driver section (region of higher pressure) from the driven section (region of lower pressure). See Figure 2.4. The fluid in the sections need not be the same. At some time t_0 the diaphragm is removed and the flow is allowed to evolve. By the nature of the problem, thermodynamic properties are not smooth everywhere (at the diaphragm, before t_0, the pressure 'jumps' and there exists no derivative there). This poses numerical difficulties which will be addressed in Section 3.1. The resulting flow profile will depend on the nature of the equations governing the fluid/s.

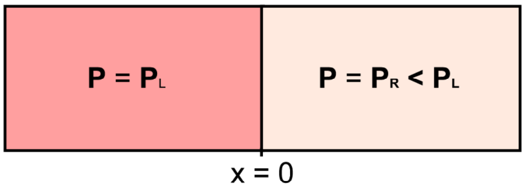

Figure 2.4: *Diagram of the shock tube. Two chambers at different pressures are separated by a diaphragm at position $x = 0$.*

The Euler Equations. The most commonly used equations to describe compressible fluid flow for shock tube type problems are the Euler equations. The Euler equations are derived in [72] and [21] and consist of three conservation equations, one for mass, momentum, and energy respectively. The Euler equations must be augmented with an appropriate equation of state for the fluid. They are a simplification of the Navier-Stokes equations in that they do not take into account viscosity. The equations are

$$\mathbf{U}_t + \mathbf{F}_x = \mathbf{0}, \tag{2.9}$$

where

$$\mathbf{U} = \begin{bmatrix} \rho \\ \rho u \\ \rho E \end{bmatrix}, \tag{2.10}$$

and

$$\mathbf{F} = \begin{bmatrix} \rho u \\ \rho u^2 + P \\ \rho u E + uP \end{bmatrix}. \tag{2.11}$$

This system of partial differential equations is used in many $1D$ fluid flow (including shock tube) models. $\mathbf{U}$ is called the vector of conserved variables. $\mathbf{F}$ is the vector of fluxes. ρ, u, P, E are defined as the fluid density, velocity, pressure, and total energy respectively. Note that $E = e + \frac{1}{2}u^2$, where e is the specific internal energy. The Euler Equations 2.9, are a set of non-linear hyperbolic partial differential equations. The Jacobian matrix, given by

$$A(\mathbf{U}) = \frac{\partial \mathbf{F}}{\partial \mathbf{U}}, \tag{2.12}$$

has 3 real eigenvalues and 3 corresponding eigenvectors (the definition of hyperbolic) given in [72] as

$$\lambda_1 = u - c, \ \lambda_2 = u, \ \lambda_3 = u + c, \tag{2.13}$$

where c is the sound speed in the fluid. In recent years most studies have focused on models which are formally hyperbolic. Complex characteristics cause the equations to become ill-posed. That is, they cause the governing PDEs to not be evolutionary so that with initial data the solution is not determined for all time. The eigenvalues (also known as characteristics due to their importance in solving PDEs along characteristic curves) of a system are physically relevant in fluid dynamics problems, since they represent the speed at which information in the system propagates.

The Riemann Problem

Recall that the simplest case of a shock tube consists of a horizontal tube with a diaphragm in the center of the tube separating a region of higher pressure from a region of lower pressure. Unless the pressures on each side of the diaphragm are equal, there will be a discontinuous jump in the fluid pressure (and possibly the density and/or velocity). This initial value problem is often called the *Riemann Problem.* The Riemann problem consists of a set of PDEs (such as 2.9) and an initial value problem with discontinuous initial conditions. Mathematically,

$$\left.\begin{array}{lr} \text{PDE:} & \mathbf{U}_t + \mathbf{F}_x = \mathbf{0}, \\ \text{IC:} & \mathbf{U}(x,0) = \mathbf{U}_0(x) = \begin{cases} \mathbf{U}_L & x < 0, \\ \mathbf{U}_R & x > 0, \end{cases} \end{array}\right\} \tag{2.14}$$

There is no exact closed-form solution to the Riemann problem for the Euler equations, instead it must be solved numerically. This will be discussed in Section 3.1, since the solution will be important in building numerical methods to solve the shock tube problem.

Chapter 3

Literature Review: Basic Numerical Methods

Simulation of a hydrothermal eruption model based on the shock tube principle requires the development of advanced numerical recipes. This is due to the fact that a three phase flow (air, water vapour, and liquid water) is occurring in two regions: 1) above the ground (atmospheric flow), and 2) below the ground, in a porous geothermal reservoir. The method must also take into account phase change between the liquid water and the water vapour. Chapters 4 - 5 discuss the development of the necessary numerical schemes. The current Section reviews the literature which forms the basis for these numerical schemes which the author researched in preparation of this thesis.

3.1 The Finite Volume Method

The Euler Equations 2.9 and their multi-phase analogue (see Section 4.1) are a system of hyperbolic PDEs. It is worth noting however that this differential form is not the most natural expression of these equations. They are derived from the following integral equations (for the 1-D case):

$$\frac{d}{dt}\int_{x_L}^{x_R}\mathbf{U}(x,t)dx = \mathbf{F}(\mathbf{U}(x_L,t)) - \mathbf{F}(\mathbf{U}(x_R,t)), \tag{3.1}$$

which is the integral form of the conservation law. The PDEs of 2.9 can be recovered from 3.1 by first rewriting 3.1 as

$$\frac{d}{dt}\int_{x_L}^{x_R}\mathbf{U}(x,t)dx = -\mathbf{F}(\mathbf{U}(x,t))\Big|_{x_L}^{x_R}. \tag{3.2}$$

Next, if we assume that $\mathbf{U}$ and $\mathbf{F}$ are smooth functions, we may write

$$\frac{d}{dt}\int_{x_L}^{x_R} \mathbf{U}(x,t)dx = -\int_{x_L}^{x_R} \frac{\partial}{\partial x}\mathbf{F}(\mathbf{U}(x,t))dx, \tag{3.3}$$

which can then be expressed more simply as

$$\int_{x_L}^{x_R} \left[\frac{\partial}{\partial t}\mathbf{U}(x,t) + \frac{\partial}{\partial x}\mathbf{F}(\mathbf{U}(x,t))\right] dx = 0. \tag{3.4}$$

Since this integral must be zero for all x_R and x_L, then the integrand must be identically zero,

$$\frac{\partial}{\partial t}\mathbf{U}(x,t) + \frac{\partial}{\partial x}\mathbf{F}(\mathbf{U}(x,t)) = 0. \tag{3.5}$$

The derivation of the differential form relied upon the assumption that $\mathbf{U}$ and $\mathbf{F}$ are sufficiently smooth functions. However, in an IVP with discontinuities such as the Riemann problem, the integral form of the equation is more natural, as pointed out by Toro [72], since the derivation of the governing equations is based on physical conservation principles expressed as integral relations on control volumes. The integral formulation requires less smoothness of the solution, which paves the way to extending the class of admissible solutions to include discontinuous solutions. The integral formulation also forms the foundation of *finite volume* methods. In one spatial and one time dimension we can construct a grid by splitting the spatial domain into $N_x = \frac{L_x}{\Delta x}$ intervals, where N_x is the number of intervals, L_x is the total length of the spatial domain, and Δx is the length of the cell. We then split the time domain analogously with $N_t = \frac{L_t}{\Delta t}$. We define the i'th grid cell on any particular time level by $C_i = (x_{i-1/2}, x_{i+1/2})$. Using this definition, the length of the cell becomes $\Delta x = x_{i+1/2} - x_{i-1/2}$. In each of the grid cells (the "finite volumes") we may define $\mathbf{Q}_i^n$ as the average value of a function u over the i'th interval at time t_n, given by the formula

$$\mathbf{Q}_i^n \approx \frac{1}{\Delta x}\int_{x_{i-1/2}}^{x_{i+1/2}} \mathbf{U}(x,t_n)dx \equiv \frac{1}{\Delta x}\int_{C_i} \mathbf{U}(x,t_n)dx. \tag{3.6}$$

Numerical Conservation Form. An extremely important property of a numerical method for compressible flow problems is that the method be *conservative*, since this class of methods can be used to accurately calculate shock waves. The sum $\sum_{i=1}^{N_x} \mathbf{Q}_i^n \Delta x$ approximates the integral in Equation

3.6 over the entire interval $[a, b]$. If we use a method which is in *numerical conservation form* (defined below), then this discrete sum will change only due to fluxes at the boundaries $x = a$ and $x = b$. Therefore, the variables $\mathbf{U}$ will be preserved in the interval, provided that the correct boundary conditions are applied. The integral form of the conservation law over any cell C_i can be found from Equation 3.1:

$$\frac{d}{dt}\int_{C_i} \mathbf{U}(x,t)dx = \mathbf{F}(\mathbf{U}(x_{i-1/2},t)) - \mathbf{F}(\mathbf{U}(x_{x_i+1/2},t)), \tag{3.7}$$

which we can integrate over one timestep (of length $\Delta t = t_{n+1} - t_n$) to approximate $\mathbf{Q}_i^{n+1}$. Integrating from t_n to t_{n+1} yields

$$\int_{C_i} \mathbf{U}(x,t_{n+1})dx - \int_{C_i} \mathbf{U}(x,t_n)dx = \int_{t_n}^{t_{n+1}} \mathbf{F}(\mathbf{U}(x_{i-1/2},t))dt - \int_{t_n}^{t_{n+1}} \mathbf{F}(\mathbf{U}(x_{i+1/2},t))dt.$$

Rearranging, and dividing by Δx gives

$$\begin{aligned}\frac{1}{\Delta x}\int_{C_i} \mathbf{U}(x,t_{n+1})dx =& \frac{1}{\Delta x}\int_{C_i} \mathbf{U}(x,t_n)dx \\ &- \frac{1}{\Delta x}\left[\int_{t_n}^{t_{n+1}} \mathbf{F}(\mathbf{U}(x_{i+1/2},t))dt - \int_{t_n}^{t_{n+1}} \mathbf{F}(\mathbf{U}(x_{i-1/2},t))dt\right].\end{aligned} \tag{3.8}$$

Numerical methods which mimic the Property 3.8 are said to be in *numerical conservation form.* The spatial integrals are exactly of the form 3.6, hence 3.8 tells us how the cell average of $\mathbf{U}$ should be updated in one time step. It also suggests studying numerical methods of the form

$$\mathbf{Q}_i^{n+1} = \mathbf{Q}_i^n - \frac{\Delta t}{\Delta x}\left(\boldsymbol{F}_{i+1/2}^n - \boldsymbol{F}_{i-1/2}^n\right), \tag{3.9}$$

where $\boldsymbol{F}_{i-1/2}^n$ is an approximation to the average flux along $x = x_{i-1/2}$;

$$\boldsymbol{F}_{i-1/2}^n \approx \frac{1}{\Delta t}\int_{t_n}^{t_{n+1}} \mathbf{F}((x_{i-1/2},t))dt. \tag{3.10}$$

Notice that Equation 3.9 can be rearranged into a finite difference type form

$$\frac{\mathbf{Q}_i^{n+1} - \mathbf{Q}_i^n}{\Delta t} + \frac{\boldsymbol{F}_{i+1/2}^n - \boldsymbol{F}_{i-1/2}^n}{\Delta x} = 0.$$

3.1.1 Godunov's Method (a first order method)

Godunov [30] proposed a new numerical scheme for conservation equations which utilised the solution of the Riemann problem. A basic assumption of the method is that at any given time level t_n the data has a piece-wise constant distribution of the form 3.6. That is, we split the domain into grid cells of width Δx, calculate the average value of $\mathbf{U}(x, t_n)$ in the cell, then model the domain as in Figure 3.1 using the cell averages as the piece-wise constant data. Since now we can view the data at time level t_n to be pairs of

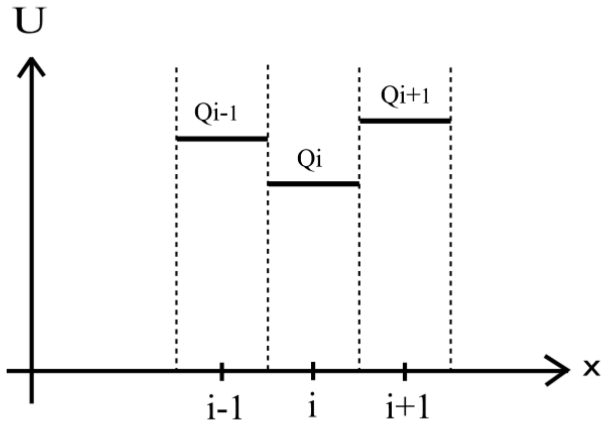

Figure 3.1: *A graphical representation of the Godunov scheme. The domain is split into discrete cells, then the value of the function in each cell is taken to be constant and to be the cell average. Modified from [72].*

constant states $(\mathbf{Q}_i^n, \mathbf{Q}_{i+1}^n)$ separated by a discontinuity at the cell interface (at $x_{i+1/2}$), we can define a local Riemann problem

$$\begin{aligned} PDE: \quad & \mathbf{U}_t + \mathbf{F}_x = 0, \\ IC: \quad \mathbf{U}(x,0) = \mathbf{U}_0(x) = & \begin{cases} \mathbf{Q}_i^n & \text{if } x < 0, \\ \mathbf{Q}_{i+1}^n & \text{if } x > 0. \end{cases} \end{aligned} \tag{3.11}$$

We can find the approximation to the average flux

$$\boldsymbol{F}_{i-1/2}^n = \frac{1}{\Delta t} \int_{t_n}^{t_{n+1}} \mathbf{F}(\mathbf{U}^n(x_{i-1/2}, t))dt. \tag{3.12}$$

The flux $\mathbf{F}$ is calculated using the value of $\mathbf{U}$ at the cell boundary $x_{i-1/2}$, which is found by solving the Riemann problem there. The solution to this Riemann problem will be discussed in Section 3.1.2. The function $\boldsymbol{F}_{i+1/2}^n$ can be found in an analogous way to 3.12. The average value of $\mathbf{U}$ can now be updated using the formula 3.9.

In summary, we can implement the following algorithm for the IVP 2.14 with Godunov's method for a single time step:

- Define a mesh of cells C_i, and cell averages using 3.6.
- Solve the Riemann problems $RP(\mathbf{U}_{i-1}^n, \mathbf{U}_i^n)$ and $RP(\mathbf{U}_i^n, \mathbf{U}_{i+1}^n)$ to find $\boldsymbol{F}_{i\pm 1/2}(0)$.
- Use Equation 3.9 to update the cell averages.

It should also be noted that a restriction on the time step for Godunov's method is

$$\Delta t \leq \frac{\Delta x}{S_{max}^n}, \tag{3.13}$$

where S_{max}^n is the maximum wave velocity in cell C_i at time t_n. This condition ensures that wave interaction does not occur within cells, see [72], [40].

3.1.2 Approximate Riemann Solver

The application of Godunov's method requires the solution of the Riemann problem. This can be done using *Riemann solvers.* The most popular solvers are those due to Roe [61], HLL, and HLLC. We will use the HLLC solver due to its simplicity, accuracy, and the fact that it is widely used in the literature [29], [12], [28], [51], [57]. These solvers attempt to directly approximate the flux function $\mathbf{F}_{i\pm 1/2}$ then evolve the system using Equation 3.9. All these methods may be extended to higher order.

The HLLC Solver. The HLLC (Harten, Lax, van Leer - Contact) solver was originally designed to restore missing contact waves from the HLL solver [73]. The HLLC method relies on estimates of a left wave speed S_L, a right wave speed S_R, and a middle wave speed, S_*. The left, right, and middle wave speeds are essentially the eigenvalues of the system, hence they are the speed at which information is propagating through the system. In the case of the Euler equations, 2.9, the left wave is a rarefaction wave where all thermodynamic properties vary smoothly, the right wave is a shock wave where all thermodynamic properties are discontinuous, and the middle wave is found to be a contact discontinuity where the pressure and velocity are constant, but the density may jump discontinuously, see [72]. These waves separate four states at the boundary of each cell, $\mathbf{U}_L$, $\mathbf{U}_{*L}$, $\mathbf{U}_R$, and $\mathbf{U}_{*R}$, see Figure 3.2. The Riemann solution in this case is given by

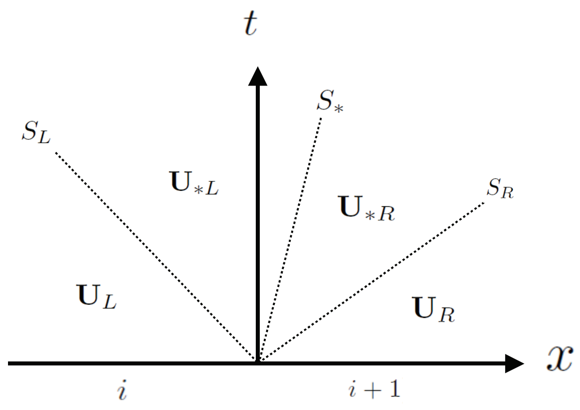

Figure 3.2: *A graphical representation of the domain in the HLLC method. Three waves separate four constant states. Modified from [72].*

$$\tilde{\mathbf{U}}(x,t) = \begin{cases} \mathbf{U}_L & \text{if} \quad x/t \leq S_L, \\ \mathbf{U}_{*L} & \text{if} \quad S_L \leq x/t \leq S_*, \\ \mathbf{U}_{*R} & \text{if} \quad S_* \leq x/t \leq S_R, \\ \mathbf{U}_R & \text{if} \quad x/t \geq S_R, \end{cases} \tag{3.14}$$

where

$$\begin{aligned} \mathbf{U}_{*L} = & \quad \frac{1}{\Delta t(S_R - S_L)} \int_{\Delta t S_L}^{\Delta t S_*} \mathbf{U}(x, \Delta t) dx, \\ \mathbf{U}_{*R} = & \quad \frac{1}{\Delta t(S_R - S_L)} \int_{\Delta t S_*}^{\Delta t S_R} \mathbf{U}(x, \Delta t) dx. \end{aligned} \tag{3.15}$$

The associated numerical flux can be shown to be

$$\mathbf{F}^{hllc}_{i+1/2} = \begin{cases} \mathbf{F}_L & \text{if} \quad 0 \leq S_L, \\ \mathbf{F}_{*L} & \text{if} \quad S_L \leq 0 \leq S_*, \\ \mathbf{F}_{*R} & \text{if} \quad S_* \leq 0 \leq S_R, \\ \mathbf{F}_R & \text{if} \quad 0 \geq S_R, \end{cases} \tag{3.16}$$

where

$$\begin{aligned} \mathbf{F}_{*L} = & \quad \mathbf{F}_L + S_L(\mathbf{U}_{*L} - \mathbf{U}_L), \\ \mathbf{F}_{*R} = & \quad \mathbf{F}_R + S_R(\mathbf{U}_{*R} - \mathbf{U}_R). \end{aligned} \tag{3.17}$$

Toro gives the definition for the $\mathbf{U}_{*k}$ states in [72]:

$$\mathbf{U}_{*k} = \rho_k \left(\frac{S_k - u_k}{S_k - S_*} \right) \begin{bmatrix} 1 \\ S_* \\ E_k + (S_* - u_k) \left[S_* + \dfrac{P_k}{\rho_k \left(S_k - u_k \right)} \right] \end{bmatrix}. \tag{3.18}$$

For either the HLL or HLLC methods, the wave speeds must be approximated.

Wave Speed Estimates. Various methods of estimating the wave speeds for the HLLC solver have been proposed and are largely problem specific [72]. A simple (and robust) choice for left and right wave speeds of the Euler equations is given by

$$S_L = min \left(u_L - c_L, u_R - c_R \right), \quad S_R = max \left(u_L + c_L, u_R + c_R \right) \tag{3.19}$$

where i is the phase and c is the speed of sound in phase i. The middle wave speed S_* is derived in [72] as:

$$S_* = \frac{P_R - P_L + \rho_L u_L \left(S_L - u_L \right) - \rho_R u_R \left(S_R - u_R \right)}{\rho_L \left(S_L - u_L \right) - \rho_R \left(S_R - u_R \right)}. \tag{3.20}$$

This choice of middle wave speed is widely used in the literature (see for example [3], [29], [57], [51]). Once calculated, the HLLC numerical flux can be substitued into Equation 3.9.

3.2 New Model Goals

Based on the work done previously in the literature on modelling both hydrothermal and volcanic eruptions and the associated numerical methods used to solve the arising equations as presented in Sections 2.2 - 3.1.2, we propose the following research goals:

- Create a shock tube based model for the initiation of a hydrothermal eruption. This is a novel approach in hydrothermal eruption modelling, and the governing equations will be similar to the multiphase Euler equations. Such a model should be able to simulate the initiation of a hydrothermal eruption for a certain set of initial conditions, and also combine the above and below ground flow into a single mathematical model. Both these outcomes would be a new development in the field.

- Develop the numerical methods necessary to solve the equations governing the new shock tube model. This will require the ability to solve a three-phase flow (water vapour, liquid water, and air) in a porous medium, as well as being able to quantify the amount of liquid water boiled to water vapour in a given time-step.

- Simulate the onset of a hydrothermal eruption for various pressure conditions. The model should be able to 'predict' the necessary pressure drop at the air-water interface to initiate an eruption. Simulations will provide important information into what characteristics of the reservoir (porosity, permeability etc.) increase the chances of an eruption. Furthermore, the model should be able to predict the rate of ejection of material, as well as the make up of an eruption jet, the rate at which a boiling front travels into the reservoir, and also the rate of 'erosion' of the porous medium as an eruption continues. This information is invaluable when considering what areas are at higher risk of a hydrothermal eruption, and what physical processes drive an eruption.

- Assess how alternative reservoir conditions may affect hydrothermal eruptions. Such alternatives include the presence of a steam cap, or a rapidly developing crack in the geothermal reservoir. These conditions have been suggested as being relevant to hydrothermal eruptions in reservoirs where a large gas phase is expected to be present.

Achieving these goals will significantly contribute to the understanding of hydrothermal eruption phenomenon. In this thesis, the new shock tube based mathematical model, and the associated numerical methods and simulations are outlined. Chapters 4 - 6 present the newly developed numerical methods to solve the arising equations, Chapter 8 advances these methods to handle flow through a porous medium. Chapters 7 and 9 describe the simulations that were performed and their results, while in Chapter 10 we draw conclusions from these findings and outline potential future work.

Chapter 4

Multi-Phase Flow Equations and Methods

There has been much work done on simulating natural physical phenomenon using multi-phase flow equations, see, for example, [60], [55], [79]. This has led to a multitude of numerical methods which may be used to solve such systems. In the case of the initiation of natural hydrothermal eruptions, the discontinuous thermodynamic profiles (e.g. pressure, temperature) demand that we use appropriate numerical methods, able to handle shock waves. Chapter 3 discusses the basic methods used in literature to achieve this. The contents of the current Chapter discuss the appropriate governing equations (Section 4.1), a two-phase flow solver from the literature (Section 4.3), and the three-phase solver, developed during the course of the current research (Section 4.4). The new method is then checked using appropriate test cases (Section 4.5).

4.1 Multi-Phase Flow Model

The development of multiphase mixture models has revolutionized mathematical modelling of flows. Powers ([23], [56], [31]) points out that two-phase continuum mixture models have been extensively used to model reactive gas dynamics in heterogeneous mixtures. One of the more well known models in this area is that of Baer and Nunziato [9]. The novelty of this model is that it is able to handle a two-phase compressible flow with separate pressures and velocities for each of the fluid and solid phases. In pure fluid zones the model tends to the single phase Euler equations. The model can also account for compaction of the porous material, chemical reactions, and interphase momentum and energy exchange due to drag. Some models have been derived from the Baer-Nunziato model which use a single pressure and velocity (e.g. [39]). Due to its compatability with the Euler equations and the shock tube model, we adopt and adapt the formulations of Baer-Nunziato, and also the assumptions which accompany the model. These assumptions are:

- The mixture can be split into discrete components (or phases). Each of the components behave as if it were a single material except when it is interacting (exchanging mass, momentum, and energy) with the other phases.
- Conservation equations for each component are written resembling one phase equations, but contain phase interaction terms, not present in one phase models.
- Each component i has an associated volume fraction, $\phi_i = \dfrac{v_i}{\sum_j v_j}$, where v_k is the volume of phase k within any given cell.
- The sum of the volume fractions is one ($\sum_i \phi_i = 1$), i.e there are no void spaces present.
- The modelling PDEs are evolutionary so that the initial-boundary value problem is well posed, see [56].

Using the above assumptions we can derive (such as in [27]) for each fluid component j, the equations for 1-D horizontal multi-phase flow (excluding interphase transfer terms):

$$\frac{\partial}{\partial t}(\phi_j \rho_j) + \frac{\partial}{\partial x}(\phi_j \rho_j u_j) = 0 \tag{4.1}$$

$$\frac{\partial}{\partial t}(\phi_j \rho_j u_j) + \frac{\partial}{\partial x}\left(\phi_j \rho_j u_j^2 + \phi_j P_j\right) = P_I \frac{\partial \phi_j}{\partial x} \tag{4.2}$$

$$\frac{\partial}{\partial t}(\phi_j \rho_j E_j) + \frac{\partial}{\partial x}(\phi_j \rho_j u_j E_j + \phi_j u_j P_j) = P_I V_I \frac{\partial \phi_j}{\partial x} \tag{4.3}$$

Equation 4.1 models the conservation of mass of phase j, Equation 4.2 the conservation of momentum, and Equation 4.3 the conservation of energy.

The physical parameters are the same as those for the Euler equations from Equation 2.9, that is, u, ρ, P, E denote the fluid velocity, density, pressure, and total energy. ϕ is the volume (sometimes called void) fraction. The terms P_I and V_I are called the interface variables, where P_I is the interface pressure, and V_I the interface speed. These two variables, along with the right hand side spatial derivative terms in the momentum and energy equations ($P_I \frac{\partial \phi_j}{\partial x}$ and $P_I V_I \frac{\partial \phi_j}{\partial x}$) will be discussed below.

We may write a further equation which models the evolution of the volume fraction, ϕ_j, of each phase. This equation is derived in [27], [4], by considering a test function equal to 1 in phase j and 0 elsewhere and is commonly used in multi-fluid models.

$$\frac{\partial}{\partial t}\phi_j + V_I \frac{\partial}{\partial x}\phi_j = 0. \tag{4.4}$$

Equation 4.4 is called the compaction equation, and is discussed below.

Compaction Equation. Equation 4.4 is called the dynamic compaction equation (so called because of its use in combustion-compaction modelling). This equation expresses the evolution of the volume fraction and was derived in [27]. Powers [56] points out that the compaction equation has proved able to (1) capture observed compaction phenomena, (2) prevent initial and initial/boundary value problems from being ill-posed (i.e. from being elliptic), and (3) ensure that any entropy inequalities are satisfied. The equation implies that in the absense of interphase transfer terms (for example, boiling) the volume fraction of each phase will advect with the interface speed, V_I, hence will be constant in this frame of reference. Note, however, that in the case of a hydrothermal eruption the volume fraction of each phase will change due to boiling of the liquid water. This effect will be discussed in a further chapter. To ensure we have the correct number of equations for the number of variables, this equation is augmented with the relation

$$\sum_j \phi_j = 1.$$

Nozzling Terms The presence of so called *nozzling terms* ($P_I \frac{\partial \phi_j}{\partial x}$ and $P_I V_I \frac{\partial \phi_j}{\partial x}$) on the right hand side of the momentum and energy equations,

Equations 4.2 and 4.3 respectively, render the system non-conservative. Hence, the system cannot be represented in the form of Equation 3.8. The use of this nozzling term is left out by some authors (see [31] and his references), but the terms are included by others (e.g. [13], [75], [23]). Powers [31] justifies not using the nozzling terms by pointing out that:

- satisfaction of the strong form of the second law of thermodynamics (which the nozzling terms guarantee) may be overly restrictive,
- nozzling does not significantly affect low-pressure compaction waves,
- we are able to avoid mathematical and numerical difficulties in the analysis of shocks associated with models having a non-conservative form.

Bdzil [13] justifies the use of nozzling terms physically by noting that the change in porosity on the continuum scale acts as a nozzle that can either accelerate or decelerate a flow, and drive relative motion between the phases. In a more recent paper, Powers [56] points out that the use of the nozzling terms can capture experimentally observed phenomena, and can prevent initial and initial/boundary value problems from being ill posed. Vreman [75] shows that the nozzling terms do not contribute to entropy. Andrianov [8] goes further and gives an example where the flow is uniform with respect to velocity and pressure only when the nozzling terms are included. In another of Abgrall's papers [3] it is noted that this term must be present since when a shock enters a mixture zone the volume fraction must change as the shock speed is different in the different phases. In Liou's paper [20] the authors show that the nozzling terms arise naturally in a stratified flow regime. In this report, the nozzling terms will be included in the analysis. We justify the use of these terms physically by appealing to the fact that volume fractions of the different phases will differ in adjoining cells. If the velocities of the phases in the adjoining cells also differ then there will be a force applied as the fluid is 'squeezed' into the volume occupied by the other cell. In addition, hydrothermal eruptions occur in porous media. The porosity of this medium will change (especially when the fluid exits the medium, which is the case when an eruption breaks the ground surface) hence the fluids will be 'nozzled'. Furthermore, when the pressures of all phases are equal, the nozzling term corresponds to the PdV work one phase does on the others when the internal phase interface varies and changes the volume fraction. The physical justification for these terms is expanded on in [65], [13].

The interface pressure P_I and velocity V_I are given in [64] by

$$\begin{aligned} P_I &= \sum_j \phi_j P_j, \\ V_I &= \frac{\sum_j \phi_j \rho_j u_j}{\sum_j \phi_j \rho_j}. \end{aligned}$$

These expressions are approximations to the pressure and speed at the interface of different phases. This particular form of P_I is justified since for uniform flow ($P_i = P_j$ and $u_i = u_j$ for all fluids i and j) the interface pressure must be the fluid pressure, $P_I = P_j$. A useful analogy is the concept of the partial pressure. If we consider the fluid pressure of fluid j with volume fraction ϕ_j, the partial pressure of fluid j is $pp_j = \phi_j P_j$. The total pressure of the mixture of all fluids in the control volume is the sum of the partial pressures, hence $P = \sum_j \phi_j P_j$.

4.1.1 Energy/Entropy Equation

Drela et al. [26], and Toro [72] show that we can write a further equation for the conservation of entropy by combining the mass, momentum, and energy equations of the Euler equations. The result is Equation 4.5, where s_j is the specific entropy of phase j.

$$\frac{\partial}{\partial t}\left(\phi_j \rho_j s_j\right) + \frac{\partial}{\partial x}\left(\phi_j \rho_j u_j s_j\right) = 0. \tag{4.5}$$

Equation 4.5 implies that the entropy of each phase of fluid advects with the flow. This relation has been used to reduce spurious losses in [26]. This relation will prove useful later in this report when we solve the flow equations with phase change between the fluids.

4.2 Multi-Phase Flow Methods

The multi-phase compressible Euler Equations 4.1 - 4.4 have been used to model a variety of interesting and important physical flows (see [59], [56],

[51], [27] for example). The resulting non-linear hyperbolic system is solved using sophisticated numerical methods which have been developed over a number of years. Note that the system is hyperbolic except in choked flow conditions, that is when $u_1 \pm c_1 = u_2$ [25]. A recent advance in the numerical treatment of multi-phase flows has been that of stratified methods (see [19], [4], [20], [41]). These methods are a new way to deal with two-phase flows efficiently and accurately. Equations 4.1-4.3 can be written in vector form, with the vector of conserved variables for a system of j fluid phases given by

$$\mathbf{Q} = \begin{bmatrix} \phi_j \rho_j \\ \phi_j \rho_j u_j \\ \phi_j \rho_j E_j \\ \\ \phi_{j-1} \rho_{j-1} \\ \phi_{j-1} \rho_{j-1} u_{j-1} \\ \phi_{j-1} \rho_{j-1} E_{j-1} \\ \vdots \\ \phi_1 \rho_1 \\ \phi_1 \rho_1 u_1 \\ \phi_1 \rho_1 E_1 \end{bmatrix}. \tag{4.6}$$

For the same system of j fluid phases, the vector of fluxes is given by

$$\mathbf{F} = \begin{bmatrix} \phi_j \rho_j u_j \\ \phi_j \rho_j u_j^2 + \phi_j P_j \\ \phi_j \rho_j E_j u_j + \phi_j u_j P_j \\ \\ \phi_{j-1} \rho_{j-1} u_{j-1} \\ \phi_{j-1} \rho_{j-1} u_{j-1}^2 + \phi_{j-1} P_{j-1} \\ \phi_{j-1} \rho_{j-1} E_{j-1} u_{j-1} + \phi_{j-1} u_{j-1} P_{j-1} \\ \vdots \\ \phi_1 \rho_1 u_1 \\ \phi_1 \rho_1 u_1^2 + \phi_1 P_1 \\ \phi_1 \rho_1 E_1 u_1 + \phi_1 u_1 P_1 \end{bmatrix}, \tag{4.7}$$

and the right hand sides of the system can be written as a Lagrangian flux

$$\mathbf{F}_{LAG} = \begin{bmatrix} 0 \\ \left(P_I \dfrac{\partial \phi_j}{\partial x}\right)_j \\ \left(P_I V_I \dfrac{\partial \phi_j}{\partial x}\right)_j \\ \\ \\ 0 \\ \left(P_I \dfrac{\partial \phi_{j-1}}{\partial x}\right)_{j-1} \\ \left(P_I V_I \dfrac{\partial \phi_{j-1}}{\partial x}\right)_{j-1} \\ \\ \vdots \\ 0 \\ \left(P_I \dfrac{\partial \phi_1}{\partial x}\right)_1 \\ \left(P_I V_I \dfrac{\partial \phi_1}{\partial x}\right)_1 \end{bmatrix}. \tag{4.8}$$

We can now discretise our system of equations using the finite volume framework. We split the spatial domain into $N_x = \dfrac{L_x}{\Delta x}$ intervals, where N_x is the number of intervals, L_x is the total length of the spatial domain, and Δx is the length of the cell. We then split the time domain analogously with $N_t = \dfrac{L_t}{\Delta t}$. We define the i'th grid cell on any particular time level by $C_i = (x_{i-1/2}, x_{i+1/2})$. Using this definition, the length of the cell becomes $\Delta x = x_{i+1/2} - x_{i-1/2}$. Therefore, the discretised system at time level n is given by

$$\mathbf{Q}_i^{n+1} = \mathbf{Q}_i^n - \frac{\Delta t}{\Delta x}\left(\mathbf{F}_{i+1/2}^n - \mathbf{F}_{i-1/2}^n\right) - \frac{\Delta t}{\Delta x}\mathbf{F}_{LAG,i}^n. \tag{4.9}$$

4.3 The Two-Phase Solver

Saurel and LeMetayer [65] discuss the use of numerical methods to solve compressible multi-fluid flows. They note that the methods in the literature all have deficiencies, especially methods which are not based on two-phase flow equations (i.e. methods that try to solve a 'mixture' fluid with a mixture equation of state). A recent and useful development in modelling multi-phase flows has been that of stratified methods. Several authors ([19], [20], [4], for example) report on a way of splitting a system with two sets of conservation laws, one for each phase of a two-phase system, into two systems of conservation laws with the solution to each of the two systems found independently of the other. This method has been found to be useful, since simple numerical methods (e.g. the HLLC solver of [72]) can be used on the individual phase systems and each phase maintains its own equation of state (no mixture equation is required). See [19], [20], [4] for more details. In the case of hydrothermal eruptions we have two phases (liquid and vapour) of water. In this specific case, the conservation equations, Equations 4.1 - 4.4, for each phase will be solved independently of the others and then the coupling will be dealt with separately, see Chapter 5. In Figure 4.1 we see a graphical representation of the stratified configuration. Two adjacent cells, C_i and C_{i+1} contain a mixture of the two phases (in this case a liquid and a gas phase) with void fractions $\phi_{l,i}$, $\phi_{g,i}$, $\phi_{l,i+1}$, $\phi_{g,i+1}$. There are four possible inter-cell interactions, depending on the void fraction in each cell 1) liquid-liquid, 2) liquid-gas, 3) gas-liquid, 4) gas-gas. Each interaction has a weight $\omega_{k,j}$, with $k, j = 1, 2$ defined as follows

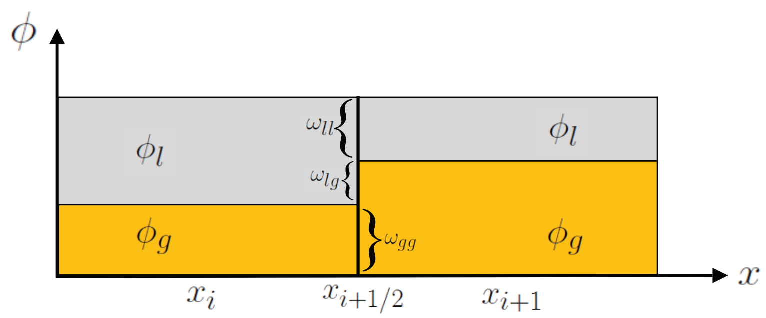

Figure 4.1: *Graphical representation of the stratified method for computing multiphase flows. In each cell each phase has weights according to the volume fraction in that cell and its neighbouring cell. Adapted from [19].*

$$\begin{aligned} \omega_{11} &= \min\{\phi_{l,i}\ , \quad \phi_{l,i+1}\}\ , & \omega_{21} &= \max\{0\ , \quad \phi_{g,i} - \phi_{g,i+1}\}\ , \\ \omega_{12} &= \max\{0\ , \quad \phi_{l,i} - \phi_{l,i+1}\}\ , & \omega_{22} &= \min\{\phi_{g,i}\ , \quad \phi_{g,i+1}\}\ , \end{aligned} \tag{4.10}$$

with the conditions $\omega_{12} \times \omega_{21} = 0$. This condition is necessarily true in each cell since the volume fraction of one of the phases must be greater or equal to the other, and $\omega_{11} + \omega_{12} + \omega_{22} + \omega_{21} = 1$, which accounts for the fact that the sum of the volume fractions, ϕ_i, must equal one in each cell. We can now compute the intercell flux

$$\mathbf{F}_{i+1/2} = \omega_{11}\mathbf{F}^{(11)}_{i+1/2} + \omega_{12}\mathbf{F}^{(12)}_{i+1/2} + \omega_{22}\mathbf{F}^{(22)}_{i+1/2} + \omega_{21}\mathbf{F}^{(21)}_{i+1/2}, \tag{4.11}$$

where $\mathbf{F}^{(L,J)}_{i+1/2}$ is the interstate flux from the corresponding Riemann problem (Equation 4.12) for a single phase system which is solved using an appropriate Riemann solver (e.g. the HLLC solver).

$$\begin{aligned} &\mathbf{U}_t + \mathbf{F}_x = \mathbf{0}, \\ &\mathbf{U}(\mathbf{x}, \mathbf{0}) = \begin{cases} \mathbf{Q}_L = \mathbf{Q}_{k,i} & \text{if} \quad x < x_{i+1/2}, \\ \mathbf{Q}_R = \mathbf{Q}_{j,i+1} & \text{if} \quad x > x_{i+1/2}. \end{cases} \end{aligned} \tag{4.12}$$

The initial data $\mathbf{Q}_{k,i}$ and $\mathbf{Q}_{j,i+1}$ with $k, j = g, l$ are the single phase conservation equations. For example, if we had a system of six conservations laws, three equations for each of two phases, we would define for cell i

$$\mathbf{Q}_i = \begin{bmatrix} \phi_g\rho_g \\ \phi_g\rho_g u_g \\ \phi_g\rho_g E_g \\ \phi_l\rho_l \\ \phi_l\rho_l u_l \\ \phi_l\rho_l E_l \end{bmatrix}_i \implies \begin{array}{l} \mathbf{Q}_{g,i} = \begin{bmatrix} \rho_g \\ \rho_g u_g \\ \rho_g E_g \end{bmatrix}_i \\ \mathbf{Q}_{l,i} = \begin{bmatrix} \rho_l \\ \rho_l u_l \\ \rho_l E_l \end{bmatrix}_i \end{array}.$$

The superscript (L, J) in Equation 4.11 is determined by the contact wave velocity, S_*, and the value of k, j in the above (single phase reduced) Riemann problem of Equation 4.12. The value of the superscript (L, J) is given by Table 4.1 below.

Table 4.1: L superscript

k (cell i)	j (cell $i+1$)	L, J
g	g	22
l	l	11
l	g	12 if $S_*^{(l,g)} > 0$
l	g	21 if $S_*^{(l,g)} < 0$
g	l	12 if $S_*^{(g,l)} < 0$
g	l	21 if $S_*^{(g,l)} > 0$

The middle wave speed, S_* is given in [72] as

$$S_* = \frac{P_R - P_L + \rho_L u_L(S_L - u_L) - \rho_R u_R(S_R - u_R)}{\rho_L(S_L - u_L) - \rho_R(S_R - u_R)}. \tag{4.13}$$

Hence for the situation where we have liquid in the left cell (cell i) and gas in the right cell (cell $i+1$), $S_*^{(l,g)}$ (and analogously $S_*^{(g,l)}$) becomes

$$S_*^{(l,g)} = \frac{P_g - P_l + \rho_l u_l(S_L - u_l) - \rho_g u_g(S_R - u_g)}{\rho_l(S_L - u_l) - \rho_g(S_R - u_g)}, \tag{4.14}$$

where the liquid variables are calculated in cell i and the gas variables in cell $i+1$. Once the intercell flux, $\mathbf{F}_{i+1/2}$, has been calculated using Equation 4.11 it will be used in Equation 4.9 to advance the system in time.

4.3.1 Calculating the Two Phase Nozzling terms, F_{LAG}

Recall that the discretised system of equations to be solved at time level n is given by

$$\mathbf{Q}_i^{n+1} = \mathbf{Q}_i^n - \frac{\Delta t}{\Delta x}\left(\mathbf{F}_{i+1/2}^n - \mathbf{F}_{i-1/2}^n\right) - \frac{\Delta t}{\Delta x}\mathbf{F}_{LAG,i}^n,$$

which is Equation 4.9. Calculating the nozzling terms, F_{LAG}, in Equation 4.9 can be done analogously to the flux. The treatment of the F_{LAG} terms is derived in [3] using Rankine-Hugoniot relations. For more information on the Rankine-Hugoniot relations see [72]. This treatment of the F_{LAG} terms differs from [19] but is closer to the discrete equations method of [4], [3]. Let the function

$$\operatorname{sign}(x) = \begin{cases} 1 \text{ if } x > 0 \\ -1 \text{ if } x < 0 \\ 0 \text{ if } x = 0 \end{cases} . \tag{4.15}$$

For the gas phase (liquid phase can be found analogously):

$$\begin{aligned} \left(\mathbf{F}_{LAG,i}\right)_g = \ & M_i^{lg} \times \omega_{12}\mathbf{U}_i^{12} - M_i^{gl} \times \omega_{21}\mathbf{U}_i^{21} + \\ & + m_{i-1}^{lg} \times \omega_{12}\mathbf{U}_{i-1}^{12} - m_{i-1}^{gl} \times \omega_{21}\mathbf{U}_{i-1}^{21}, \end{aligned} \tag{4.16}$$

where

$$\mathbf{U}_i^{12} = \mathbf{U}_i^{12}\left(\mathbf{Q}_i^{(l)}, \mathbf{Q}_{i+1}^{(g)}\right) = \begin{bmatrix} 0 \\ P_{I^*}^{(l,g)} \\ \left(P_{I^*}V_{I^*}\right)^{(l,g)} \end{bmatrix}_i \mathbf{U}_i^{21} = \mathbf{U}_i^{21}\left(\mathbf{Q}_i^{(g)}, \mathbf{Q}_{i+1}^{(l)}\right) = \begin{bmatrix} 0 \\ P_{I^*}^{(g,l)} \\ \left(P_{I^*}V_{I^*}\right)^{(g,l)} \end{bmatrix}_i \tag{4.17}$$

and

$$M^{lg} = max\left(0, \operatorname{sign}\left(S_*^{(a,v)}\right)\right), \qquad m^{lg} = min\left(0, \operatorname{sign}\left(S_*^{(a,v)}\right)\right).$$

The terms $P_{I^*}^{(l,g)}$, $\left(P_{I^*}V_{I^*}\right)^{(l,g)}$, and their (g,l) equivalents, are calculated in [3] and [72] (see Toros' treatment of the HLLC flux for the Euler equations) and are simply stated here as

$$\left[P_{I^*}^{(l,g)}\right]_i = \left[\rho_l\left(S_*^{(l,g)} - u_l\right)(S_L - u_l) + P_l\right]_i, \tag{4.18}$$

$$\left[P_{I^*}^{(l,g)}V_{I^*}^{(l,g)}\right]_i = \left[\left(\rho_l\left(S_*^{(l,g)} - u_l\right)(S_L - u_l) + P_l\right)S_*^{(l,g)}\right]_i, \tag{4.19}$$

where the liquid variables are calculated in cell i and the gas variables in cell $i+1$ (for the (l,g) case)). $S_*^{l,g}$ is given by Equation 4.14, S_L and S_R are given in [72] by:

$$S_L = min\left(u_L - c_L, u_R - c_R\right), \quad S_R = max\left(u_L + c_L, u_R + c_R\right). \tag{4.20}$$

The sign functions in Equation 4.16 account for the direction of the flux transfer (from cell i to $i+1$ or vice versa). Note that the Lagrangian flux, $\mathbf{F}_{LAG,i}$, is dependant on information from cells $i-1$, i, and $i+1$ respectively since the terms in Equations (4.18) and (4.19) depend on the left and right states at the cell boundary. This ensures that the method is symmetric when dealing with negative velocities. Once the intercell flux of Equation 4.11 and F_{LAG} of Equation 4.16 are found, they can be substituted into Equation 4.9 to advance the time of the system.

4.3.2 Two Phase Volume Fraction Evolution

The evolution of the volume fraction, Equation 4.4, is not directly derived in [19]. However we may use the method described in [4] and [3]. The reader is referred to these references for the derivation, here we simply present the volume fraction evolution scheme for a two-phase flow (without relaxation terms).

$$\frac{\partial \phi_l}{\partial t} = \frac{1}{\Delta x}\begin{bmatrix} M_i^{lg} \times \omega_{12} S_*^{(l,g)} - M_i^{gl} \times \omega_{21} S_*^{(g,l)} + \\ +m_{i-1}^{lg} \times \omega_{12} S_*^{(l,g)} - m_{i-1}^{gl} \times \omega_{21} S_*^{(g,l)} \end{bmatrix}. \tag{4.21}$$

This evolution algorithm can be used to update the volume fraction for phase l in a given timestep. The evolution of phase g can be calculated analogously, or simply found using $\phi_g = 1 - \phi_l$. Also note that since Equation (4.14) depends on the left and right states at the boundary, Equation (4.21), the volume fraction evolution equation, depends on information from cells $i-1$, i, and $i+1$ respectively. Again, this ensures that the method is symmetric when dealing with negative velocities.

In summary, the stratified method can be used as a simplification to the whole system by first calculating the weights $\omega_{j,k}$ $(j,k = 1,2)$, then calculating $\mathbf{F}_{i+1/2}^{(1,1)}$ and $\mathbf{F}_{i+1/2}^{(2,2)}$ by solving the associated single phase Riemann problem, and finally by solving the two phase reduced Riemann problem under the conditions given in Table 4.1.

4.4 The Three Phase Solver

In Section 4.3 a method to solve two-phase flows was introduced where the system is split into weighted smaller systems. This method was based upon the research of [19], [4], [20], [41]. We propose here a new method which is an extension of the previous two-phase method to three-phase flow.

4.4.1 Calculating the Three Phase Weights

Consider a flow with three distinct phases: 1, 2, and 3 respectively. As in the two-phase method we may assign a weight, ω_{xx}, to each interaction. It is the form of these weights which is the new work of this section. In the case of a three-phase flow we have 9 such interactions; three self-interactions (1-1, 2-2, 3-3), and six interactions between phases (1-2, 2-1, 1-3, 3-1, 3-2, 2-3). Each of these interactions has an assigned weight.

Self Interactions. The self-interactions are defined in a similar way to the two-phase method:

$$\begin{aligned}
\omega_{11}^i &= \min\{\phi_{1,i}\ ,\ \phi_{1,i+1}\}\,, \\
\omega_{22}^i &= \min\{\phi_{2,i}\ ,\ \phi_{2,i+1}\}\,, \\
\omega_{33}^i &= \min\{\phi_{3,i}\ ,\ \phi_{3,i+1}\}\,,
\end{aligned} \tag{4.22}$$

for all cells i. The ω subscripts represent the interactions (e.g. 11 in a 1-1 interaction). The ϕ subscripts represent the phase and the cell (e.g $\phi_{x,i}$ is the void fraction of phase x in cell i). The interactions between fluids are more tricky.

Separate Fluid Interactions. Consider an interaction between phase 1 in cell i and phase 3 in cell $i+1$. For there to be any interaction between the phases in the neighbouring cells there must be a common border at the cell wall (the effective length of this common border is the weight ω_{13}), see Figure 4.2. The two necessary conditions for this common border to exist for

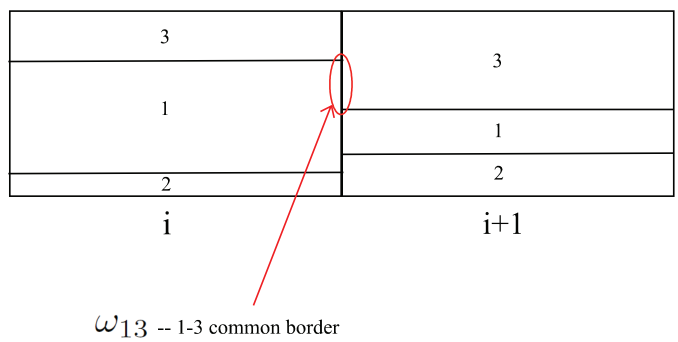

Figure 4.2: *The* 1-3 *common border.*

a 1-3 interaction are given mathematically by $\phi_{1,i} > \phi_{1,i+1}$ and $\phi_{3,i+1} > \phi_{3,i}$, that is, phase 1 in cell i has a border on the right of the cell where it is able to 'donate' or 'receive' flux to or from phase 3, and phase 3 in cell $i+1$ has a border on the left of the cell where it is able to 'donate' or 'receive' flux to or from phase 1. Furthermore, the middle wave speed (as defined in Equation (4.23)) determines which is the donating phase and which is the receiving phase. Should the middle wave speed be positive then the phase in the left cell i is the donating phase and the phase in the right cell $i+1$ is the receiving phase. For a negative middle wave speed the roles of the phases are reversed. Table 4.2 below shows the necessary conditions for a common border to exist between two different phases. S^*_{xy} is the middle wave speed between phases

Table 4.2: Conditions for a common border between phases

Interaction cells $(i, i+1)$	Condition 1	Condition 2
$1, 3$	$\phi_{1,i} > \phi_{1,i+1}$	$\phi_{3,i+1} > \phi_{3,i}$
$3, 1$	$\phi_{3,i} > \phi_{3,i+1}$	$\phi_{1,i+1} > \phi_{1,i}$
$1, 2$	$\phi_{1,i} > \phi_{1,i+1}$	$\phi_{2,i+1} > \phi_{2,i}$
$2, 1$	$\phi_{2,i} > \phi_{2,i+1}$	$\phi_{1,i+1} > \phi_{1,i}$
$2, 3$	$\phi_{2,i} > \phi_{2,i+1}$	$\phi_{3,i+1} > \phi_{3,i}$
$3, 2$	$\phi_{3,i} > \phi_{3,i+1}$	$\phi_{2,i+1} > \phi_{2,i}$

x in cell i and y in cell $i+1$ and is given in [72] by

$$S^*_{xy} = \frac{P_y - P_x + \rho_x u_x (S_L - u_x) - \rho_y u_y (S_R - u_y)}{\rho_x (S_L - u_x) - \rho_y (S_R - u_y)}, \tag{4.23}$$

which is Equation 4.13 with the left cell L (cell i) being fluid x and the right cell R (cell $i+1$) being fluid y. S_L and S_R are the left and right wavespeeds respectively and are given in [72] by Equation 3.19

$$S_L = min\left(u_x - c_x, u_y - c_y\right), \quad S_R = max\left(u_x + c_x, u_y + c_y\right).$$

If for any interactions between two different fluids the conditions in Table 4.2 are met (the two fluids share a common border), then there will be a transfer of flux from one cell to the other. We now need to quantify the value of the weight function ω_{xy} between fluids x and y.

Consider a fluid x in cell i which has a border we will call X_i on the right of the cell to donate or receive flux to or from the other two fluids y and z in cell $i+1$. The relative length of the interaction border X_i is equal to the sum of the relative lengths of the interaction borders Y_{i+1} and Z_{i+1} (note that any of these borders may have length zero), see Figure 4.3.

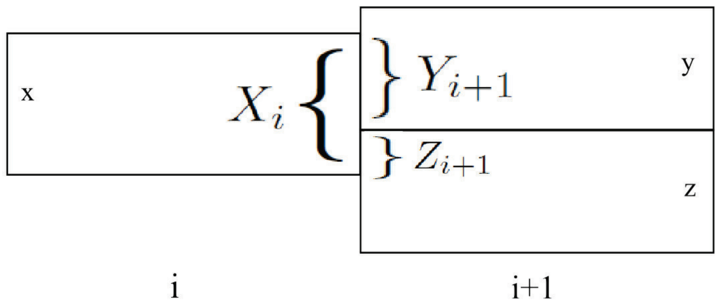

Figure 4.3: *Interaction borders for fluids x, y, and z.*

Therefore, assuming a positive middle wave speed, if we want to find the weight between fluids x and y we simply subtract fluid z's interaction border from the total donating border. That is, $Y_{i+1} = X_i - Z_{i+1}$. Stated mathematically, let $\Omega^{I+}_{x,i}$ be the length of fluid x's interaction border on the right hand side of cell i and let $\Omega^{I-}_{y,i+1}$ be the length of fluid y's interaction border on the left hand side of cell $i+1$.

$$\Omega^{I+}_{x,i} = \max(0\ ,\ \phi_{x,i} - \phi_{x,i+1}), \tag{4.24}$$

$$\Omega^{I-}_{y,i+1} = \max(0\ ,\ \phi_{y,i+1} - \phi_{y,i}). \tag{4.25}$$

With this definition we can finally define the weights ω^i_{xy}. We must make a distinction between cells which satisfy the appropriate conditions in Table 4.2 and those which do not. If the conditions in Table 4.2 are not met for any cell i, then the weight function for that cell is set at zero. Furthermore, we must account for the sign of the middle wave speed. Consider an interaction between fluids x in cell i and y in cell $i+1$. We assume that the conditions of Table 4.2 for a common border to exist are met and we define the interaction border lengths as in Equations (4.24) and (4.25). We also define the middle wave speed, S^*_{xy} as in Equation (4.23). If this middle wave speed is positive there will be a donation of flux from phase x in cell i to phase y in cell $i+1$ and the interaction weight will be defined as

$$\omega^{i+}_{xy} = \Omega^{I+}_{x,i}\left(\frac{\Omega^{I-}_{y,i+1}}{\Omega^{I-}_{z,i+1} + \Omega^{I-}_{y,i+1}}\right). \tag{4.26}$$

However, if the middle wave speed is negative then the donating phase becomes y in cell $i+1$ which donates to phase x in cell i and the interaction weight becomes

$$\omega_{xy}^{i-} = \Omega_{y,i+1}^{I-} \left(\frac{\Omega_{x,i}^{I+}}{\Omega_{x,i}^{I+} + \Omega_{z,i}^{I+}} \right). \tag{4.27}$$

The physics of the situation requires that the weight, ω_{xy}^{i}, must be symmetric in terms of direction of flow (i.e. the length of the interacting border must be the same regardless of if we have a positive or negative middle wave speed). Hence, we must have

$$\omega_{xy}^{i+} = \omega_{xy}^{i-} \quad \Rightarrow \quad \Omega_{x,i}^{I+} \left(\frac{\Omega_{y,i+1}^{I-}}{\Omega_{z,i+1}^{I-} + \Omega_{y,i+1}^{I-}} \right) = \Omega_{y,i+1}^{I-} \left(\frac{\Omega_{x,i}^{I+}}{\Omega_{x,i}^{I+} + \Omega_{z,i}^{I+}} \right), \tag{4.28}$$

which is true if and only if

$$\Omega_{z,i+1}^{I-} + \Omega_{y,i+1}^{I-} = \Omega_{x,i}^{I+} + \Omega_{z,i}^{I+}. \tag{4.29}$$

To prove this relation, consider that the sum of the interaction borders on the right of cell i must be equal to the sum of the interaction borders on the left of cell $i+1$, that is

$$\Omega_{x,i}^{I+} + \Omega_{y,i}^{I+} + \Omega_{z,i}^{I+} = \Omega_{x,i+1}^{I-} + \Omega_{y,i+1}^{I-} + \Omega_{z,i+1}^{I-}. \tag{4.30}$$

Since we are calculating the weight for the $x-y$ interaction, we assumed that the associated relations of Table 4.2 were satisfied. This implies that $\Omega_{x,i}^{I+} \neq 0$ and $\Omega_{y,i+1}^{I-} \neq 0$. Therefore, by the same relations of Table 4.2, $\Omega_{x,i+1}^{I-} = 0$ and $\Omega_{y,i}^{I+} = 0$. Hence we find that

$$\Omega_{x,i}^{I+} + \Omega_{z,i}^{I+} = \Omega_{y,i+1}^{I-} + \Omega_{z,i+1}^{I-} \tag{4.31}$$

which completes the proof that $\omega_{xy}^{i+} = \omega_{xy}^{i-}$.

The definition for the weight between fluids x and y is then possible and is given by

$$\omega_{xy}^{i} = \begin{cases} 0 \quad \text{if} \quad \text{Table 4.2 conditions unsatisfied} \\ \Omega_{x,i}^{I+} \left(\dfrac{\Omega_{y,i+1}^{I-}}{\Omega_{z,i+1}^{I-} + \Omega_{y,i+1}^{I-}} \right) \quad \text{otherwise,} \end{cases} \tag{4.32}$$

which is symmetric with respect to the middle wave speed. The definition of the weights given by Equation 4.32 gives a geometrical interpretation of their form. The bracketed term is between 0 and 1 (since $\Omega^{I-}_{y,i+1}$ cannot be negative) and represents the fraction of phase y in cell $i+1$ available for interaction with fluids in cell i. When this bracketed term is multiplied by the fraction of available flux in cell i, $\Omega^{I+}_{x,i}$, the resulting weight, ω^{i}_{xy}, can be considered the probability that fluid x in cell i will donate or receive flux to or from fluid y in cell $i+1$. This definition is new and is a natural definition for the weight functions since fluids with larger receiving interaction borders have a higher probability of interacting with the donating fluid. Furthermore, this definition has some attractive properties:

- It is a necessary condition that the value of each individual weight is between 0 and 1. Since the volume fraction for every phase is between 0 and 1 in every cell, $\Omega^{I+}_{x,i}$ and $\Omega^{I-}_{y,i+1}$ are also between 0 and 1 for all fluid phases x and y and all cells i. Furthermore, from the definition of the weights in Equation (4.32), $0 \leq \omega^{i}_{xy} \leq \Omega^{I+}_{x,i}$ for all phases x and y, hence for all interaction weights ω^{i}_{xy}, $0 \leq \omega^{i}_{xy} \leq 1$.

- Whenever we have a weight $\omega^{i}_{xy} \neq 0$ then, by the conditions given in Table 4.2, $\omega^{i}_{yx} = 0$. This means that in actuality we only need to calculate half of the separate fluid interaction weights, since the others will all be zero.

- The sum of all the weights equals one ($\omega_{11}+\omega_{22}+\omega_{33}+\omega_{12}+\omega_{21}+\omega_{23}+\omega_{32}+\omega_{31}+\omega_{13} = 1$) in each cell. The proof of this follows: consider the weights ω^{i}_{xy} and ω^{i}_{xz}, assuming all conditions in Table 4.2 are met. The sum of these two is given by $\omega^{i}_{xy}+\omega^{i}_{xz} = \Omega^{I+}_{x,i}\left(\dfrac{\Omega^{I-}_{y,i+1}}{\Omega^{I-}_{z,i+1}+\Omega^{I-}_{y,i+1}}\right) + \Omega^{I+}_{x,i}\left(\dfrac{\Omega^{I-}_{z,i+1}}{\Omega^{I-}_{z,i+1}+\Omega^{I-}_{y,i+1}}\right) = \Omega^{I+}_{x,i}$. Now consider if one of the conditions in Table 4.2 is not met, say we find $\Omega^{I-}_{z,i+i} = 0$. The sum of the two weights becomes $\omega^{i}_{xy}+\omega^{i}_{xz} = \Omega^{I+}_{x,i}\left(\dfrac{\Omega^{I-}_{y,i+1}}{0+\Omega^{I-}_{y,i+1}}\right) + \Omega^{I+}_{x,i}\left(\dfrac{0}{0+\Omega^{I-}_{y,i+1}}\right) = \Omega^{I+}_{x,i}$. The same is true if we find that $\Omega^{I-}_{y,i+i} = 0$. The other possibility is that we find $\Omega^{I+}_{x,i} = 0$ in which case $\omega^{i}_{xy}+\omega^{i}_{xz} = 0$. Hence if $\Omega^{I+}_{x,i} = 0$ then $\omega^{i}_{xy}+\omega^{i}_{xz} = 0$, otherwise $\omega^{i}_{xy}+\omega^{i}_{xz} = \Omega^{I+}_{x,i}$.

  Now consider the sum $\omega^{i}_{xx}+\omega^{i}_{xy}+\omega^{i}_{xz}$. If $\Omega^{I+}_{x,i} = 0$ then $\omega^{i}_{xx}+\omega^{i}_{xy}+\omega^{i}_{xz} =$

ω^i_{xx}. But if $\Omega^{I+}_{x,i} = 0$, then by Equation (4.24) $\phi_{x,i} \leq \phi_{x,i+1}$, hence $\omega^i_{xx} + \omega^i_{xy} + \omega^i_{xz} = \omega^i_{xx} = \phi_{x,i}$.

Now consider if $\Omega^{I+}_{x,i} \neq 0$. The sum $\omega^i_{xx} + \omega^i_{xy} + \omega^i_{xz} = \omega^i_{xx} + \Omega^{I+}_{x,i}$. Again if $\Omega^{I+}_{x,i} \neq 0$, then $\phi_{x,i} \geq \phi_{x,i+1}$ from Equation (4.24) which implies that $\omega^i_{xx} = \phi_{x,i+1}$ and $\Omega^{I+}_{x,i} = \phi_{x,i} - \phi_{x,i+1}$. Looking again at the sum $\omega^i_{xx} + \omega^i_{xy} + \omega^i_{xz} = \omega^i_{xx} + \Omega^{I+}_{x,i} = \phi_{x,i+1} + \phi_{x,i} - \phi_{x,i+1} = \phi_{x,i}$. Hence, under all circumstances, $\omega^i_{xx} + \omega^i_{xy} + \omega^i_{xz} = \phi_{x,i}$. The same proof can be done for the other phases, hence we can consider the sum $(\omega_{11} + \omega_{12} + \omega_{13}) + (\omega_{22} + \omega_{21} + \omega_{23}) + (\omega_{33} + \omega_{31} + \omega_{32}) = \phi_{1,i} + \phi_{2,i} + \phi_{3,i} = 1$ by definition of the volume fraction.

- In theory, the definitions given here for the weights can be extended to a flow of N fluids with simple modifications. We can define the self-interactions in an analogous way to Equation (4.22) and we may also find analogous conditions to Table 4.2. The weight for an interaction between two fluids j, k can then be defined as

$$\omega^i_{jk} = \begin{cases} 0 \quad \text{if} \quad \text{table conditions unsatisfied} \\ \\ \Omega^{I+}_{j,i} \left(\dfrac{\Omega^{I-}_{k,i+1}}{\left(\sum_{n=1}^{N} \Omega^{I-}_{n,i+1}\right)_{n \neq j}} \right) \quad \text{otherwise.} \end{cases} \tag{4.33}$$

Note that if the system has no void spaces (the sum of the volume fractions is 1 in every cell) then $\Omega^{I+}_{j,i} = \left(\sum_{n=1}^{N} \Omega^{I-}_{n,i+1}\right)_{n \neq j}$ since any donating boundary of phase j in cell i must be received by one of the other $N-1$ phases in cell $i+1$. However, in the case where the volume fractions of the N fluids do not add up to 1 (such as flow in a nozzle with varying area, or flow in a porous medium with non constant porosity) this relation does not hold, yet the definition of the weights in Equation (4.33) remains unchanged. Therefore the weights of Equation (4.33) could be used for multiphase flow in a porous medium or nozzle of varying area.

4.4.2 Calculating the Three Phase Flux.

Once the weights have been calculated, we calculate the intercell flux. We define this flux analogously with the previous two-phase solver (Equation 4.11) but extend it to include the nine interphase fluid interactions. The flux then reads

$$\begin{aligned}
\mathbf{F}_{i+1/2} = \omega_{11}\mathbf{F}^{11}_{i+1/2} + \omega_{22}\mathbf{F}^{22}_{i+1/2} + \omega_{33}\mathbf{F}^{33}_{i+1/2} + \\
+\omega_{12}\mathbf{F}^{12}_{i+1/2} + \omega_{21}\mathbf{F}^{21}_{i+1/2} + \omega_{13}\mathbf{F}^{13}_{i+1/2} + \\
+\omega_{31}\mathbf{F}^{31}_{i+1/2} + \omega_{32}\mathbf{F}^{32}_{i+1/2} + \omega_{23}\mathbf{F}^{23}_{i+1/2}.
\end{aligned} \tag{4.34}$$

The fluxes $\mathbf{F}^{xy}_{i+1/2}$, where x and y can be fluid 1, 2, or 3, are calculated by solving the Riemann problem for a single-phase system

$$\begin{aligned}
&\mathbf{U}_t + \mathbf{F}_x = \mathbf{0}, \\
&\mathbf{U}(\mathbf{x}, \mathbf{0}) = \begin{cases} \mathbf{Q}_L = \mathbf{Q}^x_i & \text{if} \quad x < x_{i+1/2}, \\ \mathbf{Q}_R = \mathbf{Q}^y_{i+1} & \text{if} \quad x > x_{i+1/2}. \end{cases}
\end{aligned} \tag{4.35}$$

4.4.3 Calculating Three Phase Nozzling Terms, F_{LAG}

The F_{LAG} terms for the three-phase solver are calculated analogously to Equation 4.16 in Section 4.3.1. For phase 1 (analogously phase 2 or 3):

$$\begin{aligned}
(\mathbf{F}_{LAG,i})_1 = \quad & M^{21}_i\omega_{21}\mathbf{U}^{21}_i - M^{12}_i\omega_{12}\mathbf{U}^{12}_i + m^{21}_{i-1}\omega_{21}\mathbf{U}^{21}_{i+1} \\
& -m^{12}_{i-1}\omega_{12}\mathbf{U}^{12}_{i-1} + M^{31}_i\omega_{31}\mathbf{U}^{31}_i - M^{13}_i\omega_{13}\mathbf{U}^{13}_i \\
& +m^{31}_{i-1}\omega_{31}\mathbf{U}^{31}_{i-1} - m^{13}_{i-1}\omega_{13}\mathbf{U}^{13}_{i-1},
\end{aligned} \tag{4.36}$$

where the $\mathbf{U}$ terms can be found analogously with Equation 4.17 and

$$M^{12} = max\left(0, \text{sign}\left(S_*^{(1,2)}\right)\right), \qquad m^{12} = min\left(0, \text{sign}\left(S_*^{(1,2)}\right)\right).$$

The resulting fluxes can then be substituted into Equation 3.9 to advance the system. Splitting the flux from a three-phase vector into three single-phase vectors has the massive advantage that simple well researched Riemann solvers such as the HLLC solver can be used to solve each subsystem, instead of trying to construct a nine wave Riemann solver to find the solution of the whole system, see [19].

4.4.4 Three Phase Volume Fraction Evolution

The algorithm for the evolution of the volume fraction for three phase flow is found analogously with Equation 4.21. For phase 1 (analogously phase 2 or 3):

$$\frac{\partial \phi_1}{\partial t} = \frac{1}{\Delta x} \begin{bmatrix} M_i^{12}\omega_{12}S_*^{(1,2)} - M_i^{21}\omega_{21}S_*^{(2,1)} + \\ m_{i-1}^{12}\omega_{12}S_*^{(1,2)} - m_{i-1}^{21}\omega_{21}S_*^{(2,1)} + \\ M_i^{13}\omega_{13}S_*^{(1,3)} - M_i^{31}\omega_{31}S_*^{(3,1)} + \\ m_{i-1}^{13}\omega_{13}S_*^{(1,3)} - m_{i-1}^{31}\omega_{31}S_*^{(3,1)} \end{bmatrix}. \tag{4.37}$$

Note that we need to use this algorithm for the first two fluid phases only, since $\phi_3 = 1 - \phi_1 - \phi_2$.

4.5 Test Cases

In this section we analyse how the new numerical scheme performs on four important test problems. The governing equations, Equations 4.1 - 4.4, are solved using the three phase numerical scheme of Section 4.4. The equations solved are repeated here:

$$\begin{aligned} \frac{\partial}{\partial t}(\phi_j\rho_j) + \frac{\partial}{\partial x}(\phi_j\rho_j u_j) &= 0 \\ \frac{\partial}{\partial t}(\phi_j\rho_j u_j) + \frac{\partial}{\partial x}\left(\phi_j\rho_j u_j^2 + \phi_j P_j\right) &= P_I\frac{\partial \phi_j}{\partial x} \\ \frac{\partial}{\partial t}(\phi_j\rho_j E_j) + \frac{\partial}{\partial x}(\phi_j\rho_j u_j E_j + \phi_j u_j P_j) &= P_I V_I \frac{\partial \phi_j}{\partial x} \\ \frac{\partial}{\partial t}\phi_j + V_I\frac{\partial}{\partial x}\phi_j &= 0. \end{aligned}$$

For each of the four test cases below we use the stiffened gas equation of state as presented in [64]:

$$P = (\gamma - 1)\,\rho e - \gamma\pi, \tag{4.38}$$

where γ and π are constants. e is the specific internal energy of the gas. The Riemann problems of Equation 4.35 are solved using the HLLC Rieman solver of Toro [72]. Each test is conducted with 200 cells over the $1m$ long tube with a timestep of $\Delta t = 1 \times 10^{-7}$s.

Note that as a consequence of the stratified solver each fluid is treated separately with its own equation of state and its own pressure, even if two fluids are the same, e.g, if there are two gases. We do not treat the gases as part of a mixture, but solve an individual set of conservation equations for each individual gas.

4.5.1 Test 1: A Moving Contact Discontinuity

The following test is designed to see if the new three-phase solver is able to accurately solve a simple flow regime: a moving contact discontinuity. Andrianov et al. [8] discuss this basic requirement for a multi-phase flow. Andrianov et al. state:

> *A flow, uniform in velocity and pressure, must remain uniform during its temporal evolution. In other words, under the uniformity conditions on velocity and pressure, a contact discontinuity must be preserved.*

The only variable that will change during this test then is the volume fractions of the phases. Test 1 consists of a $1m$ horizontal shock tube. The tube is filled with three fluids, one liquid and two different gases. The fluids are initially all at the same velocity and pressure. The parameters used in Test 1 are given in Table 4.3 below. Figure 4.4 shows the volume fractions of each

Table 4.3: Test 1 parameters

Parameter	Gas # 1	Gas # 2	Liquid
$P(x < 0.5m)$ (Pa)	1×10^6	1×10^6	1×10^6
$P(x > 0.5m)$ (Pa)	1×10^6	1×10^6	1×10^6
$u(x < 0.5m)$ (ms^{-1})	50	50	50
$u(x > 0.5m)$ (ms^{-1})	50	50	50
$\rho(x < 0.5m)$ (kgm^{-3})	0.5	1	1000
$\rho(x > 0.5m)$ (kgm^{-3})	0.5	1	1000
$\phi(x < 0.5m)$	0.1	0.3	0.6
$\phi(x > 0.5m)$	0.2	0.5	0.3
π	1.4	1.6	4.4
γ	0	0	6×10^8

phase for three different times. The volume fractions advect to the right hand side of the tube as expected.

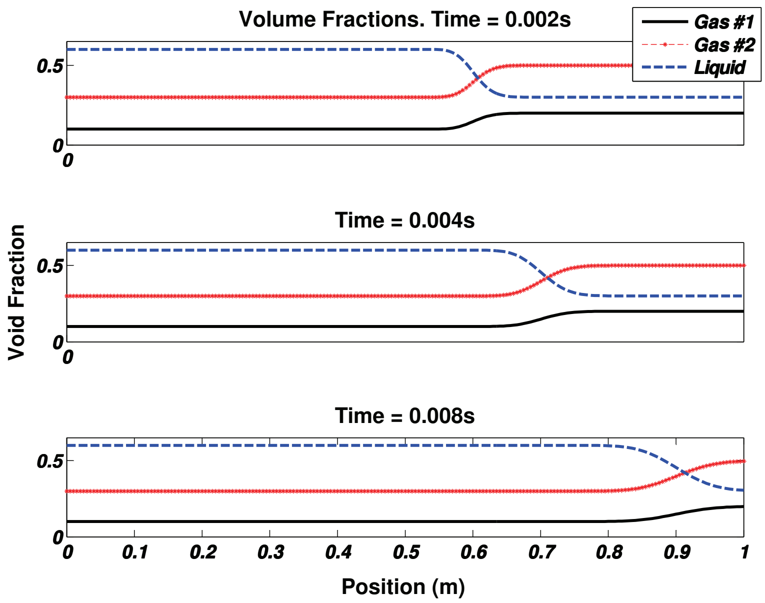

Figure 4.4: *The moving contact discontinuity. We see the volume fractions of the phases advecting to the right hand side of the tube as expected.*

In Figure 4.5 we see that the liquid density and pressure remain constant over time. Similarly, the density and pressure of the two gas phases remain constant, and the liquid velocity is consistently $50ms^{-1}$. We therefore conclude that this method is able to accurately deal with a contact discontinuity by preserving the pressure and velocity uniformity conditions.

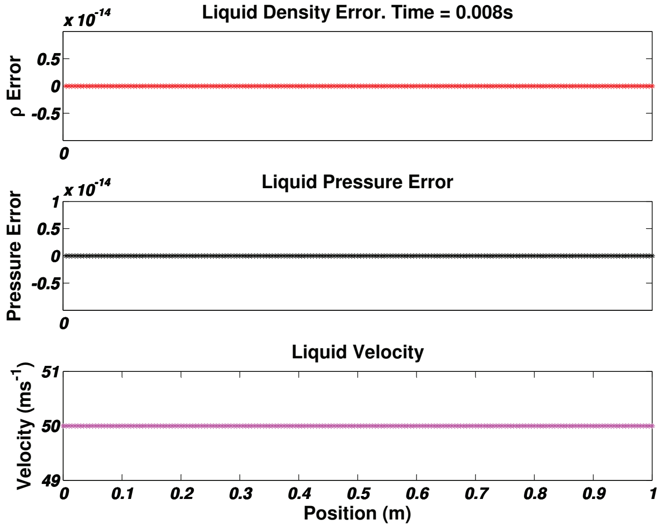

Figure 4.5: *Errors in the liquid flow variables. We see that the method preserves the uniformity condition on the pressure and velocity of the flow.*

4.5.2 Test 2: The Simplified Three Fluid Problem

The next test of the new three-phase method is effectively a two-phase flow problem. If we have two gases with the exact same parameters γ and π in Equation 4.38, and the two gases also have the same pressure and velocity, then the parameters of both gases should evolve exactly equal to each other. These two gases should, effectively, flow as one gas. Additionally, the new three-phase solver of Section 4.4 should reduce to the solver of [19] in two-phases. Test 2 is taken from [19]. A $1m$ horizontal shock tube is filled with liquid and gas (in Toro's paper it is a single gas, in Test 2 we have two gases with the same parameters, hence they act as one gas). The parameters used in Test 2 are given in Table 4.4 below: The output times for all graphs is $0.25 \times 10^{-3}s$.

Table 4.4: Test 2 parameters

Parameter	Gas # 1	Gas # 2	Liquid
$P(x < 0.5m)$ (Pa)	0.2×10^6	0.2×10^6	0.2×10^7
$P(x > 0.5m)$ (Pa)	0.18×10^6	0.18×10^6	0.18×10^6
$u(x < 0.5m)$ (ms^{-1})	9	9	9
$u(x > 0.5m)$ (ms^{-1})	5	5	5
$\rho(x < 0.5m)$ (kgm^{-3})	1.5	1.5	1000
$\rho(x > 0.5m)$ (kgm^{-3})	1	1	1000
$\phi(x < 0.5m)$	0.1	0.1	0.8
$\phi(x > 0.5m)$	0.4	0.4	0.2
π	1.4	1.4	4.4
γ	0	0	6×10^8

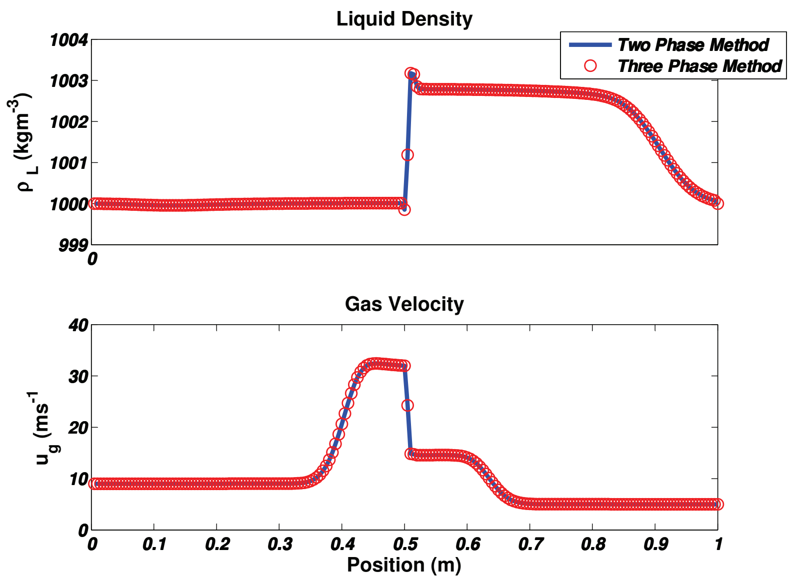

Figure 4.6: *Plots of the liquid density and the gas (the 2-phase gas) velocity with the old two-phase solver and the new 3-phase solver.*

Figure 4.6 is a comparison plot of the liquid density and the gas velocity after $0.025 \times 10^{-3}s$ using the new three-phase solver and the old two-phase solver of [19]. The plots are identical whether using the new or old method. This is further supported by Figure 4.7 which shows that the three-phase solver keeps the two gas phases (gas 1 and gas 2) in the three-phase test at the same pressure and velocity. In summary then, the new three-phase solver performs well under a two-phase flow test and reduces to the solver of [19] under two-phase flow conditions.

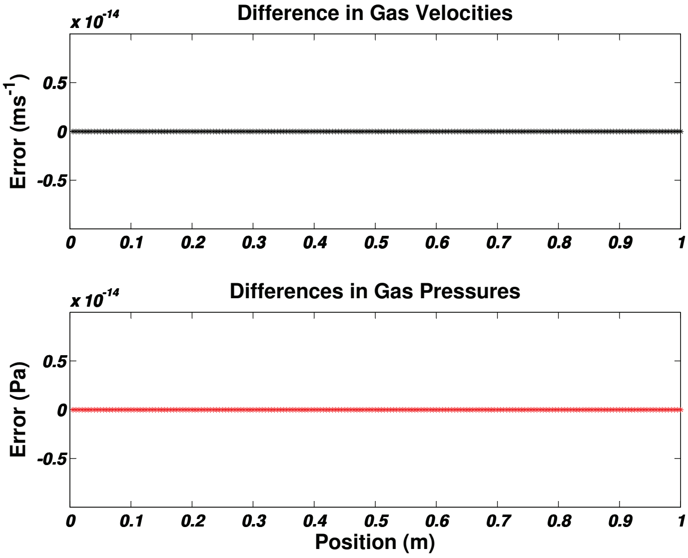

Figure 4.7: *Difference between the velocities and pressures of gas* 1 *and gas* 2 *in the new three-phase solver. The plots show that the velocities and pressures of the two gases are equal.*

4.5.3 Test 3: An Interface Problem

Test 3 examines the methods' ability to handle interface problems. Such problems have become common tests of numerical methods for two-phase flow since exact solutions can be found for the fluid velocity, pressure, and density, see, for example, [64]. The test consists of a chamber of almost pure liquid separated from a chamber of almost pure gas. A constant time step is used to produce an output time of $229\mu s$. The parameters used in Test 3 are given in Table 4.5 below. The gas phase densities and volume fractions were carefully chosen to mimic the two-phase test found in [64] where the same parameters were used except for a single gas with density $50kgm^{-3}$. Our choice of the two gas densities and volume fractions means that the total gas phase ($\phi_{g1}\rho_{g1} + \phi_{g2}\rho_{g2}$) has density $50kgm^{-3}$, yet the flow is still technically a three-pase flow. The benefit of such a choice of gas densities and volume fractions is that we can now compare our solution to the exact two-phase

Table 4.5: Test 3 parameters

Parameter	Gas # 1	Gas # 2	Liquid
$P(x < 0.7m)\ (Pa)$	1×10^9	1×10^9	1×10^9
$P(x > 0.7m)\ (Pa)$	1×10^5	1×10^5	1×10^5
$u(x < 0.7m)\ (ms^{-1})$	0	0	0
$u(x > 0.7m)\ (ms^{-1})$	0	0	0
$\rho(x < 0.7m)\ (kgm^{-3})$	70	10	1000
$\rho(x > 0.7m)\ (kgm^{-3})$	70	10	1000
$\phi(x < 0.7m)$	$(1 \times 10^{-6})/2$	$(1 \times 10^{-6})/2$	$1 - 1 \times 10^{-6}$
$\phi(x > 0.7m)$	$2(1 - 1 \times 10^{-6})/3$	$(1 - 1 \times 10^{-6})/3$	1×10^{-6}
π	1.4	1.4	4.4
γ	0	0	6×10^8

solution for the fluid velocity, pressure, and density.

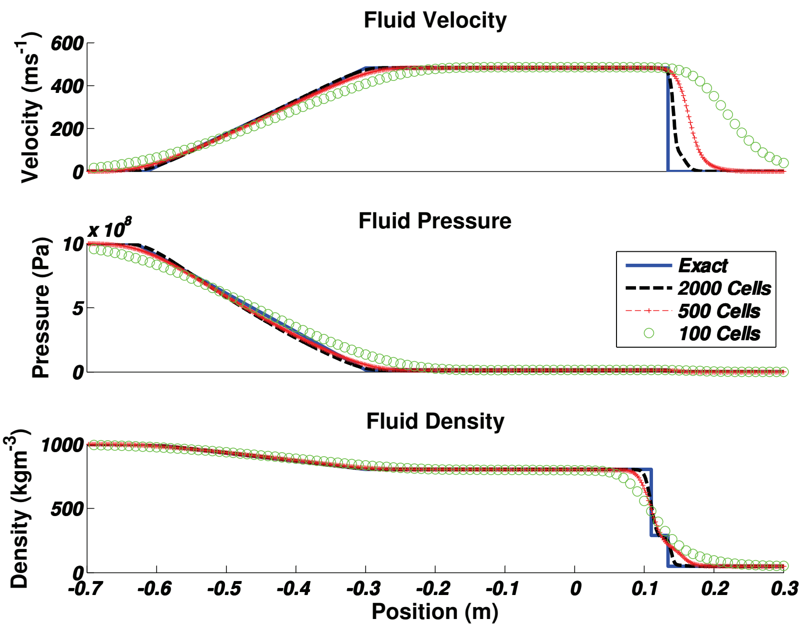

Figure 4.8: *Plots of the fluid velocity, pressure, and density for various number of cells and also the exact solution.*

Figure 4.8 shows the fluid velocity, pressure, and density at $229\mu s$. The fluid values were found using

$$\rho_f = \sum_i \rho_i \phi_i,$$
$$P_f = \sum_i P_i \phi_i,$$
$$u_f = \frac{\sum_i \rho_i \phi_i u_i}{\sum_i \rho_i \phi_i}.$$

The two-phase exact solution is shown alongside the numerical solutions for an increasing number of cells in the $1m$ domain. Figure 4.8 shows that the numerical solution approaches the exact solution as the number of computational cells is increased. There is some error around the contact and shock waves. A zoomed view of these waves is given in Figure 4.9.

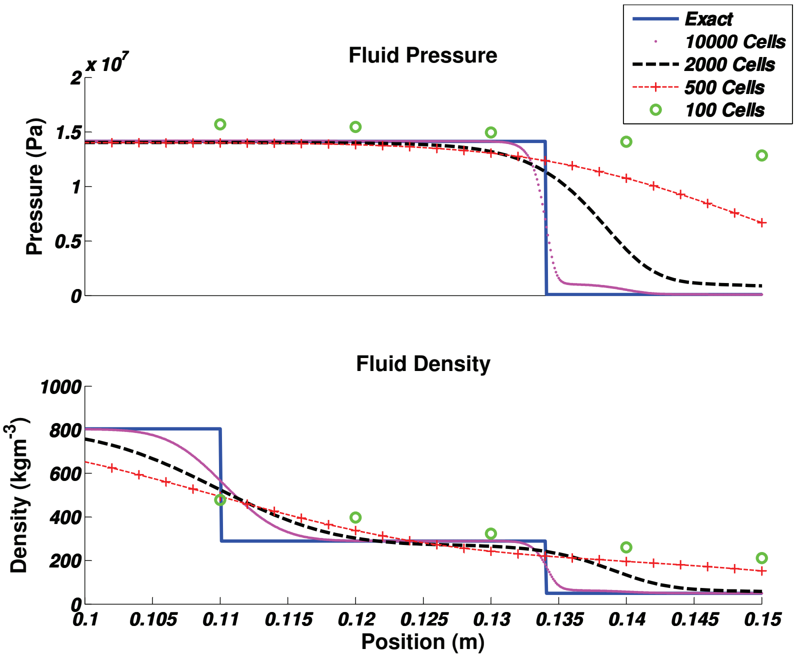

Figure 4.9: *A zoomed in view of the contact and shock waves for the fluid pressure and density.*

Again the solution is converging to the exact two-phase solution with an increasing number of cells. The method performs well on this test as expected. We take the results of this test to indicate that the method can successfully handle interface problems.

4.5.4 Test 4: A Three-Phase Mixture

Test 4 is an experiment to show the evolution of a three-phase mixture of two different gases and a liquid. The initial pressures of all fluid components are the same, and the initial velocity of the fluids is zero. This test should show that the method allows the pressure and velocity of each fluid component to evolve individually. The parameters used in Test 4 are given in Table 4.6 below: Figure 4.10 shows that each fluid (governed by its individual version

Table 4.6: Test 4 parameters

Parameter	Gas # 1	Gas # 2	Liquid
$P(x < 0.5m)$ (Pa)	1×10^6	1×10^6	1×10^6
$P(x > 0.5m)$ (Pa)	0.5×10^6	0.5×10^6	0.5×10^6
$u(x < 0.5m)$ (ms^{-1})	0	0	0
$u(x > 0.5m)$ (ms^{-1})	0	0	0
$\rho(x < 0.5m)$ (kgm^{-3})	0.5	1.5	1000
$\rho(x > 0.5m)$ (kgm^{-3})	1	2	1000
$\phi(x < 0.5m)$	0.1	0.3	0.6
$\phi(x > 0.5m)$	0.2	0.6	0.2
π	1.4	1.6	4.4
γ	0	0	6×10^8

of the stiffened gas equation of state) is able to evolve independently of the other fluids. Each fluid has its own pressure and velocity. This test shows that the new three-phase solver can handle the three-phase flow of fluids with different thermodynamic properties. Note that in an actual flow, other factors such as mass and momentum transfer would also have an effect on the flow. This is beyond the scope of this testing and was not considered here.

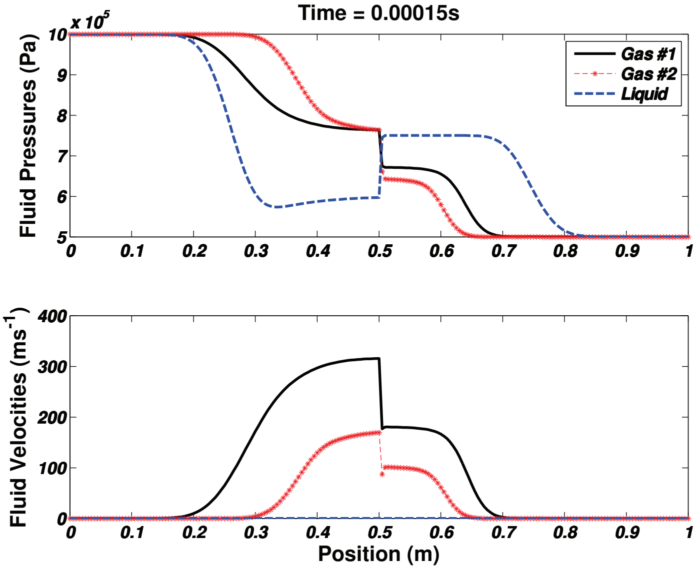

Figure 4.10: *A plot of the individual fluid pressures and velocities. Each fluid phase is able to evolve independently of the others.*

Convergence of Test 4 In order to ensure the numerical solver is working as it should we consider here the order of convergence as we refine the mesh of the numerical experiment of Test 4. Figure 4.11 below shows the velocity of Gas 1 as we refine the mesh from 50 cells to 1600 cells over the $1m$ domain. As the spacestep is scaled, the timestep is also scaled appropriately.

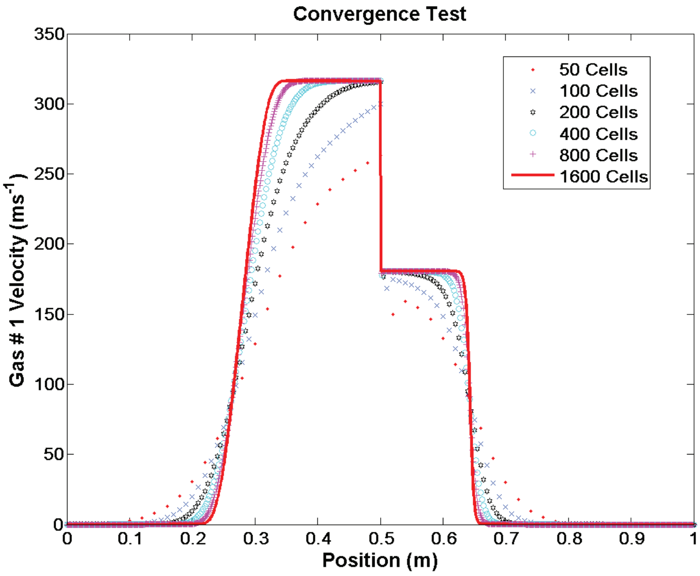

Figure 4.11: *A convergence plot of the velocity of gas* 1 *as the mesh is refined from* 50 *cells to* 1600 *cells. The figure shows convergence of the solution under mesh refinement.*

Figure 4.11 shows that the method converges under mesh refinement. This is confirmation that our new solver is working as expected. Below in Table 4.7 we approximate the order of the method. The L_2 norm is calculated between solutions as the step size is halved and the convergence ratio is approximated. As we refine the mesh the error found using the L_2 norm also reduces. We see an error ratio of between $0 - 1$ which indicates that this method is first order (the HLLC Riemann solver used was also first

Table 4.7: Test 4 convergence

# Cells	L_2 Norm	Convergence Ratio
1600	0.0385	0.5268
800	0.0730	0.6388
400	0.1143	0.6719
200	0.1702	0.7041
100	0.2417	0.7525
50	0.3212	$\cdots$

order). We are therefore confident that this method is working as expected.

4.6 Conclusions

In this chapter we have extended the two-phase stratified solver to be able to handle three-phase flows. The new method was tested to show that it is suitable to be used in a three-phase flow situation. We believe that this new solver will be useful since it is simple to implement and eases the burden of solving a series of large Riemann problems by splitting the flux vector into single phase systems.

Chapter 5

Details on the Phase Change Equations

In Chapter 4 a numerical scheme was developed which was able to solve a class of hyperbolic equations describing horizontal three phase flow. This method, however, needs to be modified to account for phase change between the liquid water and water vapour phases during a hydrothermal eruption. This modification is the subject of the current chapter.

In the literature, interphase mass transfer is usually handled by adding source terms to the conservation equations, see [65]. However, in the case of boiling water the liquid and vapour phases are assumed to stay on the boiling point with depth curve. After one iteration of the numerical solver the thermodynamic variables will have evolved according to the fluxes at the boundaries of the cells. This causes the variables of the water phases to leave the boiling point curve. By necessity, some mechanism must exist to bring the system back onto the boiling point with depth curve; this mechanism is phase change between the liquid and vapour phases of the water. For this reason we must handle phase change between the fluids in a non standard way. This chapter details the numerical method used to account for the amount of boiling taking place at each time step.

5.1 Modification to the HLLC Solver for the Entropy Equation

In Section 4.1.1 Equation 4.5 was introduced to govern the conservation of entropy of a fluid phase. For further use in this chapter it will be useful to replace the energy equation, Equation 4.3, with the entropy equation, Equation 4.5, in the Euler Equations. The set of equations to solve in the horizontal case becomes:

$$\frac{\partial}{\partial t}(\phi_j\rho_j) + \frac{\partial}{\partial x}(\phi_j\rho_j u_j) = 0, \tag{5.1}$$

$$\frac{\partial}{\partial t}(\phi_j\rho_j u_j) + \frac{\partial}{\partial x}\left(\phi_j\rho_j u_j^2 + \phi_j P_j\right) = P_I\frac{\partial \phi_j}{\partial x}, \tag{5.2}$$

$$\frac{\partial}{\partial t}(\phi_j\rho_j s_j) + \frac{\partial}{\partial x}(\phi_j\rho_j u_j s_j) = 0, \tag{5.3}$$

$$\frac{\partial}{\partial t}\phi_j + V_I\frac{\partial}{\partial x}\phi_j = 0, \tag{5.4}$$

and the HLLC middle wave states become:

$$\mathbf{U}_{*k} = \rho_k\left(\frac{S_k - u_k}{S_k - S_*}\right)\begin{bmatrix} 1 \\ S_* \\ s_k \end{bmatrix}. \tag{5.5}$$

Note that energy is also implicitly conserved (via the fundamental thermodynamic relation) since entropy and mass are conserved.

5.2 Equations of State

To close the set of Equations 5.1 – 5.4, appropriate equations of state must be provided for each phase. In the case of natural hydrothermal eruptions we consider three phases: liquid water, water vapour, and air. The initial liquid water and water vapour phases make up the underground geothermal reservoir, and the air phase is associated with the above ground fluid.

The Air Equation of State. We choose to use the ideal gas with constant specific heats as defined in [21] for the equation of state of the air phase. The governing equations are

$$P_a = \rho_a R T_a, \tag{5.6}$$

$$e_a = \frac{5}{2} R T_a, \tag{5.7}$$

where $R = 287.05 JKg^{-1}K^{-1}$ is the specific gas constant for air. The entropy of the air is approximated by

$$s_a = \frac{7}{2} R \ln(T_a) - R \ln(P_a). \tag{5.8}$$

The Liquid Water and Water Vapour Equation of State. The conceptual model of a hydrothermal eurption introduced in Section 2.4.1 assumes that the water below the surface in a geothermal field lies at boiling point conditions. We assume that throughout the eruption this relationship holds. Therefore, the equation of state chosen for the liquid water and water vapour is governed by the steam tables of [62]. This choice has some interesting consequences for the numerical method and for the structure of the fluid itself, since we have to account for phase change between the liquid water and water vapour.

5.3 The Relaxation and Evaporation Solver

We now need to develop a numerical scheme to account for the phase change between the liquid water and water vapour. As in [46] and [76], we assume that any boiling occurs too rapidly for thermal conduction to have any effect on the flow, i.e., we assume that the flow is adiabatic. We can use simple thermodynamics to describe the adiabatic flashing of liquid water to vapour. Following [16] we may write the fluid entropy, s_F, of the liquid-vapour-air mixture as

$$s_F = \frac{\chi_a s_a \rho_a + \chi_w \Phi_v s_v \rho_v + \chi_w \Phi_l s_l \rho_l}{\chi_a \rho_a + \chi_w \Phi_v \rho_v + \chi_w \Phi_l \rho_l}, \tag{5.9}$$

where $\chi_a = \phi_a$ is the volume fraction of the air phase and $\chi_w = \phi_v + \phi_l$ is the volume fraction of the water phase (liquid water + vapour). Φ_v is the fraction of vapour in the water phase (termed the vapour water fraction), defined such that $\phi_v = \chi_w \Phi_v$ and $\phi_l = \chi_w \Phi_l$. Note that $\Phi_l + \Phi_v = 1$. As in [46] and [76], the principle of adiabatic flashing allows us to assume that the total entropy of the system s_F is conserved. Note that the entropy of the system will change due to advection during the application of the three-phase solver, but the entropy in each cell is conserved during the phase change process. Note also that this process is not reversible (not isentropic) due to the relaxation process to be discussed shortly. Equation (5.9) can be rearranged to obtain

$$\Phi_v = \frac{\chi_w \rho_l \left(s_l - s_F\right) + \chi_a \rho_a \left(s_a - s_F\right)}{\chi_w \rho_l \left(s_l - s_F\right) + \chi_w \rho_v \left(s_F - s_v\right)}. \tag{5.10}$$

We can use Equation 5.10 to quantify how much liquid has been boiled to vapour using conservation of entropy. However, we must first have an appropriate way of bringing the evolved system back onto the boiling point curve after the three-phase solver has been applied. This is achieved via a relaxation process.

5.3.1 Fundamental Thermodynamic Relation

The fundamental thermodynamic relation is a statement of how energy changes in a closed system in equilibrium in response to changes in entropy and/or volume. It reads:

$$de = Tds - Pd\nu, \tag{5.11}$$

where e is the internal energy of the fluid and ν the specific volume ($\nu = 1/\rho$). The flow problem occurs in a closed system so the total energy of the fluid must be conserved. As a simplifying assumption we assume that the total internal energy is conserved. This assumption is not physically accurate since in a given flow the internal energy will not be conserved but a portion of it will be converted to kinetic energy. However, we need to define a path by which we can bring our boiling fluids back onto the boiling point curve, hence we must make some simplification to proceed further. Furthermore, we believe the effects of this assumption are minor, since the major source of acceleration of a flow is the volume expansion due to boiling. As in [76] we assume that total entropy is also conserved during the boiling. However, the entropy and internal energy of each *phase* of the fluid need not be conserved, rather, any change in entropy/energy of the one phase must be compensated for in the other phases. We assume that any entropy and energy transfers during boiling occur only between the liquid and vapour phases since these are directly involved in the phase change process. Mathematically,

$$ds_v = -ds_l, \tag{5.12}$$

$$de_v = -de_l. \tag{5.13}$$

We can use Equations 5.11 - 5.13 to obtain

$$\frac{d\nu_v}{d\nu_l} = -1. \tag{5.14}$$

We may integrate Equation 5.14 with respect to ν_l. This gives

$$\nu_v = -\nu_l + C_I, \tag{5.15}$$

where C_I is an integration constant. In a plot of ν_v versus ν_l, Equation 5.15 is a straight line, along which the total energy and total entropy of the system is conserved. Figure 5.1 is a plot of the specific volumes of liquid water and water vapour along the boiling point line. One iteration of the numerical solver takes us from point A on the boiling point curve to point B off the curve in Figure 5.1. Let $\nu_l(B)$ and $\nu_v(B)$ be the specific volumes of the liquid and the vapour at point B respectively. The line in Equation 5.15 must pass through this point B. Therefore, the integration constant C_I is given by $C_I = \nu_v(B) + \nu_l(B)$. We can then rewrite Equation 5.15.

$$\nu_v = -\nu_l + \nu_v(B) + \nu_l(B). \tag{5.16}$$

From here we can find the point C, where the line L given by Equation 5.16 meets the boiling point curve in Figure 5.1. This is our new state for the system and gives us the phase densities from which we can calculate the phase entropies from the equation of state and calculate the phase volume fractions using Equation 5.10.

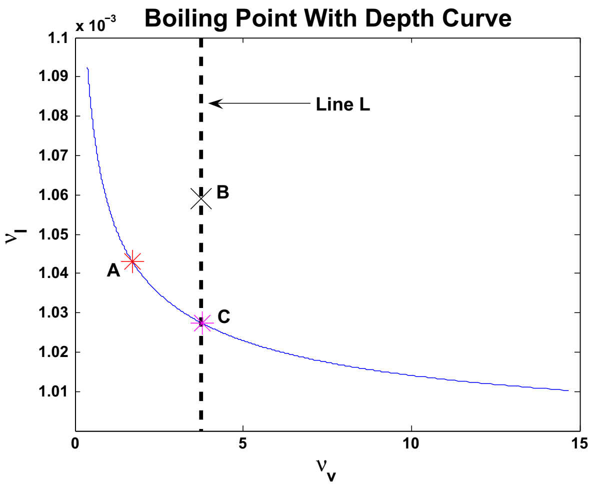

Figure 5.1: *The fluid begins at the point A. The three-phase solver is applied to move the state of the fluid to point B. Then the relaxation routine is applied causing the fluid state to move down line L and finish at point C. The evaporation solver is then applied which quantifies the amount of boiling in the system.*

5.3.2 The Relaxation Velocity

Once we evolve our system through points A to C we are able to calculate other thermodynamic variables for each phase. We must, however, assume that the total momentum is conserved during the boiling process (moving from point B to C in Figure 5.1). Mathematically,

$$\phi_v^C \rho_v^C u_v^C + \phi_l^C \rho_l^C u_l^C = \phi_v^B \rho_v^B u_v^B + \phi_l^B \rho_l^B u_l^B \tag{5.17}$$

where the supercripts B and C refer to the thermodynamic variable values at the points B or C in Figure 5.1. We have two unknowns (u_v^C and u_l^C) and one equation (5.17). We therefore make a further assumption that $u_l^C = u_l^B$; the velocity of the liquid phase is constant during the boiling process. This is a realistic assumption, since the density of liquid is of the order of 1000 times greater than that of vapour. This implies it would take large changes in the liquid momentum to change the liquid velocity significantly. However, the vapour velocity will change with only small changes in momentum. Setting $u_l^C = u_l^B$ and solving Equation 5.17 for u_v^C we obtain

$$u_v^C = \frac{\phi_v^B \rho_v^B u_v^B + \phi_l^B \rho_l^B u_l^B - \phi_l^C \rho_l^C u_l^C}{\phi_v^C \rho_v^C}. \tag{5.18}$$

The Common Velocity. We now have evolved the system via the advection scheme, then used relaxation and evaporation routines to arrive at the new state of our system. In reality there will be some drag forces between the fluid phases which act to slow down or speed up the relative motion of each phase. A common method to deal with this motion is that of infinite relaxation parameters (see [65]). For simplicity we assume that the interphase drag forces are great enough that the three fluid phases reach equilibrium in some time $t_e < \Delta t$ where Δt is the current timestep of the numerical method. We therefore define a common velocity for the fluid as follows

$$\begin{aligned} u_F &= \frac{\sum_j \phi_j \rho_j u_j}{\sum_j \phi_j \rho_j}, && (5.19) \\ u_v &= u_l = u_a \equiv u_F. && (5.20) \end{aligned}$$

5.4 Conclusions

In this chapter we have modified the numerical scheme of Section 4.4 to be able to account for phase change (boiling) between the liquid water and water vapour phases of our flow. We have exchanged the energy equation for an entropy equation, and have modified the HLLC Riemann solver accordingly. This change, when combined with the relaxation and boiling procedures of Section 5.3, will allow us to simulate a horizontal flow with boiling.

Chapter 6

Vertical Flow Equations and Methods

Chapter 4 introduced the governing equations of horizontal three phase flow and a new numerical method to solve the system. The work of Chapter 5 extended this numerical method to quantify the amount of boiling occurring in each timestep and gave instructions on how to bring the system into a relaxed state. The current chapter modifies the governing equations and associated numerical method to handle 1-D vertical flow.

6.1 Vertical Flow Equations

In its current form, the HLLC solver of Section 3.1.2 will produce inconsistent middle wave speeds for vertical flow which lead to errors in the solutions. This problem is highlighted when we observe static flows where the thermodynamic variables (pressure, density, fluid speed, etc) should be unchanging over time. The entropic version of the multi-phase Euler equations, including gravitational terms, are given by

$$\begin{aligned}
\frac{\partial}{\partial t}\left(\phi_j\rho_j\right)+\frac{\partial}{\partial z}\left(\phi_j\rho_j u_j\right) &= 0, && (6.1)\\
\frac{\partial}{\partial t}\left(\phi_j\rho_j u_j\right)+\frac{\partial}{\partial z}\left(\phi_j\rho_j u_j^2+\phi_j P_j\right) &= P_I\frac{\partial \phi_j}{\partial z}-\phi_j\rho_j g, && (6.2)\\
\frac{\partial}{\partial t}\left(\phi_j\rho_j s_j\right)+\frac{\partial}{\partial z}\left(\phi_j\rho_j u_j s_j\right) &= 0, && (6.3)\\
\frac{\partial}{\partial t}\phi_j+V_I\frac{\partial}{\partial z}\phi_j &= 0. && (6.4)
\end{aligned}$$

for each phase j. As before, ρ, u, P, s are defined as the fluid density, velocity, pressure, and specific entropy respectively. Note that the lack of source terms in the entropy equation ensures that we have an adiabatic flow as in [76]. g is the acceleration due to gravity which acts in the z vertical direction. Also as before,

$$\begin{aligned} P_I &= \sum_j \phi_j P_j, \\ V_I &= \frac{\sum_j \phi_j \rho_j u_j}{\sum_j \phi_j \rho_j}. \end{aligned}$$

In the case of static flow ($u_j \equiv 0$ and all time derivatives $\equiv 0$) we find the natural pressure profile of the fluid given as a differential equation:

$$\frac{\partial}{\partial z} P_f = -g\rho_f, \tag{6.5}$$

where $P_f = \sum_j \phi_j P_j$ and $\rho_f = \sum_j \phi_j \rho_j$. The middle wave speed, Equation 3.20, of the HLLC solver is derived in [72]. Toro assumes the following about the middle wave states:

$$\begin{cases} u_{*L} = u_{*R} = u_* = S_* & , \\ P_{*L} = P_{*R} = P_* & . \end{cases} \tag{6.6}$$

These assumptions are justified since these conditions are satisfied by the exact solution (the middle wave is a contact discontinuity, see [72] for further details). Substituting the conditions of Equation 6.6 into the relations for the middle wave states, that is, Equation 3.17, Toro obtains the following solutions for the pressure in the middle wave regions:

$$\begin{cases} P_{*L} = P_L + \rho_L (S_L - u_L)(S_* - u_L) & , \\ P_{*R} = P_R + \rho_R (S_R - u_R)(S_* - u_R) & . \end{cases} \tag{6.7}$$

From 6.6 we set $P_{*L} = P_{*R}$ and solve for the middle wave speed, S_*,

$$S_* = \frac{P_R - P_L + \rho_L u_L (S_L - u_L) - \rho_R u_R (S_R - u_R)}{\rho_L (S_L - u_L) - \rho_R (S_R - u_R)},$$

as in Equation 3.20.

6.2 Modified Middle Wave Speed, S_*

The assumptions of Equation 6.6 are valid for the horizontal case where the pressure of the system is not naturally varying in the space coordinate.

However, in the vertical flow case we have a natural pressure gradient arising from the weight of the overlying fluid. The pressure in the fluid is governed by Equation 6.5 in the multi-phase flow case. Therefore we modify the pressure assumption of Equation 6.6 to be:

$$P_{*L} = P_{*R} + \Delta P. \tag{6.8}$$

We assume the left state, P_L, is '*below*' the state P_R and therefore should be at a higher pressure, see Figure 6.1.

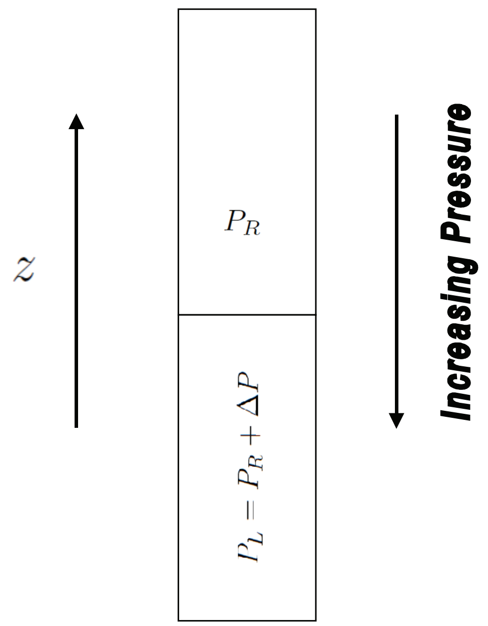

Figure 6.1: *Adjoining cells of a fluid in a vertical state. The pressure is determined by Equation 6.5.*

We can obtain an approximation for ΔP by discretizing Equation 6.5. For the single phase case we find

$$\Delta P = \rho_R g \Delta z, \tag{6.9}$$

where ρ_R is the fluid density in the right cell and g is the acceleration due to gravity. We can now substitute Equation 6.9 into Equation 6.8 and solve for S_* as before. We obtain:

$$S_* = \frac{P_R - P_L + \rho_R g \Delta z + \rho_L u_L (S_L - u_L) - \rho_R u_R (S_R - u_R)}{\rho_L (S_L - u_L) - \rho_R (S_R - u_R)}. \tag{6.10}$$

This new middle wave speed will now preserve the case of a static vertical fluid, that is, there are no erroneous variations in the pressure, density, fluid speed, etc. over time when the new middle wave speed is used in conjunction with the numerical discretization of the Equation set 6.1 – 6.3. A simple test case is shown in the next subsection. The gravitational term in the momentum equation, Equation 6.2, is solved in the standard way, that is, using a fractional splitting, see [72].

6.2.1 Vertical Flow Test: A Static Compressible Gas

In this subsection we perform a simple numerical experiment to see if the new middle wave speed of Equation 6.10 will improve the accuracy of a vertical flow problem.

Consider a $1m$ tall column of a compressible gas as in Figure 6.1. The pressure in the gas is governed by the relation given in Equation 6.5. The density of the gas will increase the further down in the vertical column we go. The fluid is initially at rest and should remain so as time evolves. Additionally, for the static case, the middle wave speed should be zero. The equation of state chosen for the gas is that for water vapour as given by the steam tables [62]. These tables contain the density, temperature, internal energy of the vapour for a given pressure.

$z = 0$ is taken to be the top of the gas column and we set $P(z = 0) = 1e^5\,Pa$. The cell length is taken as $\Delta z = 0.01m$ and the output time for all figures is $5ms$ with 1600 timesteps.

Old Middle Wave Speed, S_*

The HLLC method with the old wave speed of Equation 3.20 does not preserve the steady static state for the compressible case. The errors in Figure 6.2 show that the method does not preserve the gas density, neither does it preserve the hydrostatic pressure profile. Figure 6.3 shows that the method has a positive middle wave speed and that the liquid is not static (it now has a positive gas velocity).

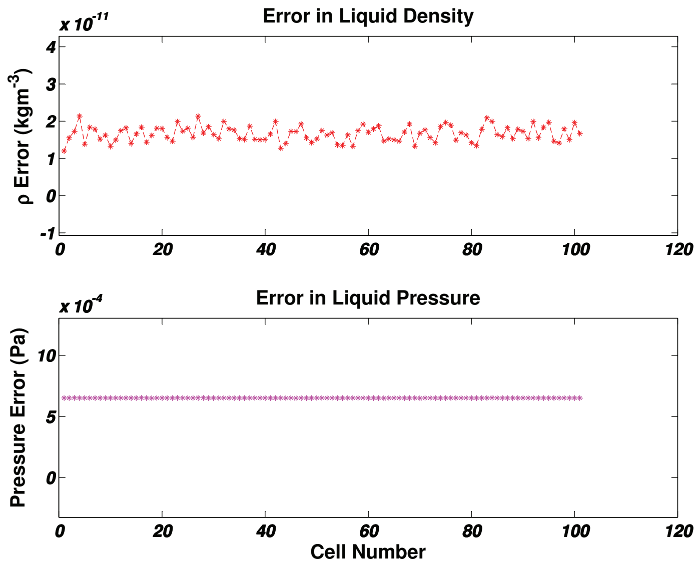

Figure 6.2: Error in the gas density and pressure. Output time is $5ms$ and each cell is $0.01m$ in length. The old middle wave speed does not conserve the static state.

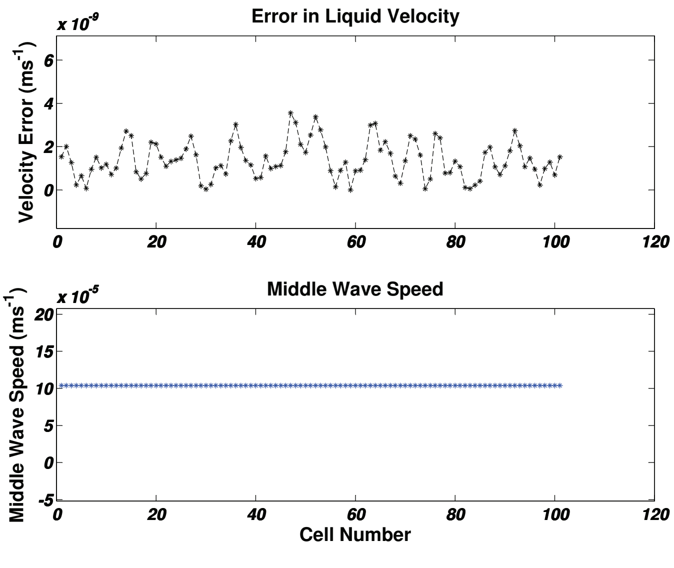

Figure 6.3: Error in the gas velocity and a plot of the middle wave speed. Output time is $5ms$ and each cell is $0.01m$ in length. The old middle wave speed is greater than zero for the compressible and causes the gas velocity to increase.

New Middle Wave Speed, S_*

The HLLC method with the new wave speed of Equation 6.10 preserves the steady static state for the compressible case. Figure 6.5 shows that the middle wave speed is zero, as is the gas velocity.

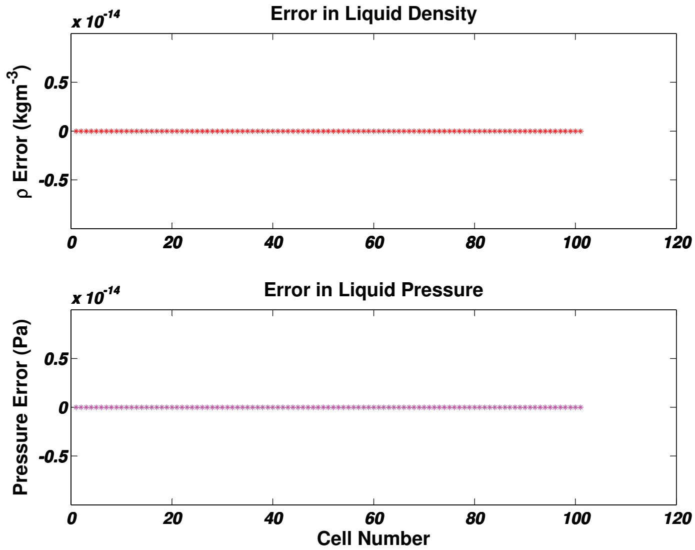

Figure 6.4: Error in the gas density and pressure. Output time is $5ms$ and each cell is $0.01m$ in length. The new middle wave speed conserves the static state.

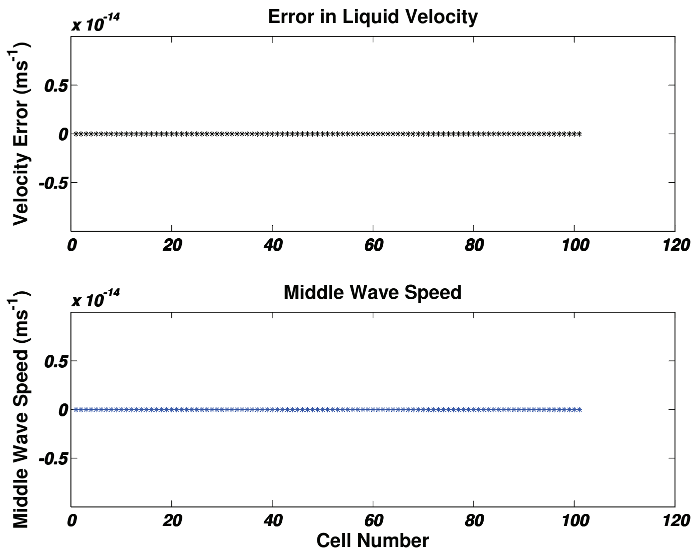

Figure 6.5: Error in the gas velocity and a plot of the middle wave speed. Output time is $5ms$ and each cell is $0.01m$ in length. The new middle wave speed is exactly zero for the compressible case.

This numerical experiment shows the advantage of using the new middle wave speed. In the case of a static fluid, errors produced by inaccurate calculation of the middle wave speed were completely eliminated. We will use this new formulation for the middle wave speed to simulate vertical flow during a hydrothermal eruption later in this thesis.

6.3 Full Numerical Method

Accounting for vertical flow, and using the entropy equation in place of an energy equation, the system of conservation equations to solve becomes

$$
\begin{aligned}
\frac{\partial}{\partial t}(\phi_j \rho_j) + \frac{\partial}{\partial z}(\phi_j \rho_j u_j) &= 0, \\
\frac{\partial}{\partial t}(\phi_j \rho_j u_j) + \frac{\partial}{\partial z}\left(\phi_j \rho_j u_j^2 + \phi_j P_j\right) &= P_I \frac{\partial \phi_j}{\partial z} - \phi_j \rho_j g, \\
\frac{\partial}{\partial t}(\phi_j \rho_j s_j) + \frac{\partial}{\partial z}(\phi_j \rho_j u_j s_j) &= 0, \\
\frac{\partial}{\partial t}\phi_j + V_I \frac{\partial}{\partial z}\phi_j &= 0,
\end{aligned}
$$

which is the system of equations, Equations 6.1 - 6.4. The numerical algorithm for one time step of the system is summarised below.

Evolution Algorithm Using the theory from the previous chapters and sections we can calculate the fluid pressure, the volume fraction of each phase, and the other thermodynamic variables by applying the following algorithm for one step of our numerical solver:

1. Apply the multiphase advection solver of Section 4.4 using the modified HLLC solver and middle wave speeds from Chapter 6 to the system of Equations 6.1 - 6.4 at point A of Figure 5.1. The fluid will evolve to a new point B of Figure 5.1. B may or may not lie on the boiling point line.

2. Account for gravitational sources in the standard way using the fractional step method, see [72].

3. Calculate the specific volume of each phase ($\nu_i = 1/\rho_i$). Define the line L from Figure 5.1 given by Equation 5.16.

4. Solve for the point C from Figure 5.1, where line L meets the boiling point curve. This is the new state of our system.

5. From the new densities at point C, calculate the fluid pressure P_f.

6. From the pressure P_f, calculate the specific entropies s_v and s_l (using the equation of state).

7. Using the entropy conservation Equation 5.10 calculate the new volume fractions ϕ_v and ϕ_l. This is a measure of how much boiling has taken place.

8. Calculate the new velocity using Equation 5.18 and relax the fluid velocity.

9. Repeat for next timestep.

6.4 Conclusion

In this chapter we have introduced the governing equations for 1-D vertical multi phase flow. The middle wave speed was modified to account for the gravitational weight forces which change the initial pressure profile in the shock tube. Furthermore, in Section 6.3 we summarise the full numerical method used to solve the shock tube problem for air, water vapour, and liquid water, whilst also accounting for boiling. It is this numerical method that will be used to simulate an eruption in a fully liquid reservoir in Chapter 7. We now have the tools necessary to perform our first simulations of the initiation of a hydrothermal eruption.

Chapter 7

Eruption Simulation in a Liquid Reservoir

This chapter presents the first simulations of the initiation of a hydrothermal eruption in a liquid filled reservoir using the shock tube model. To achieve this the governing equations and the numerical theory of previous chapters are used to simulate a 1-D vertical hydrothermal eruption. The governing equations, Equations 6.1 - 6.4, are repeated here for ease of reading:

$$\begin{aligned}
\frac{\partial}{\partial t}(\phi_j \rho_j) + \frac{\partial}{\partial z}(\phi_j \rho_j u_j) &= 0, \\
\frac{\partial}{\partial t}(\phi_j \rho_j u_j) + \frac{\partial}{\partial z}\left(\phi_j \rho_j u_j^2 + \phi_j P_j\right) &= P_I \frac{\partial \phi_j}{\partial z} - \phi_j \rho_j g, \\
\frac{\partial}{\partial t}(\phi_j \rho_j s_j) + \frac{\partial}{\partial z}(\phi_j \rho_j u_j s_j) &= 0, \\
\frac{\partial}{\partial t}\phi_j + V_I \frac{\partial}{\partial z}\phi_j &= 0.
\end{aligned}$$

Furthermore, the assumptions of the progressive flashing model are used. These assumptions are:

- In geothermal fields, a liquid or a two-phase mixture of water lies below the surface and is heated to boiling point conditions. The pressure and temperature follow a standard saturated pressure-temperature (boiling point with depth) curve.

- Due to an initiation event (discussed in Section 2.2) the saturated fluid is exposed to reduced pressure conditions.

- This pressure reduction allows boiling of the fluid to occur, and the fluid to expand.

- The fluid will move towards regions of lower pressure (the surface), and the movement of this fluid will provide lift to the rock above.

- When the cohesive and weight forces are exceeded by the lift provided by the fluid velocity, the eruption will break the surface and a column of vapour/liquid water mix will be ejected, taking some rock along with it.

- As the fluid and rock are ejected upwards, the depressurization path moves down further into the ground, causing the boiling front to move down further, and more material and fluid to be ejected.

- Some of the ejected material falls back into the eruption column and is re-ejected.

- This process will continue until some terminating mechanism occurs. This may include the hot water recharge running out, cold inflows from other parts of the aquifer, or the boiling front meeting an impermeable layer of rock.

- The principles of conservation of mass, momentum and energy hold, and are governed by the equations given further on in this Section.

- The fluid below the flashing zone is motionless.

- The fluid flowing is a homogeneous mixture of liquid water and water vapour. Due to the fact that the boiling processes occur rapidly, time is not available for the two separate phases to be established in their passage to the surface.

- The moving fluid is at saturated (boiling) conditions.

- Thermal conduction is ignored, i.e., there is no heat transfer between the fluid and rock in the flashing zone. The process is modelled as being adiabatic.

Figure 7.1 is a schematic of the initial configuration before a hydrothermal eruption in a liquid reservoir (i.e. no flow through porous medium). We have a region of liquid water at boiling point conditions below a region of air. At the interface of the water and air there is some discontinuous pressure jump.

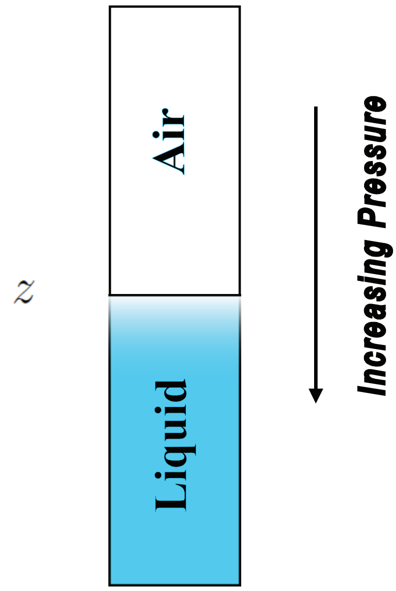

Figure 7.1: *A schematic of the shock tube model. In the lower half of the column we have liquid water, while in the upper half we have air.*

It is this pressure difference that causes the liquid water to flash to water vapour and drive the eruption. Note that there is no porous medium present in this setup. The effects of flow through a porous medium will be accounted for in a subsequent chapter.

We are interested in three main outputs from our simulations:

1. How far and fast does the flashing front (boundary of boiled/unboiled water) travel down into the geothermal reservoir?

2. How far and fast does the eruption jet travel up above the ground surface?

3. How much of the liquid water is boiled to water vapour?

These three questions will be analysed for various values of ΔP, the pressure jump at the boundary of the water and air interface.

7.1 The Pressure Jump at the Water-Air Interface

The driving force of a hydrothermal eruption using the shock tube model is the pressure difference, ΔP, at the interface between the water and air. We have two options when choosing the location of the pressure jump at the water-air boundary: We may have an atmospheric pressure water and reduced pressure air, or we may have an atmospheric pressure air and an increased pressure water. For example, with a pressure jump $\Delta P = 0.5atm$, we may have the pressure of the water at the boundary $P_W = 1atm$ and the air pressure $P_A = 0.5atm$, which we will denote by ΔP^A. Alternatively, we may have the air pressure $P_A = 1atm$ and the pressure of the water at the boundary $P_W = 1.5atm$. We denote this situation by ΔP^B. In both cases the pressure jump is $0.5atm$, the difference being in which fluid the pressure jump is taking place. This difference accounts for separate eruption triggering mechanisms, for example, we may have the ΔP^B situation (atmospheric air, high pressure water) in the case of a landslide or a crack in the reservoir generated by an earthquake. We may have an atmospheric pressure water and low pressure air (ΔP^A situation) in the case of a rapid reduction in atmospheric presure. These triggering mechanisms are discussed in [69], [34], [38], [54], [35]. It is worth noting that the ΔP^B situation is more physically realistic, especially for large pressure jumps.

7.2 Simulation of an Eruption in a Liquid Filled Geothermal Reservoir

This section includes specific initial conditions for our simulation of a hydrothermal eruption in a liquid reservoir using the shock tube model. We also report our results in this section. The natural pressure profile of the fluid away from the boundary is given by the differential equation:

$$\frac{\partial}{\partial z} P_f = -g\rho_f,$$

which is Equation 6.5 where $P_f = \sum_j \phi_j P_j$ and $\rho_f = \sum_j \phi_j \rho_j$. A space step $\Delta z = 0.25m$ was used to simulate a $100m$ deep reservoir and $100m$ above the water/air boundary. The timestep used was $\Delta t = 7.5 \times 10^{-5}s$ and a total time of $0.9s$ was simulated. Initially all the water under the ground is liquid and none is vapour, however, for the sake of our numerical method, we must give ϕ_v a non-zero value. This is a common method in this kind of modelling, see [4] for example. We choose the initial $\phi_v = 1 \times 10^{-6}$ in the groundwater domain which represents a liquid filled reservoir.

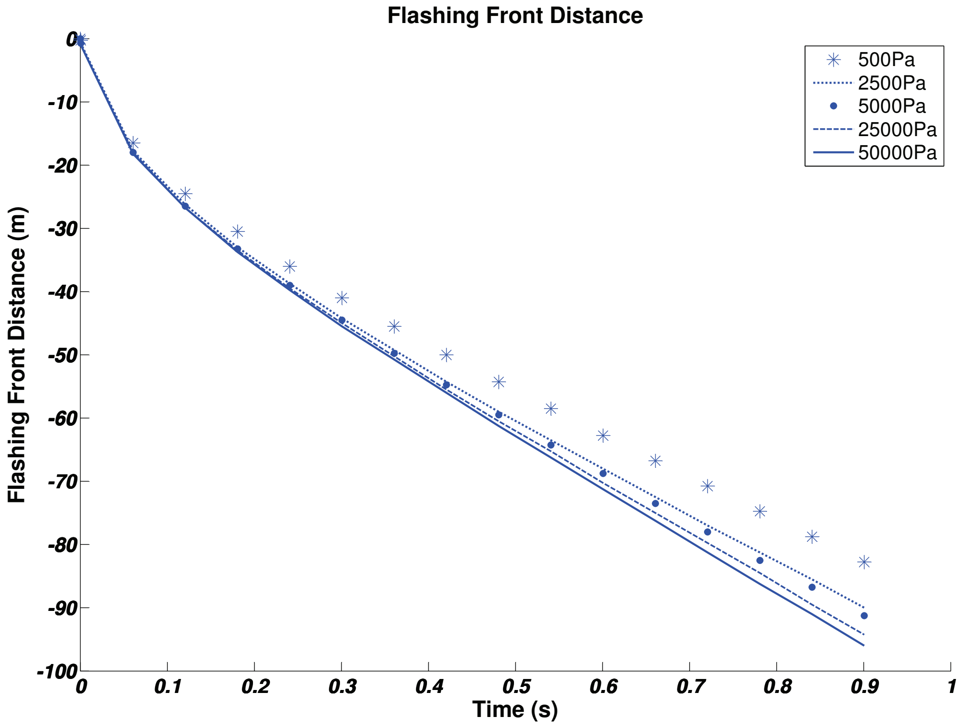

Figure 7.2: *The position of the flashing front as a function of time for various* ΔP^A.

Figure 7.2 is a plot of the position of the flashing front for various ΔP^A. The boiling front travels very rapidly into the geothermal reservoir, with the front reaching at least $80m$ in less than a second for all initial pressure differences. Furthermore, the effect of the pressure difference ΔP^A on the distance the front travels into the reservoir is minor, with the $50000Pa$ front traveling only approximately 1.2 times further than the $500Pa$ front, despite a 100 times larger pressure difference. The profile shape of the flashing front is also interesting and worthy of note. In the classical shock tube model, the speed of this front should be constant. In fact, if we allow all three fluid phases to evolve with their own velocities then this is also the case for our model and we get a constant velocity flashing front. However, Equation (5.18) describes the common (mass averaged) velocity of the three phases. A common velocity for the total fluid is more physically realistic, since any phases flowing together will interact, exchanging mass, momentum, and energy. This change in the velocity of the phases causes a change in momentum between the phases and acts like a viscous force, slowing the speed of the flashing front, and hence the speed of the front is not constant as seen in Figure 7.2. Figure 7.3 shows the position of the eruption jet above the ground surface for various ΔP^A. The eruption jet travels much slower than the flashing front which is expected from shock tube theory. The value of the pressure difference ΔP^A has a large effect on the speed of the eruption jet. The $50000Pa$ front travels approximately 75 times further than the $500Pa$ front, for the 100 times larger pressure difference. This implies that significant above ground flow during a hydrothermal eruption will require a large pressure difference to drive the flow.

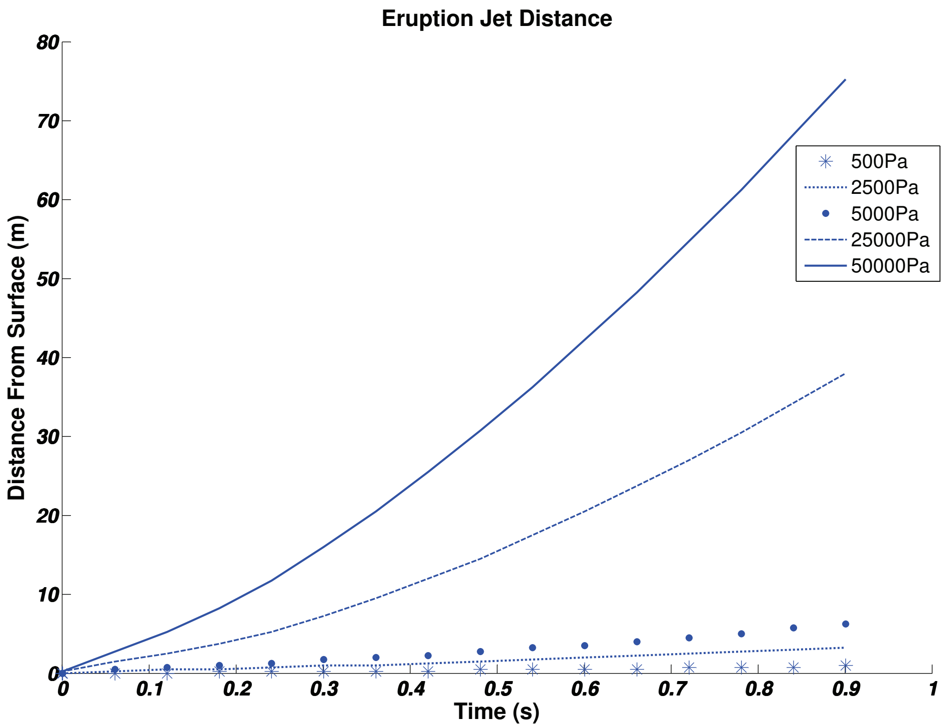

Figure 7.3: *The position of the eruption jet as a function of time for various* ΔP^A.

Table 7.1 gives information about the system at time $0.9s$ after initiation of the eruption for various pressure differences ΔP. The table also shows whether the pressure difference was in the air, ΔP^A, or in the water, ΔP^B.

Table 7.1: Flashing front position, eruption jet position, and the amount of boiling at 0.9s.

ΔP (Pa)	500	2500	5000	25000	50000
ΔP^A					
D_F (m)	82.75	90.00	91.25	94.25	96.00
D_E (m)	1.00	3.25	6.25	38.00	75.25
ϕ_v	0.199	0.578	0.736	0.955	0.980
ΔP^B					
D_F (m)	82.50	89.75	90.75	92.00	92.75
D_E (m)	1.00	3.25	6.00	28.00	43.00
ϕ_v	0.198	0.574	0.728	0.937	0.958

From the table, we see that both the flashing front distance, D_F, and the eruption jet distance, D_E, are affected by whether our pressure difference was in the water or air. In both cases the flashing front and the eruption jet travel further when the water is at atmospheric pressure (that is, pressure drop in the air phase, corresponding to ΔP^A). However, the eruption jet is effected much more than the flashing front. Furthermore, if we look at the amount of liquid water boiled to vapour, ϕ_v in the table, we see that more boiling occurs for ΔP^A than when we use ΔP^B. It is initially unclear why this should be the case, since in both circumstances the pressure differences themselves are the same. On closer inspection, however, it becomes evident why this occurs. Even though the pressure difference at the water/air boundary is the same in both the ΔP^A and ΔP^B cases, the difference in the fluid densities and fluid entropies is not. In fact, we found that the difference in these variables was significantly greater in the ΔP^A case, thus giving us more potential for boiling to occur by Equation (8.34). However, the ΔP^B situation is a more physically likely result at higher pressure differences, since an air pressure of 0.5atm is highly unrealistic. Figure 7.4 also shows the difference in the volume fraction of vapour at time 0.9s for ΔP^A and ΔP^B. It shows how much boiling occurs as a function of pressure difference. For a 500Pa pressure difference, only around 20% of the liquid water is boiled to vapour.

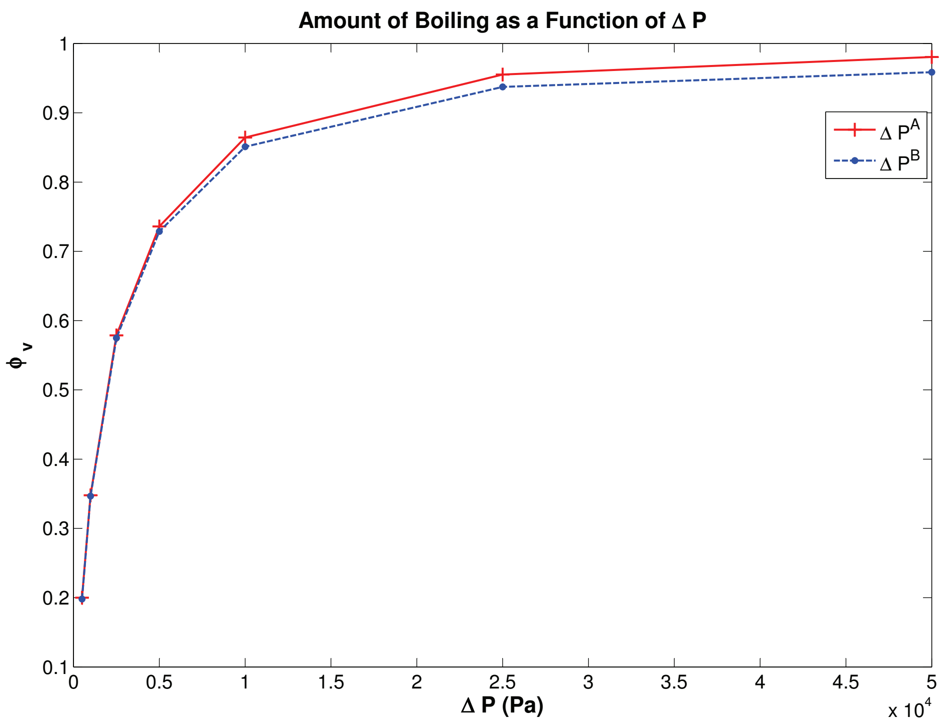

Figure 7.4: *The maximum fraction of liquid water boiled to water vapour at time* $0.9007s$ *as a function of* ΔP*.*

This is the major factor that contributes to these eruptions being smaller than those with larger pressure differences, since the phase change of the water is the major driving force of a hydrothermal eruption. The larger the pressure difference, the more boiling, the larger the eruption. This implies that the biggest eruptions will occur when all the water below the ground is liquid water. Any condensed gas present in the liquid water (a larger fraction of water vapour, for example) will reduce the size of an eruption, since there is less phase change taking place.

7.3 Conclusions

In this chapter we have used the shock tube model to simulate a hydrothermal eruption in a liquid reservoir. The eruption jet is highly dependent on the pressure difference, but travels much slower than the flashing front. This is directly due to the amount of boiling which occurs. The flashing front was shown to have only small dependence on the initial pressure difference, but travelled very quickly into the geothermal reservoir. This raises some questions: since the flashing front travels so fast into the reservoir, how do some eruptions last hours, even days? Is there some sort of water recharge allowing the replenishment of the liquid water for further boiling, prolonging the eruption? What pressure difference is sufficient to cause enough boiling to initiate an eruption big enough to break the ground surface? These questions will be the focus of the remainder of this thesis, which will include taking into account the flow through porous medium via Darcy's Law. Future research will need to extend the governing equations and numerical method to handle 2-D flow. This is beyond the scope of this thesis. The inclusion of the Darcy terms should slow the eruption jet due to viscous dissipation. Extending the model to two dimensions will allow for potential liquid water recharge, which is likely to be the main factor in long lasting eruptions. Also, a 2-D model should be able to simulate the development of any craters formed by an eruption.

Chapter 8

Hydrothermal Eruptions in a Porous Geothermal Reservoir

The results achieved in Chapter 7 do not take into account viscous dissipation due to the fact that the fluids are flowing through a porous medium, nor do they account for heat transfer between the fluids and the rock. Due to the fact that we are modelling the initiation of an eruption we assume that there is not enough time for heat transfer effects to have an impact on our simulations. The current chapter deals with modifying the governing equations and numerical method to account for the viscous dissipation caused by flow through a porous medium. Chapter 9 will use the theory developed in the current chapter to simulate an eruption in a geothermal reservoir.

8.1 Modifications for Flow Through a Porous Medium

The assumptions listed in Section 7 are used to simulate a hydrothermal eruption in a porous medium. Figure 8.1 is a schematic of the initial configuration before a hydrothermal eruption. We have a chamber of liquid water at boiling point conditions below a chamber of air. At the interface of the water and air there is some discontinuous pressure jump. It is this pressure difference that causes the liquid water to flash to water vapour and drive the eruption. Note that the liquid chamber is also filled with some porous solid with porosity ϵ.

We describe the flow of these fluids by modifications to the multiphase

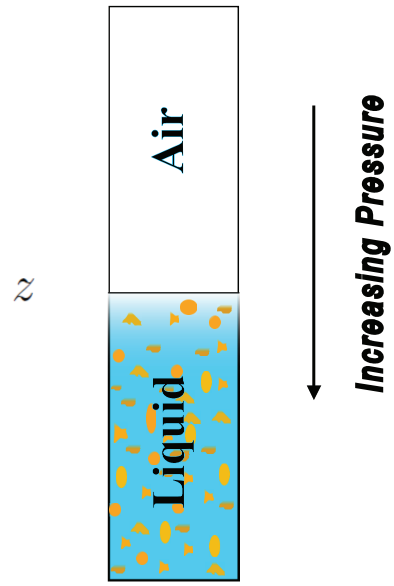

Figure 8.1: *A schematic of the shock tube model. In the lower half of the column we have liquid water in a porous medium, while in the upper half we have air.*

Euler equations, 6.1 - 6.4, of Section 6.3. The equations have been modified in this section to include viscous dissipation due to flow and drag through a porous medium.

$$\begin{aligned}
\frac{\partial}{\partial t}\left(\epsilon\phi_j\rho_j\right)+\frac{\partial}{\partial z}\left(\epsilon\phi_j\rho_j u_j\right) &= 0 && (8.1)\\
\frac{\partial}{\partial t}\left(\epsilon\phi_j\rho_j u_j\right)+\frac{\partial}{\partial z}\left(\epsilon\phi_j\left(\rho_j u_j^2+P_j\right)\right) &= S_j-\delta\delta_s D_j-\left(1-\delta\right)\delta_s L_j && (8.2)\\
\frac{\partial}{\partial t}\left(\epsilon\phi_j\rho_j s_j\right)+\frac{\partial}{\partial z}\left(\epsilon\phi_j\rho_j u_j s_j\right) &= 0 && (8.3)\\
\frac{\partial}{\partial t}\phi_j+V_I\frac{\partial}{\partial z}\phi_j &= 0, && (8.4)
\end{aligned}$$

where $S_j = P_I \dfrac{\partial\left(\epsilon\phi_j+\epsilon\right)}{\partial z} - \phi_j\rho_j g$. Here ϕ_j, ρ_j, u_j, P_j, and s_j are the volume fraction, density, velocity, pressure, and specific entropy of phase $j = a, v, l$ (air, vapour, liquid respectively) as before. g is the acceleration due to gravity which acts in the z (vertical) direction. P_I and velocity V_I are the interface pressure and speed given in [64] as

$$P_I = \sum_j \phi_j P_j,$$
$$V_I = \frac{\sum_j \phi_j\rho_j u_j}{\sum_j \phi_j\rho_j}.$$

The presence of the derivative term $(P_I \dfrac{\partial\left(\epsilon\phi_j+\epsilon\right)}{\partial z})$ on the right hand side of the momentum equation, Equation 5.2, arises from the fact that changes in the volume fraction of each phase and changes in the porosity of the medium can act to accelerate a flow. For further details see [13], [56], [8], [20]. The drag and lift terms (D_j, L_j) in the momentum equation describe the transfer of momentum between each individual fluid phase and the porous medium itself. They are given by simple modifications to relations in [46] and [2] by

$$
\begin{aligned}
D_j &= \frac{\mu_j(\epsilon\phi_j)^2}{k_j}(u_j - u_s) + \frac{\rho_j c_F(\epsilon\phi_j)^3}{\sqrt{k_j}}|u_j - u_s|(u_j - u_s), && (8.5)\\
L_j &= \frac{3}{4}c_F\phi_j\frac{1-\epsilon}{\epsilon d_p}\rho_j|u_j - u_s|(u_j - u_s). && (8.6)
\end{aligned}
$$

k_j is the relative permeability of phase j, given by $k_j = \phi_j k$ where k is the permeability of the porous medium. c_F is a drag coefficient, μ_j is the dynamic viscosity of phase j, d_p is a representative size for particles ejected from the porous medium, and u_s is the velocity of the ejected solid porous medium. The extra Equation (4.4) expresses the evolution of the volume fraction and was derived in [27]. Note that an appropriate equation of state must be provided for each fluid phase. We also describe the motion of the porous medium as it is transported by the moving fluid phases. We ignore any thermal conduction between the fluids and the porous medium and treat the medium itself as incompressible, hence we have an equation for the conservation of mass and momentum of the porous medium, as well as an equation describing the change in the porosity as the medium is moved.

$$
\begin{aligned}
\frac{\partial}{\partial t}\rho_s &= 0 && (8.7)\\
\frac{\partial}{\partial t}(\epsilon\phi_s\rho_s u_s) &= \delta\delta_s D_j + (1-\delta\delta_s)L_j - (1-\epsilon)\rho_s g && (8.8)\\
\frac{\partial}{\partial t}(1-\epsilon) + u_s\frac{\partial}{\partial z}(1-\epsilon) &= 0. && (8.9)
\end{aligned}
$$

The δ terms are used to distingush the flow profile at any given time. δ_s informs us if there is any solid phase present in any given cell, while δ tells us if that solid phase is stationary or moving with some velocity u_s. At any given point on the flow we may have fluid flowing with no interaction with the porous medium (atmospheric), fluid flowing through a porous medium (underground), or fluid transporting porous medium (eruption jet). Many relations are possible for δ and δ_s. We choose the following simple definitions:

$$\delta_s = \begin{cases} 0 & \text{if } (1-\epsilon) = 0 \\ 1 & \text{otherwise} \end{cases} \tag{8.10}$$

$$\delta = \begin{cases} 1 & \text{if } u_s = 0 \\ 0 & \text{otherwise} \end{cases} \tag{8.11}$$

The final important process we must modify for the effects of the porous medium is the flashing of liquid water to water vapour. This is the engine of the eruption since the large volume expansion of the fluid when it boils from liquid water to vapour provides the necessary lift to initiate ejection of solid material. This will be described fully in the Numerical Method Section 8.2. These equations can now be used to describe the initiation and eruption process.

8.2 Numerical Method

The numerical method to solve this problem is modified from that of Chapters 4 - 5. We modify the three parts of the method individually:

1. The advection/source term solver – this advances the system of equations 8.1 - 8.4 and 8.7 - 8.9 taking into account the three-phase flow through the porous medium.

2. A relaxation step – this brings the system back onto the boiling point with depth equation of state.

3. The evaporation routine – this accounts for the phase change of liquid water to water vapour (steam).

8.3 The Advection Solver

The first step in simulating the initiation of a hydrothermal eruption involves solving the advection problem. We must solve the system of Equations 8.1 - 8.4 and 8.7 - 8.9. The basis for the numerical scheme used to achieve this is described (in the case of no porous medium) in Chapter 4. The scheme is modified here to account for the fact that part of our flow may occur in a porous medium in Section 8.3.1. Since we will be dealing with discontinuous initial data (the pressure jump at the boundary of the water and air, hence the name shock-tube) we must use the finite volume framework to discretize our system of equations. We split the spatial domain into $N_z = \dfrac{L_z}{\Delta z}$ intervals, where N_z is the number of intervals, L_z is the total length of the spatial domain, and Δz is the length of the cell. We then split the time domain analogously with $N_t = \dfrac{L_t}{\Delta t}$. We define the i'th grid cell on any particular time level by $C_i = (z_{i-1/2}, z_{i+1/2})$. Using this definition, the length of the cell becomes $\Delta z = z_{i+1/2} - z_{i-1/2}$. Therefore the discretised system at time level n is given by:

$$\mathbf{Q}_i^{n+1} = \mathbf{Q}_i^n - \frac{\Delta t}{\Delta z}\left(\mathbf{F}_{i+1/2}^n - \mathbf{F}_{i-1/2}^n\right) - \frac{\Delta t}{\Delta z}\mathbf{F}_{LAG,i}^n. \tag{8.12}$$

$\mathbf{Q}$ is the vector of conserved variables and $\mathbf{F}$ the vector of fluxes. They correspond to the t and z partial derivatives in the system of Equation 8.1 - 8.4. $\mathbf{F}_{LAG}$ is the Lagrangian flux and is the vector of spatial derivatives on the right hand side of the momentum Equation 5.2. Explicitly, these are given by

$$\mathbf{Q} = \begin{bmatrix} \epsilon\phi_v\rho_v \\ \epsilon\phi_v\rho_v u_v \\ \epsilon\phi_v\rho_v s_v \\ \\ \epsilon\phi_l\rho_l \\ \epsilon\phi_l\rho_l u_l \\ \epsilon\phi_l\rho_l s_l \\ \\ \epsilon\phi_a\rho_a \\ \epsilon\phi_a\rho_a u_a \\ \epsilon\phi_a\rho_a s_a \end{bmatrix}, \tag{8.13}$$

$$
\mathbf{F} = \begin{bmatrix} \epsilon\phi_v\rho_v u_v \\ \epsilon\phi_v\rho_v u_v^2 + \epsilon\phi_v P_v \\ \epsilon\phi_v\rho_v u_v s_v \\ \\ \epsilon\phi_l\rho_l u_l \\ \epsilon\phi_l\rho_l u_l^2 + \epsilon\phi_l P_l \\ \epsilon\phi_l\rho_l u_l s_l \\ \\ \epsilon\phi_a\rho_a u_a \\ \epsilon\phi_a\rho_a u_a^2 + \epsilon\phi_a P_a \\ \epsilon\phi_a\rho_a u_a E_a \end{bmatrix}, \tag{8.14}
$$

and

$$
\mathbf{F}_{LAG} = \begin{bmatrix} 0 \\ P_I \dfrac{\partial\left(\epsilon\phi_v + \epsilon\right)}{\partial z} \\ 0 \\ \\ 0 \\ P_I \dfrac{\partial\left(\epsilon\phi_l + \epsilon\right)}{\partial z} \\ 0 \\ \\ 0 \\ P_I \dfrac{\partial\left(\epsilon\phi_a + \epsilon\right)}{\partial z} \\ 0 \end{bmatrix}. \tag{8.15}
$$

The remaining source terms on the right hand side of the momentum Equation 5.2 and the solid Equations 8.7 - 8.8 will be solved simultaneously in the standard way, by solving a system of ODEs arising from the fractional step method, see [72], [52].

8.3.1 The Three-Phase Porous Medium Solver

The numerical scheme tasked to solve the three-phase flow through porous medium is an advancement of the three-phase solver from Chapter 4. The system is split into weighted smaller systems and the smaller systems solved using the HLLC framework. Consider a flow with three distinct phases: v, l, and a respectively. We assign a weight, ω_{xx}, to each interaction.

Self Interactions. The self-interactions are defined as:

$$\begin{aligned}
\omega_{vv}^{i} &= \min\left\{\epsilon_i\phi_{v,i}\ ,\ \epsilon_{i+1}\phi_{v,i+1}\right\}, \\
\omega_{ll}^{i} &= \min\left\{\epsilon_i\phi_{l,i}\ ,\ \epsilon_{i+1}\phi_{l,i+1}\right\}, \\
\omega_{aa}^{i} &= \min\left\{\epsilon_i\phi_{a,i}\ ,\ \epsilon_{i+1}\phi_{a,i+1}\right\},
\end{aligned} \tag{8.16}$$

for all cells i. The subscripts on ω represent the interactions (e.g. v in a v-v interaction). The ϕ subscripts represent the phase and the cell (e.g $\phi_{x,i}$ is the void fraction of phase x in cell i). This definition is analogous to the definition given for the case when no porous medium is present, as in Equation 4.22.

Separate Fluid Interactions. We recall the concept of a common border between phases from Section 4.4, see Figure 4.2. We must now account for the fact that most of the volume is taken up by the porous medium itself. Under this new situation, conditions for this common border to exist for a v-a interaction are $\epsilon_i\phi_{v,i} > \epsilon_{i+1}\phi_{v,i+1}$ and $\epsilon_{i+1}\phi_{a,i+1} > \epsilon_i\phi_{a,i}$, that is, phase v in cell i has a border on the right of the cell to 'donate' or 'receive' flux to or from phase a, and phase a in cell $i+1$ has a border on the left of the cell to 'donate' or 'receive' flux to or from phase v. Again, the middle wave speed determines which is the donating phase and which is the receiving phase. Should the middle wave speed be positive then the phase in the left cell i is the donating phase and the phase in the right cell $i+1$ is the receiving phase. For a negative middle wave speed the roles of the phases are reversed. Table 4.2 below shows the necessary conditions for a common border to exist between two different phases with the assumption of the fluid moving through a porous medium. S_{xy}^{*} is the middle wave speed between phases x in cell i and y in cell $i+1$, given by

$$S_* = \frac{P_R - P_L + \rho_R g\Delta z + \rho_L u_L\left(S_L - u_L\right) - \rho_R u_R\left(S_R - u_R\right)}{\rho_L\left(S_L - u_L\right) - \rho_R\left(S_R - u_R\right)},$$

which is Equation 6.10. If, for any interactions between two different fluids, the conditions in Table 8.1 are met then there will be a transfer of flux from one cell to the other.

Table 8.1: Conditions for a common border between phases (three-phase)

Cells $_{(i,i+1)}$	Cond. 1	Cond. 2
v, a	$\epsilon_i\phi_{v,i} > \epsilon_{i+1}\phi_{v,i+1}$	$\epsilon_{i+1}\phi_{a,i+1} > \epsilon_i\phi_{a,i}$
a, v	$\epsilon_i\phi_{a,i} > \epsilon_{i+1}\phi_{a,i+1}$	$\epsilon_{i+1}\phi_{v,i+1} > \epsilon_i\phi_{v,i}$
v, l	$\epsilon_i\phi_{v,i} > \epsilon_{i+1}\phi_{v,i+1}$	$\epsilon_{i+1}\phi_{l,i+1} > \epsilon_i\phi_{l,i}$
l, v	$\epsilon_i\phi_{l,i} > \epsilon_{i+1}\phi_{l,i+1}$	$\epsilon_{i+1}\phi_{v,i+1} > \epsilon_i\phi_{v,i}$
l, a	$\epsilon_i\phi_{l,i} > \epsilon_{i+1}\phi_{l,i+1}$	$\epsilon_{i+1}\phi_{a,i+1} > \epsilon_i\phi_{a,i}$
a, l	$\epsilon_i\phi_{a,i} > \epsilon_{i+1}\phi_{a,i+1}$	$\epsilon_{i+1}\phi_{l,i+1} > \epsilon_i\phi_{l,i}$

Calculating the Weights The definition of the interaction weights for the porous medium case is analogous to that of Section 4.4.1, Equations 4.24, 4.25, 4.32.

$$\Omega^{I+}_{x,i} = \max(0\ ,\ \epsilon_i\phi_{x,i} - \epsilon_{i+1}\phi_{x,i+1}), \tag{8.17}$$

$$\Omega^{I-}_{y,i+1} = \max(0\ ,\ \epsilon_{i+1}\phi_{y,i+1} - \epsilon_i\phi_{y,i}). \tag{8.18}$$

The definition for the weights between fluids x and y is then

$$\omega^i_{xy} = \begin{cases} 0 \quad \text{if} \quad \text{Table 8.1 conditions unsatisfied} \\ \Omega^{I+}_{x,i}\left(\dfrac{\Omega^{I-}_{y,i+1}}{\Omega^{I-}_{z,i+1} + \Omega^{I-}_{y,i+1}}\right) \quad \text{otherwise.} \end{cases} \tag{8.19}$$

Calculating the Flux. Once the weights have been calculated we calculate the intercell flux as in the case without porous media. The flux is defined as

$$\begin{aligned} \mathbf{F}_{i+1/2} = {} & \omega_{vv}\mathbf{F}^{vv}_{i+1/2} + \omega_{ll}\mathbf{F}^{ll}_{i+1/2} + \omega_{aa}\mathbf{F}^{aa}_{i+1/2} + \\ & \omega_{vl}\mathbf{F}^{vl}_{i+1/2} + \omega_{lv}\mathbf{F}^{lv}_{i+1/2} + \omega_{va}\mathbf{F}^{va}_{i+1/2} + \\ & \omega_{av}\mathbf{F}^{av}_{i+1/2} + \omega_{al}\mathbf{F}^{al}_{i+1/2} + \omega_{la}\mathbf{F}^{la}_{i+1/2}. \end{aligned} \tag{8.20}$$

The fluxes $\mathbf{F}^{xy}_{i+1/2}$, where x and y can be fluid v, l, or a, are calculated by solving the Riemann problem for a single-phase system using the HLLC Riemann solver;

$$\begin{aligned} & \mathbf{U}_t + \mathbf{F}_z = \mathbf{0}, \\ & \mathbf{U}(z,0) = \begin{cases} \mathbf{U}_L = \mathbf{U}^x_i \quad \text{if} \quad z < z_{i+1/2}, \\ \mathbf{U}_R = \mathbf{U}^y_{i+1} \quad \text{if} \quad z > z_{i+1/2}. \end{cases} \end{aligned} \tag{8.21}$$

Once the flux is calculated using Equation 8.20 it can be substituted into Equation 8.12 to advance the time of the system.

Calculating the Lagrangian Flux, $\mathbf{F}_{LAG}$ Calculating the F_{LAG} terms in Equation 8.12 must be done in two separate parts. The first, which we will call F_{LAG1}, takes into account the acceleration of the flow due to changes in the volume fraction of the fluid phase itself. This is analogous to Equation 4.36 in the case with no porous medium. The second part, which we will call F_{LAG2}, is present due to changes in the porosity of the porous medium itself.

Calculation of F_{LAG1} can be done analogously to the flux in Equation 8.20. It is derived in [3] using Rankine-Hugoniot relations; see also [72]. This treatment of the F_{LAG1} terms differs from [19] but is closer to the discrete equations method of [4], [3]. Let the function

$$\operatorname{sign}(x) = \begin{cases} 1 \text{ if } x > 0 \\ -1 \text{ if } x < 0 \\ 0 \text{ if } x = 0 \end{cases} \tag{8.22}$$

account for the direction of the flux transfer (from cell i to $i+1$ or vice versa). We can then define F_{LAG1} for phase v (analogously phase l or a) by

$$\begin{aligned} (\mathbf{F}_{LAG1,i})_v = \quad & M_i^{lv}\omega_{lv}\mathbf{U}_i^{lv} - M_i^{vl}\omega_{vl}\mathbf{U}_i^{vl} + \\ & m_{i-1}^{lv}\omega_{lv}\mathbf{U}_{i-1}^{lv} - m_{i-1}^{vl}\omega_{vl}\mathbf{U}_{i-1}^{vl} + \\ & M_i^{av}\omega_{av}\mathbf{U}_i^{av} - M_i^{va}\omega_{va}\mathbf{U}_i^{va} + \\ & m_{i-1}^{av}\omega_{av}\mathbf{U}_{i-1}^{av} - M_{i-1}^{va}\omega_{va}\mathbf{U}_{i-1}^{va}, \end{aligned} \tag{8.23}$$

where

$$\mathbf{U}_{lv,i} = \quad \mathbf{U}_{lv,i}\left(\mathbf{Q}_i^{(l)}, \mathbf{Q}_{i+1}^{(v)}\right) = \begin{bmatrix} 0 \\ P_{I^*}^{(l,v)} \\ 0 \end{bmatrix}_i, \mathbf{U}_{vl,i} = \mathbf{U}_{vl,i}\left(\mathbf{Q}_i^{(v)}, \mathbf{Q}_{i+1}^{(l)}\right) = \begin{bmatrix} 0 \\ P_{I^*}^{(v,l)} \\ 0 \end{bmatrix}_i$$

and analogously for $\mathbf{U}_{la,i}$, $\mathbf{U}_{al,i}$, $\mathbf{U}_{va,i}$, $\mathbf{U}_{av,i}$, and

$$M^{av} = max\left(0, \operatorname{sign}\left(S_*^{(a,v)}\right)\right), \qquad m^{av} = min\left(0, \operatorname{sign}\left(S_*^{(a,v)}\right)\right).$$

The term $P_{I^*}^{(l,v)}$ is calculated in [3] and [72] and are simply stated here as:

$$\left[P_{I^*}^{(l,v)}\right]_i \quad = \quad \left[\rho_l\left(S_*^{(l,v)} - u_l\right)(S_L - u_l) + P_l\right]_i. \tag{8.24}$$

$S_*^{l,v}$ (analogously $S_*^{v,l}$, $S_*^{l,a}$, etc.) is given by Equation 6.10, with fluid l as the left state and fluid v as the right state. S_L and S_R are given in [72] by:

$$S_L = min\left(u_L - c_L, u_R - c_R\right), \quad S_R = max\left(u_L + c_L, u_R + c_R\right). \tag{8.25}$$

The calculation of F_{LAG2}, which takes into account the acceleration of the flow due to a change in the porosity of the porous medium, is a new piece of research. We assume that each fluid in each cell must use all of its available interaction borders. When there is no porous medium this is achieved naturally using the weight functions given by Equation 8.19. However, in the presence of porous medium this will not be true since most of the available fluid space is taken up by the porous medium itself. We therefore assume that the porous medium interacts with the fluid, acting to either accelerate or decelerate the flow. The first step in this calculation is therefore to measure the length of the remaining interaction borders of each fluid. For phase v (analogously phase l or a) we calculate the remaining interaction border on the right side of cell i, $\Omega_{v,i}^{I+,Nozz}$, and the remaining interaction border on the left side of cell $i+1$, $\Omega_{v,i+1}^{I-,Nozz}$. The remaining border, $\Omega_{v,i}^{I+,Nozz}$, is given simply by subtracting everything that fluid v donates from cell i to cell $i+1$ from its original interaction boundary $\Omega_{v,i}^{I+}$. The remaining border, $\Omega_{v,i+1}^{I-,Nozz}$, is given by subtracting everything fluid v receives in cell $i+1$ from cell i from its original boundary $\Omega_{v,i+1}^{I-}$. Mathematically,

$$\Omega_{v,i}^{I+,Nozz} = \Omega_{v,i}^{I+} - \left(\omega_{vv}^i + \omega_{vl}^i + \omega_{va}^i\right), \tag{8.26}$$

$$\Omega_{v,i+1}^{I-,Nozz} = \Omega_{v,i+1}^{I-} - \left(\omega_{vv}^i + \omega_{lv}^i + \omega_{av}^i\right). \tag{8.27}$$

The nozzling term, N_{ozz}, can now be defined as the difference of these two terms

$$N_{ozz,v} = \Omega_{v,i+1}^{I-,Nozz} - \Omega_{v,i}^{I+,Nozz}. \tag{8.28}$$

Finally, we can calculate F_{LAG2} using

$$\left(\mathbf{F}_{LAG2,i}\right)_v = P_v N_{ozz,v}, \tag{8.29}$$

which can then be added to F_{LAG1} to obtain the Lagrangian flux

$$\left(\mathbf{F}_{LAG,i}\right)_v = F_{LAG1} + F_{LAG2}. \tag{8.30}$$

Once the intercell flux of Equation 8.20 and F_{LAG} of Equation 8.30 are found, they can be substituted into Equation 8.12 to advance the time of the system.

Volume Fraction and Porosity Evolution The final step in the advection solver is the calculation of the evolution of both the volume fractions of each phase and the porosity of the porous medium. We must treat these independently, since we do not want to double count the evolution of the volume fraction.

The evolution of the volume fraction, Equation 4.4, is not directly derived in [19]. However we may use the method described in [4] and [3]. The reader is referred to these references for the derivation, here we simply present the three-phase extension of this scheme.

$$\frac{\partial \phi_v}{\partial t} = \frac{1}{\Delta z} \begin{bmatrix} \epsilon_i M_i^{vl} \omega_{(vl,VF)} S_*^{(v,l)} - \epsilon_i M_i^{lv} \omega_{(lv,VF)} S_*^{(l,v)} + \\ \epsilon_{i-1} m_{i-1}^{vl} \omega_{(vl,VF)} S_*^{(v,l)} - \epsilon_{i-1} m_{i-1}^{lv} \omega_{(lv,VF)} S_*^{(l,v)} + \\ \epsilon_i M_i^{va} \omega_{(va,VF)} S_*^{(v,a)} - \epsilon_i M_i^{av} \omega_{(av,VF)} S_*^{(a,v)} + \\ \epsilon_{i-1} m_{i-1}^{va} \omega_{(va,VF)} S_*^{(v,a)} - \epsilon_{i-1} m_{i-1}^{av} \omega_{(av,VF)} S_*^{(a,v)} \end{bmatrix} \tag{8.31}$$

where the M^{vl} and m^{vl} terms are as before and the $\omega_{vl,VF}$ terms are calculated analogously to Equations 4.22 and 4.32 except without the porosity, ϵ terms present. For example, $\omega_{vv} = \min\{\phi_{v,i}\ ,\ \phi_{v,i+1}\}$, and $\omega_{(vv,VF)} = \min\{\phi_{v,i}\ ,\ \phi_{v,i+1}\}$. Note that we need to use this algorithm for the first two fluid phases only, since $\phi_a = 1 - \phi_v - \phi_l$.

For the evolution of the porosity, Equation 8.9, we use a simple discretization:

$$\frac{\partial \epsilon}{\partial t} = \frac{1}{\Delta z} \left[\epsilon_{i-1} u_s^{i-1} - \epsilon_i u_s^i \right]. \tag{8.32}$$

8.4 The Relaxation and Evaporation Solver in a Porous Medium

We must also modify the scheme used to quantify how much boiling is occurring in a given timestep. In the case when no porous medium is present Equation 5.10 is used. However, when the fluid travels through a porous medium this relation becomes

$$s_F = \epsilon \frac{\chi_a s_a \rho_a + \chi_w \Phi_v s_v \rho_v + \chi_w \Phi_l s_l \rho_l}{\chi_a \rho_a + \chi_w \Phi_v \rho_v + \chi_w \Phi_l \rho_l}, \tag{8.33}$$

where $\chi_a = \phi_a$ is the volume fraction of the air phase and $\chi_w = \phi_v + \phi_l$ is the volume fraction of the water phase (liquid water + vapour) as previously. Φ_v is the fraction of vapour in the water phase (termed the vapour water fraction), defined such that $\phi_v = \chi_w \Phi_v$ and $\phi_l = \chi_w \Phi_l$. Note also that we must have $\Phi_l + \Phi_v = 1$. Equation 5.10 is replaced in the porous medium case by

$$\Phi_v = \frac{\chi_w \rho_l (\epsilon s_l - s_F) + \chi_a \rho_a (\epsilon s_a - s_F)}{\chi_w \rho_l (\epsilon s_l - s_F) + \chi_w \rho_v (s_F - \epsilon s_v)}. \tag{8.34}$$

We can use Equation 8.34 to quantify how much liquid has been boiled to vapour using conservation of entropy. The relaxation process is the same as used in Section 8.4.

8.5 Detecting Initiation

The driving force in the shock-tube model of a hydrothermal eruption is the flashing of liquid water to water vapour. This process occurs when the water immediately below the ground surface (whose pressure profile is assumed to follow the boiling point with depth curve) is exposed to reduced pressure conditions. The principal question to be investigated then becomes, 'given a particular geometry of a geothermal reservoir, what is the pressure drop, ΔP, required to generate enough boiling and hence lift force to overcome the weight and cohesive forces of a porous medium and initiate a hydrothermal eruption?' Momentum is transfered to the solid porous medium via drag and lift forces defined by Equations 8.5 and 8.6 and is opposed by both the gravitational weight and cohesive stress of the solid medium. However, when attempting to detect initiation of an eruption, the lift forces become irrelevant since it is only present in an eruption jet, which by definition, can only form after initiation. Hence, the condition governing initiation is given by

$$\sum_j D_j > (1-\epsilon)\rho_s g + C_{pm}. \tag{8.35}$$

That is, the sum of the viscous drag forces from each phase j must exceed the sum of the gravitational weight and the cohesive stress, C_{pm}, of the porous medium. During the simultaneous integration of the drag terms in Equations 8.2 and 8.8 the initiation criterion of Equation 8.35 is tested at each timestep. If the criterion is met then we are notified and the solid phase velocity, u_s, may evolve according to the solution of the integration. However, if the initiation criterion is not met then we set the solid velocity, $u_s = 0$.

In summary, the numerical method can be represented graphically by Figure 8.2. The advection, fractional step, relaxation, and boiling/evaporation solvers are split into steps and performed in order.

8.6 Conclusion

In this chapter we modified the three phase solver of Chapter 4. These modifications were made to include viscous dissipation due to the fact that the fluids are flowing through a porous medium. This modified numerical method will be used to simulate a hydrothermal eruption in a geothermal reservoir in Chapter 9. We can now make the first simulations of the initiation of a hydrothermal eruption in a porous medium.

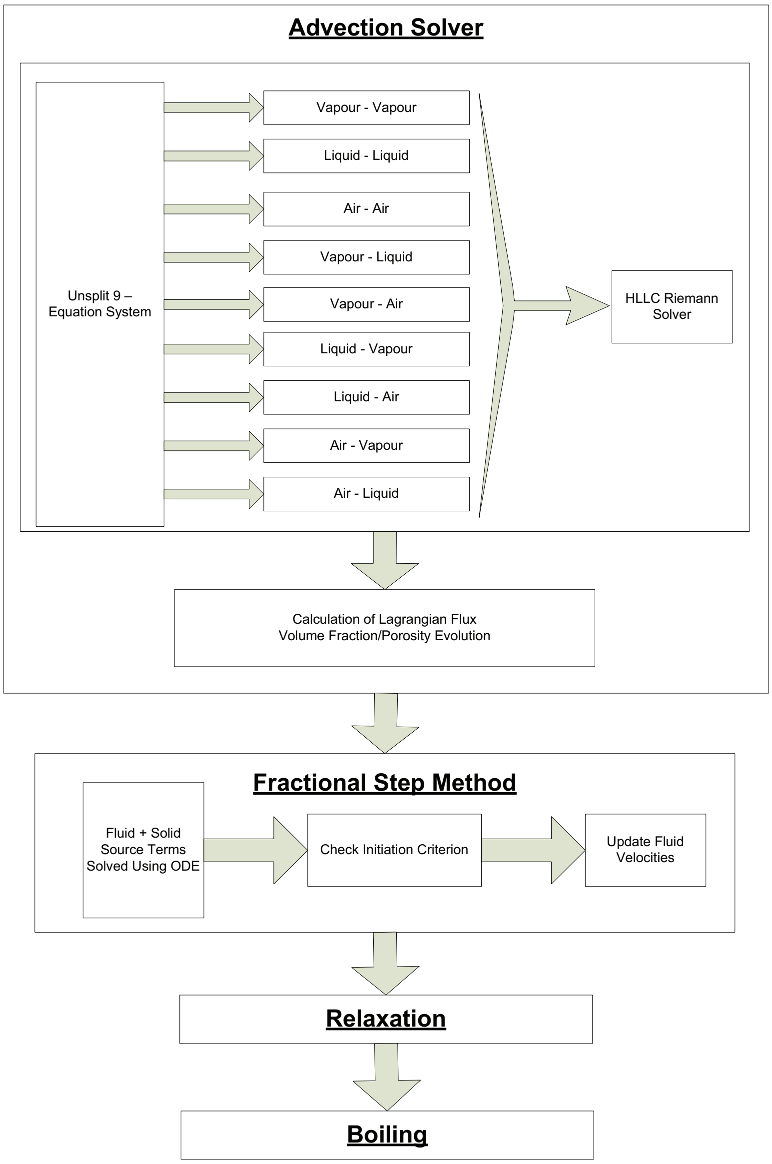

Figure 8.2: *A flow chart summary of the numerical method used to solve the shock-tube equations*

Chapter 9

Simulation of an Eruption in a Porous Geothermal Reservoir

In this chapter, 1-D vertical simulations are performed to analyse the effect of various parameters on hydrothermal eruptions. We are interested in both geometric effects (e.g. porosity, permeability) and mechanistic effects (e.g. does a 'steam cap' have an effect on an eruption?). The following sections of this chapter investigate these questions. The equations and numerical method of Chapter 8 are used, specifically, we solve the Equation set 8.1 - 8.4 and 8.7 - 8.9 and use the numerical method outlined in Section 8.2. The equations are repeated here for ease of reading.

$$
\begin{aligned}
\frac{\partial}{\partial t}\left(\epsilon\phi_j\rho_j\right)+\frac{\partial}{\partial z}\left(\epsilon\phi_j\rho_j u_j\right) &= 0,\\
\frac{\partial}{\partial t}\left(\epsilon\phi_j\rho_j u_j\right)+\frac{\partial}{\partial z}\left(\epsilon\phi_j\left(\rho_j u_j^2+P_j\right)\right) &= S_j-\delta\delta_s D_j-(1-\delta)\,\delta_s L_j,\\
\frac{\partial}{\partial t}\left(\epsilon\phi_j\rho_j s_j\right)+\frac{\partial}{\partial z}\left(\epsilon\phi_j\rho_j u_j s_j\right) &= 0,\\
\frac{\partial}{\partial t}\phi_j+V_I\frac{\partial}{\partial z}\phi_j &= 0,\\
\frac{\partial}{\partial t}\rho_s &= 0,\\
\frac{\partial}{\partial t}\left(\epsilon\phi_s\rho_s u_s\right) &= \delta\delta_s D_j+\left(1-\delta\delta_s\right)L_j-(1-\epsilon)\rho_s g,\\
\frac{\partial}{\partial t}(1-\epsilon)+u_s\frac{\partial}{\partial z}(1-\epsilon) &= 0,
\end{aligned}
$$

where

$$
\begin{aligned}
D_j &= \frac{\mu_j(\epsilon\phi_j)^2}{k_j}(u_j - u_s) + \frac{\rho_j c_F(\epsilon\phi_j)^3}{\sqrt{k_j}}|u_j - u_s|(u_j - u_s), \\
L_j &= \frac{3}{4}c_F\phi_j\frac{1-\epsilon}{\epsilon d_p}\rho_j|u_j - u_s|(u_j - u_s).
\end{aligned}
$$

9.1 Initiation Simulations

This section investigates factors that affect the initiation of a hydrothermal eruption. The main variables to be investigated are related to the 'geometry' of the geothermal reservoir. These are the porosity and permeability of the reservoir, the cohesion of the porous medium, and the initial saturation of vapour (steam) present in the reservoir. Although we will make 'predictions' for the required pressure difference at the interface for the initiation condition, Equation 8.35, to be satisfied, we are more interested in how the required pressure difference changes as we modify the porosity, permeability, and cohesion of the reservoir. We wish to investigate how these factors affect the pressure difference required to initiate a hydrothermal eruption. In each of the tests performed, the parameters of Table 9.1 were used: where

Table 9.1: Test parameters

Δz (m)	0.25
Δt (s)	7.5×10^{-5}
N	780
ρ_s (kgm^{-3})	1500
$u_i(t = 0s)$ (ms^{-1})	0
$P(z = 0m)$ (Pa)	1×10^5
$T_a(z = 0m)$ (^oC)	20
R $(Jkg^{-1}K^{-1})$	287.05
c_F	0.5
$\chi_w(z < 0)$	0.999999
$\chi_a(z > 0)$	0.999999

$z = 0m$ refers to the ground surface (the interface between the water/porous medium and the atmosphere), u_i is the initial condition that all phases are initially stationary, R is the specific gas constant for air, N is the number of computational cells used (half above $z = 0m$, half below), and T_a is the air temperature.

9.1.1 The Effect of Varying Porosity

This subsection will investigate the effect of varying porosity and cohesion on the pressure difference, ΔP, required at the interface to initiate an eruption. Simulations are run until the initiation condition of Equation 8.35 is satisfied. If, for a particular ΔP, the condition is not satisfied then we repeat the experiment with a larger pressure difference. We have performed the numerical experiment with a resolution of $10Pa$, that is, our results are accurate to $10Pa$.

The initial conditions given in Table 9.1 are used as well as the permeability, $k = 10 \times 10^{-12}$ and the initial vapour fraction, $\phi_{v0}(z < 0) = 1 \times 10^{-6}$ (that is, the reservoir is essentially fully liquid). We perform the analysis for the following range of porosity values $\epsilon = 0.1, 0.2, 0.3, 0.4, 0.5, 0.6, 0.7$. The cohesion is also varied as $C_{pm} = 0, 1000, 5000, 10000, 25000$. Figure 9.1 shows

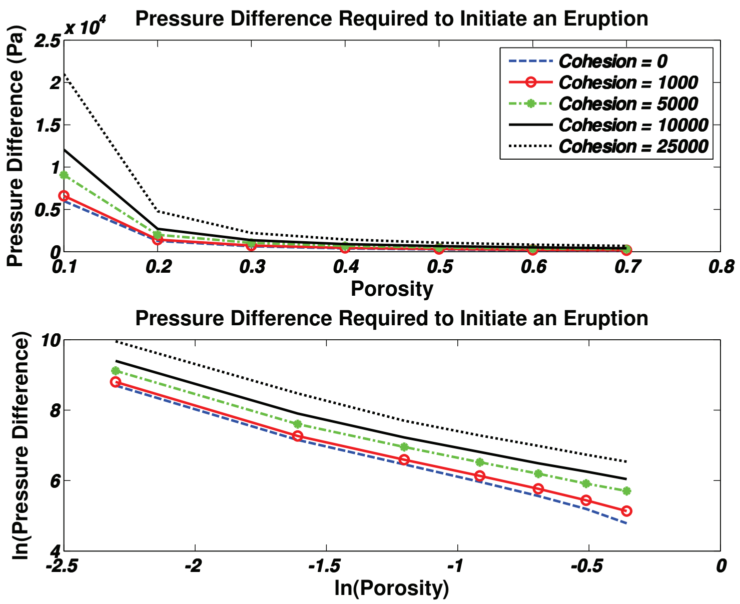

Figure 9.1: *The effect of varying porosity and cohesion.*

the relationship between the required pressure difference for initiation, ΔP, and the porosity, ϵ. The upper graph shows that ΔP is monotone decreasing as we increase the porosity ϵ. This is an expected result, since for lower values of ϵ there is less liquid water to boil, expand, and hence provide lift to the solid porous medium. Additionally, for lower values of ϵ, there is more solid phase, hence the gravitational weight force in the initiation condition 8.35 is larger, necessitating a larger ΔP to provide the extra lift and overcome the extra weight. Also shown on this graph is that increasing cohesive stress, C_{pm}, increases the pressure difference necessary to initiate an eruption. This result also follows directly from Equation 8.35, since extra lift is required to overcome the extra retarding force of cohesion.

The lower graph of Figure 9.1 is a log - log plot of ΔP and ϵ. Considering the $10Pa$ resolution used, the resulting plots are remarkably linear, with very similar gradients. Table 9.2 shows the 95% confidence interval for the slope and the R^2 fitting value. This result suggests a relationship of the form

Table 9.2: 95% confidence interval for the gradients of Figure 9.1 and their R^2 values.

C_{pm}	m (Gradient)	R^2 Value
0	$(-2.07, -1.82)$	0.9970
1000	$(-1.98, -1.69)$	0.9954
5000	$(-1.91, -1.53)$	0.9909
10000	$(-1.91, -1.49)$	0.9887
25000	$(-1.96, -1.52)$	0.9884

$\Delta P = A\epsilon^m$, where A is the intercept constant, and m the gradient. Hence we can say $\Delta P \propto \dfrac{1}{\epsilon^{1.9}}$.

9.1.2 The Effect of Varying Permeability

This subsection will investigate the effect of varying permeability on the pressure difference, ΔP, required at the interface to initiate an eruption. Again, simulations are run until the initiation condition of Equation 8.35 is satisfied. The initial conditions given in Table 9.1 are used, and the following parameters are varied for the four runs: permeability, $k = 0.5 \times 10^{-12}, 1 \times 10^{-12}, 5 \times 10^{-12}, 10 \times 10^{-12}$, porosity $\epsilon = 0.2, 0.5$, cohesion $C_{pm} = 0, 5000$.

The initial vapour fraction is given as $\phi_{v0}(z < 0) = 1 \times 10^{-6}$. Figure 9.2

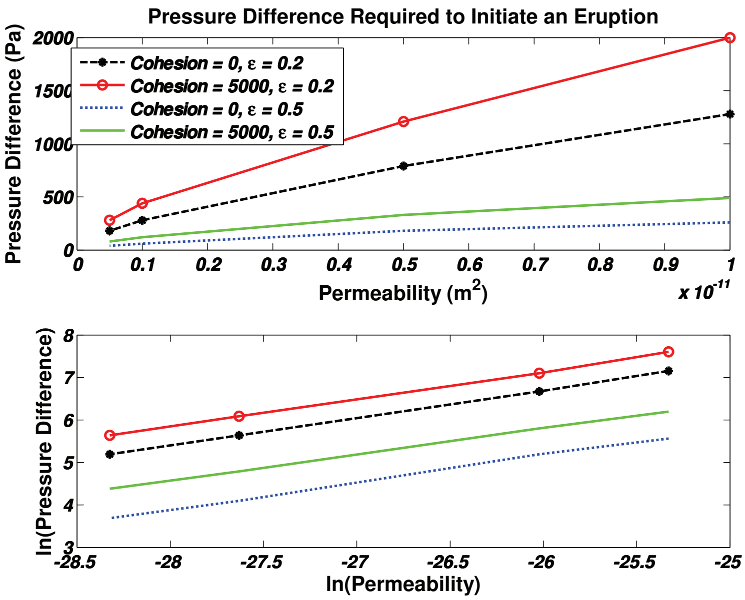

Figure 9.2: *The effect of varying permeability.*

shows a monotonic increase in ΔP as we increase the permeablity, k, of the porous medium. This is also expected, since in Equation 8.5 the drag force on the porous medium from any phase is the sum of a term inversely proportional to the permeability, and a term inversely proportional to the square root of the permeability. Permeability is essentially a measure of the ease of a porous medium to transmit fluids. Higher values of permeability allow fluids to travel through the fluid with less resistance, hence reducing the drag (lifting) force on the porous medium. This reduction of force on the porous medium must be accounted for by an increase in ΔP if we are to satisfy the initiation condition. The lower graph of Figure 9.2 is a log - log plot of ΔP and k. Again the plot is remarkably linear. Table 9.3 shows the 95% confidence interval for the slope and the R^2 fitting value. This result suggests the pressure difference required to initiate an eruption varies like $\Delta P \propto k^{0.6}$.

9.1.3 The Amount of Boiling

This section analyses the amount of boiling which has occurred at the point of initiation for varying ΔP. For each of the runs in the porosity test of Section 9.1.1 the volume fraction of vapour, ϕ_v, is noted at initiation. Figure

Table 9.3: 95% confidence interval for the gradients of Figure 9.2 and their R^2 values.

C_{pm}	ϵ	m (Gradient)	R^2 Value
0	0.2	$(0.62, 0.68)$	0.9998
0	0.5	$(0.56, 0.71)$	0.9984
5000	0.2	$(0.60, 0.70)$	0.9994
5000	0.5	$(0.58, 0.64)$	0.9997

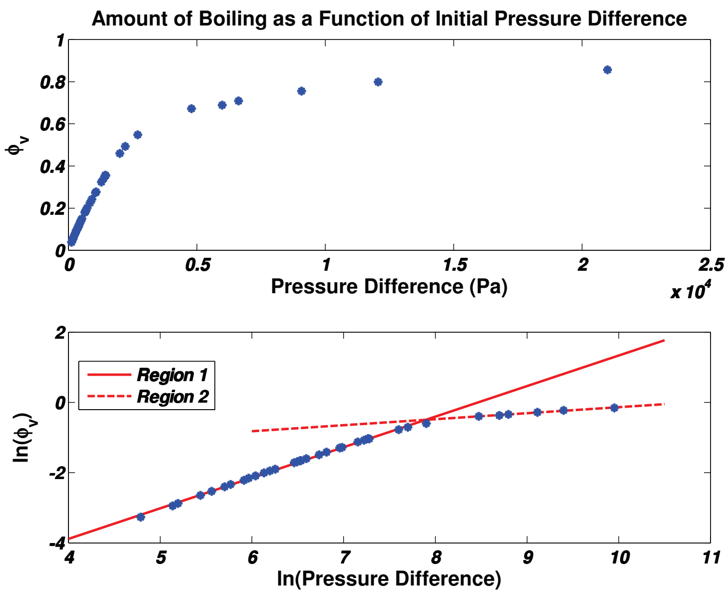

Figure 9.3: *The amount of boiling for a given* ΔP.

9.3 shows the relationship between ΔP and the amount of vapour ϕ_v (amount of boiling) present at the point of initiation. The amount of boiling increases monotonically as we increase the pressure difference between the water and atmospheric chambers. Physically this is correct, since a greater pressure difference across the interface of the two chambers necessarily produces a greater jump in the specific entropy over the interface. This greater entropic jump increases the amount of boiling via Equation 8.33. The graph also seems to show two distinct regions. This is emphasised when plotted on a log - log plot, as in the lower graph. For lower pressures, which we call Region 1, the amount of boiling increases with an increase in ΔP more rapidly than for higher pressures, Region 2. The linear least squares best fit is shown on the graph, and Table 9.4 shows the 95% confidence interval for m the slope, and also shows the R^2 values for the lines. The author hypothesises that the two

Table 9.4: 95% confidence interval for the gradients of Figure 9.3 and their R^2 values.

Region	m (Gradient)	R^2 Value
1	$(0.85, 0.89)$	0.9979
2	$(0.14, 0.20)$	0.9872

distinct regions are due to the form of the drag relation, Equation 8.5. When the $(u_j - u_s)$ term in that equation is small (which correlates with lower values of ΔP) then the Darcian term, $\frac{\mu_j(\epsilon\phi_j)^2}{k_j}(u_j - u_s)$ is dominant. However, as we increase ΔP we also increase the fluid velocities. Hence $(u_j - u_s)$ is no longer small. Therefore the Forchheimer type term, $\frac{\rho_j c_F(\epsilon\phi_j)^3}{\sqrt{k_j}}|u_j - u_s|(u_j - u_s)$, becomes significant. This addition to the drag on the porous medium causes the initiation condition, Equation 8.35, to be satisfied quicker, hence there is less time available for boiling to occur. In this way, we suppose that Figure 9.3 allows us to determine whether Darcian or Forchheimer type flow is dominating in a given region. We conclude that the Forchheimer terms are important for eruptions which require larger pressure differences to initiate them.

9.1.4 The Effect of Varying the Initial Steam Fraction

In [47], McKibbin investigates the effect of having a water vapour (and CO_2) phase present in the underground reservoir. He notes that

> *The greatest potential (for a hydrothermal eruption) is for liquid reservoir conditions; the presence of a vapour phase reduces the possible effect, with a dry system having the least capability for expansion.*

When a vapour phase is present the driving force of the eruption is reduced due to less liquid present to boil, expand, and hence, drive the eruption. This section investigates the effect of varying ϕ_{v0}, the initial vapour (steam) volume fraction. The initial conditions given in Table 9.1 are used as well as the permeability, $k = 10 \times 10^{-12}$. We perform the analysis for the porosity values $\epsilon = 0.1, 0.2, 0.3$ and cohesion $C_{pm} = 0, 5000$. We investigate initial volume fractions $\phi_{v0}(z < 0) = 1 \times 10^{-6}, 0.05, 0.1, 0.25, 0.5, 0.7, 0.9, 0.95, 0.99$.

Figures 9.4 and 9.5 show the relationship between the pressure difference

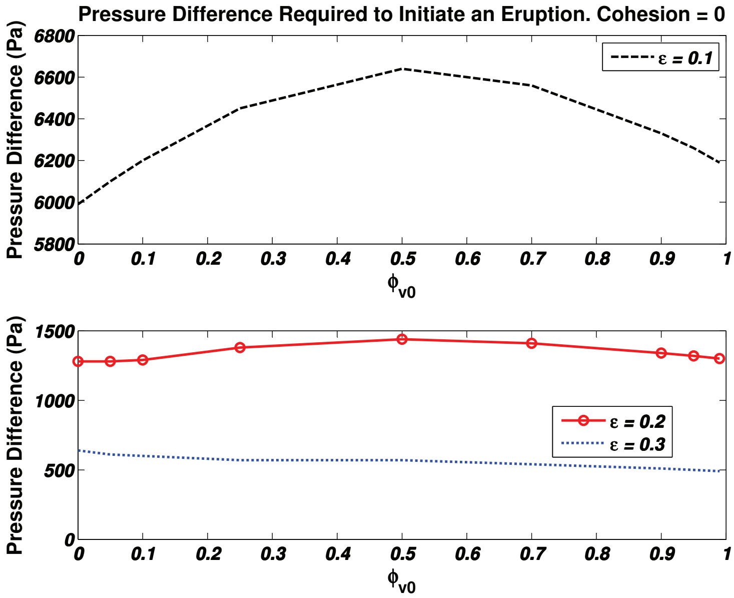

Figure 9.4: *The effect of* ϕ_{v0} *with* $C_{pm} = 0$.

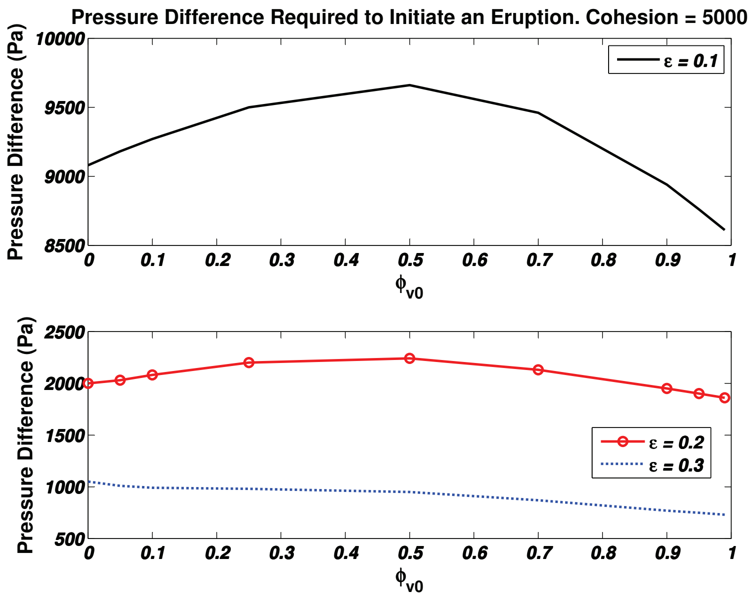

Figure 9.5: *The effect of* ϕ_{v0} *with* $C_{pm} = 5000$.

needed to initiate an eruption and the initial volume fraction of water vapour present in the geothermal reservoir. Figure 9.4 initially shows an increase in the pressure difference necessary as we increase ϕ_{v0} for $\epsilon = 0.1, 0.2$, however, at some critical value of ϕ_{v0} the pressure difference begins to drop again. For $\epsilon = 0.3$, ΔP is actually monotonically decreasing as ϕ_{v0} is increasing. Figure 9.5 shows that it is easier to initiate an eruption when the reservoir is completely vapour for all ϵ shown. This behaviour is due to the fact that the density of vapour is approximately one thousand times less than that of the liquid water. For a given ΔP, or analogously a given force applied to the fluid, the resulting acceleration of the fluid is greater when that fluid is vapour rather than liquid because of the density difference. This means the fluid flows faster when there is a high fraction of low density vapour. Due to the initiation condition of Equation 8.35, this higher velocity causes initiation to occur easier, even though other parameters such as dynamic viscosity may be working against initiation. Further light may be shed on this matter by Figure 9.6. The volume fraction of vapour due to boiling at initiation is plotted against the initial vapour fraction. The volume fraction of boiling must take into account the fact that we do not start with liquid reservoir conditions, for example, at initiation we may find $\phi_v = 0.75$, but if $\phi_{v0} = 0.25$ then our volume fraction of vapour that has been boiled is $0.75 - 0.25 = 0.5$. This figure is a measure of how important the force provided by expansion due to boiling is in the initiation process. For low values of ϕ_{v0}, boiling is dominant. It is necessary to provide the force needed to lift the porous medium into an eruption jet. This is not so for higher ϕ_{v0}, which rely on high values of velocity to provide the necessary lift. At first glace, the fact that it may be easier to initiate an eruption for high vapour concentrations seems to contradict the findings of McKibbin [47]. Yet here we are discussing the initiation of an eruption, not the eruption itself. The next subsection investigates if easily initiated eruptions due to high vapour fractions actually produce larger eruptions, or if eruptions in which boiling is dominant have more potential as McKibbin found.

The Solid Erosion and Eruption Fronts

In this subsection we test the following hypothesis: reservoirs with larger initial vapour fraction, ϕ_{v0}, values will experience smaller hydrothermal erup-

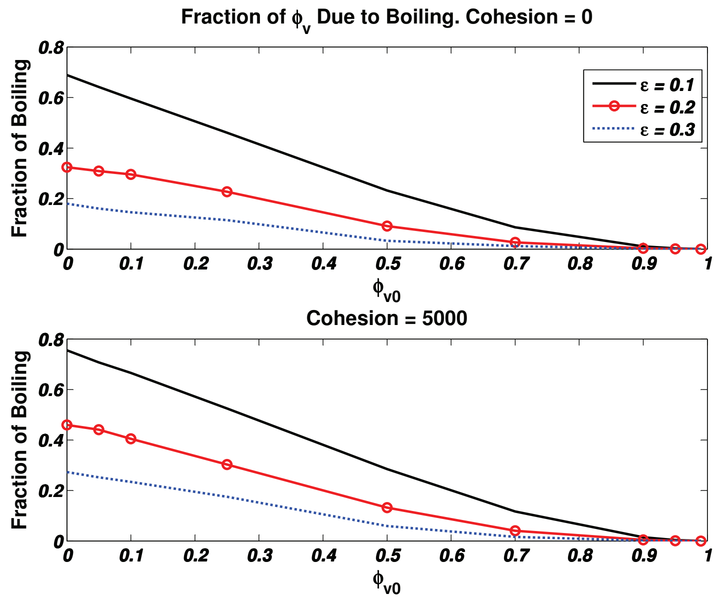

Figure 9.6: *The amount of boiling for a given* ϕ_{v0}

tions even though some eruptions can be initiated with smaller pressure differences for larger ϕ_{v0}. This is due to the lack of boiling in reservoirs with a high vapour fraction.

The initial conditions given in Table 9.1 are used as well as the permeability, $k = 10 \times 10^{-12}$. We perform the analysis for the porosity values $\epsilon = 0.2$ and cohesion $C_{pm} = 5000$. The pressure difference, ΔP, is chosen such that for all ϕ_{v0} we get initiation (see Figure 9.5). We investigate initial volume fractions $\phi_{v0}(z < 0) = 1 \times 10^{-6}, 0.1, 0.25, 0.5, 0.9, 0.99$. The upper graph of Figure 9.7 shows the distance of erosion into the geothermal reservoir. It is a plot as a function of time of the cell deepest in the geothermal reservoir where the initiation condition is satisfied. This 'mining' into the geothermal reservoir allows hotter, more energy rich fluid to be transported towards the ground surface and into the eruption jet. We see that boiling in the system is important for the erosion front to propogate into the geothermal reservoir. In fact, even though the initiation condition was initially satisfied for all ϕ_{v0}, only the simulations with 75% liquid or more continue down into the reservoir, the others are unable to continue to erode away at the porous medium. Furthermore, the smaller ϕ_{v0} (more liquid) the further down the erosion front is able to travel. The lower graph of Figure 9.7 is further evidence supporting the need for boiling. This graph plots the height above ground that the solid

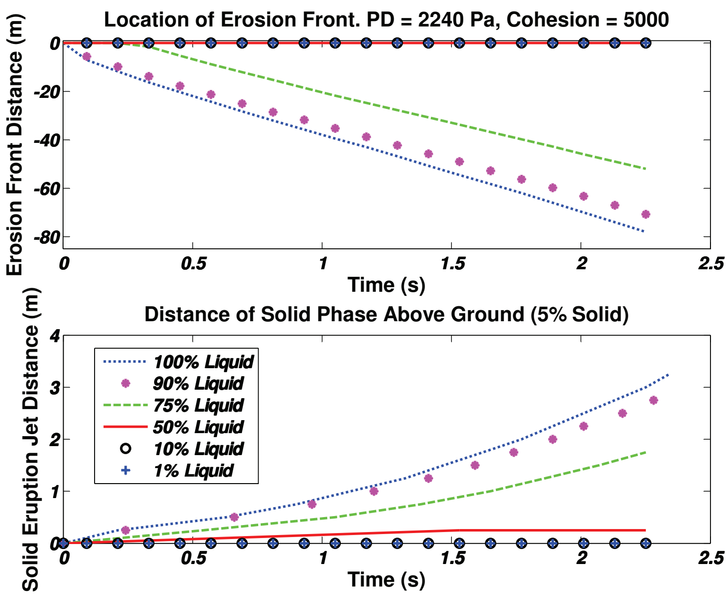

Figure 9.7: *The erosion and eruption fronts for the solid phase.*

porous medium has been ejected by the eruption. Every time step we check to find the highest cell above ground that has 5% or more volume fraction of solid phase and plot this as a function of time. Again there is little movement of the solid medium for high ϕ_{v0}, and as we increase the initial liquid saturation we increase the height/strength of an eruption. These results are evidence that boiling is the main driving force in a hydrothermal eruption. Even though a vapour filled reservoir may initiate an eruption easily, that eruption quickly dies out because there is no boiling to continue to drive the eruption. We therefore conclude, as did McKibbin [47], that the greatest potential for a hydrothermal eruption is liquid reservoir conditions.

9.2 The Effect of a Steam Cap or Cracking of the Geothermal Reservoir

It has been suggested that a 'steam cap' could increase the risk of a hydrothermal eruption in a geothemal reservoir by transmitting higher pressures to shallower regions, see [22]. This mechanism is thought to be important in exploited geothermal fields. Furthermore, rapidly forming vertical cracks in the porous medium could provide pressure differences large enough to initiate large hydrothermal eruptions. This type of cracking would have the effect of transmitting higher pressures to shallower regions. This section investigates the effect of steam caps and cracks on hydrothermal eruptions. In previous modelling of hydrothermal eruptions ([46], [47], for example) the initial reservoir conditions were assumed to be fully liquid, allowing for the largest potential for boiling. We now investigate the effect of having a 'steam cap' or a crack. A steam cap is defined by a region immediately below the ground surface that is fully steam, followed by a region that is fully liquid at some depth below the surface, see Figure 9.8. Note that the liquid and steam chambers are also filled with some porous solid with porosity ϵ. Again we use the equation set 8.1 - 8.4 and 8.7 - 8.9 and use the numerical method outlined in Section 8.2. The governing equations and assumptions of Section

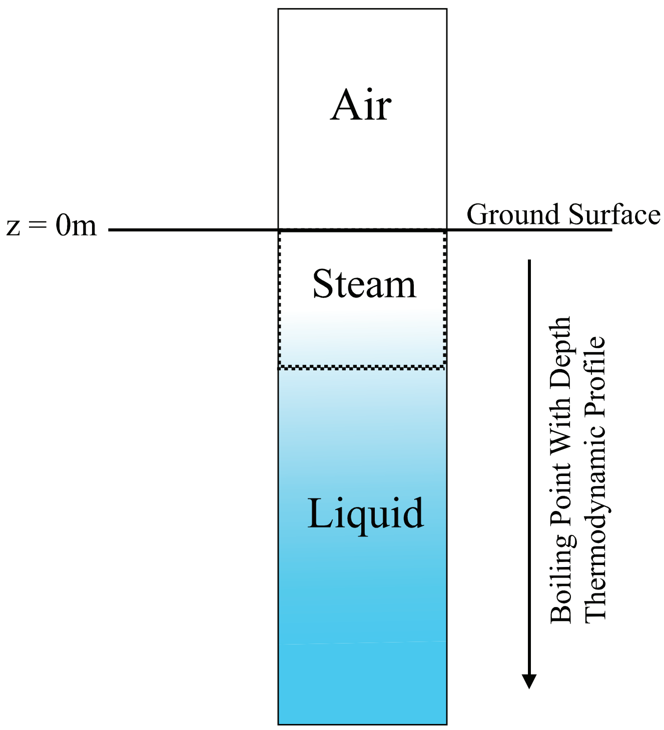

Figure 9.8: *A schematic of the shock tube model with a steam cap. In the lower part of the column we have liquid water in a porous medium, while in the upper part we have air.*

8.1 are also used to simulate a crack in a geothermal reservoir. Figure 9.9 shows the initial configuration for our simulations of cracking. In a liquid filled porous geothermal reservoir the pressure initially follows the boiling point with depth curve. The pressure at the ground surface, point B in the figure, is atmospheric and is less than the pressure at some depth A. In Figure 9.10 the reservoir quickly develops a large crack (perhaps via a small earthquake) which fills with steam. In our figure the crack reaches all the way to the surface. Note that a crack could already exist in the reservoir which could fill up with steam. In this situation some event (such as an earthquake) could enable the crack to expand, potentially all the way to the surface. The effect on the situation is this: the pressure, P_A, at point A of Figure 9.10 is transferred to point B, the ground surface. In this way, the pressure at point B is much larger than atmospheric and large pressure differences are achieved at the surface. For the sake of this thesis, the difference between

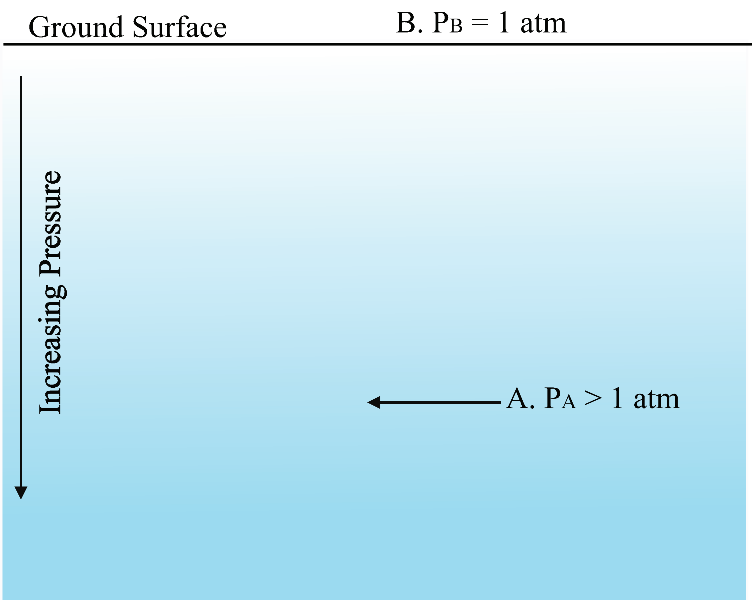

Figure 9.9: *Initially, the pressure profile in a liquid filled porous geothermal reservoir follows the boiling point with depth curve. The pressure at the ground surface (point B) is atmospheric.*

a steam cap and a cracked reservoir is formation time. A steam cap may develop slowly, over a number of days, perhaps weeks. This means that the pressure gradient in the geothermal reservoir has time to adjust to the new conditions. The initiation of a hydrothermal eruption with a steam cap is assumed to be separate from the formation of the steam cap itself. However,

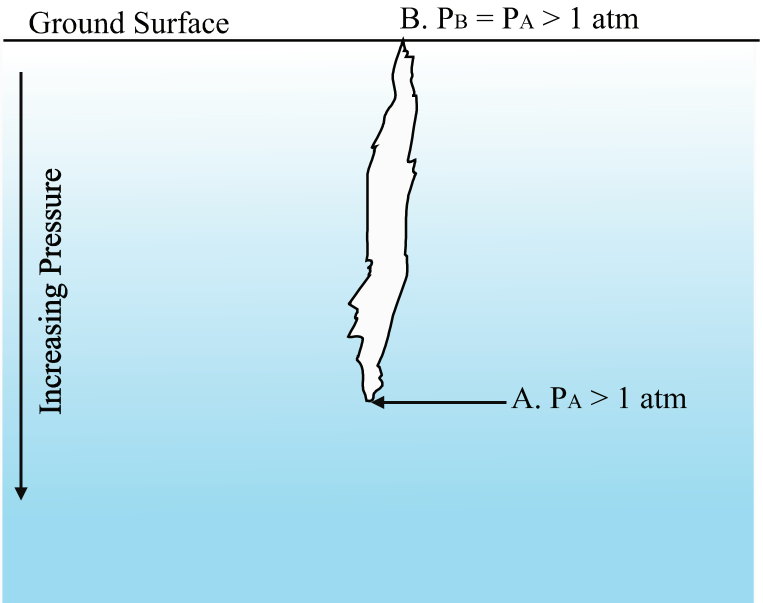

Figure 9.10: *A large vapour filled crack rapidly forms which transfers large pressures to shallow regions. The pressure at the top of the crack, the ground surface (point B), is equal to the pressure at the bottom of the crack (point A), and is greater than atmospheric.*

in the case of cracking, the cause of the eruption is the formation of the crack itself. A rapidly forming crack can transmit high pressure differences to the surface very quickly. The simulation of these two situations is similar mathematically, but the interpretation of results differs depending on which situation we find ourselves in. Note that we do not simulate the geometry of the crack itself, but rather infer the effect that a crack would have from our shock tube simulations.

9.2.1 Erosion

Equations 8.2 and 8.8 contain the terms δ and δ_s. As stated previously, these terms are to distinguish the flow profile at any time. They allow us to know whether the porous medium is part of the flow (i.e. moving with the eruption jet) or if the fluids are merely moving through the porous medium. At each timestep the initiation condition (Equation 8.35) is tested:

$$\sum_j D_j > (1-\epsilon)\rho_s g + C_{pm}.$$

If the criterion is met then we are notified and the solid phase velocity, u_s, may evolve according to the solution of the integration. However, if the initiation criterion is not met then we set the solid velocity, $u_s = 0$. This will provide us with a way of evaluating the magnitude of a given eruption, by measuring how much porous medium a given eruption can eject.

9.3 Steam Cap and Cracking Simulations

Equations 8.1 - 8.9 are solved using the numerical method of Section 8.2. Simulations of cracks and of a steam cap are done simultaneously, yet are interpreted separately. The initial conditions for simulations are given in Table 9.5. where z_v is the depth below the ground surface where the steam

Table 9.5: Test parameters

Δz (m)	0.25
Δt (s)	7.5×10^{-5}
N	780
ρ_s (kgm^{-3})	1500
$u_i(t = 0s)$ (ms^{-1})	0
$P(z = 0m)$ (Pa)	1×10^5
$T_a(z = 0m)$ (^oC)	20
R $(Jkg^{-1}K^{-1})$	287.05
c_F	0.5
$\phi_v(z_v < z < 0)$	0.999999
$\phi_v(z < z_v)$	0.000001
$\phi_l(z_v < z < 0)$	0.000001
$\phi_l(z < z_v)$	0.999999
$\phi_a(z > 0)$	0.999999
$\epsilon(z < 0)$	0.2

cap/crack meets the fully liquid reservoir. Following that given in [46], we choose a value of 5000 $\mathrm{Pa\,m^{-1}}$ for the cohesive strength of the porous medium.

9.3.1 No Steam Cap/Crack

As a first comparison, we run the simulation with no steam cap/crack, that is, $z_v = 0$. The simulation is run for an initial pressure drop across the ground/air interface of $\Delta P = 2000Pa$, $4000Pa$, $10000Pa$. Note that $2000Pa$ is the smallest pressure difference to initiate an eruption with these initial conditions for a fully liquid reservoir. See Section 9.1 for details. Figure

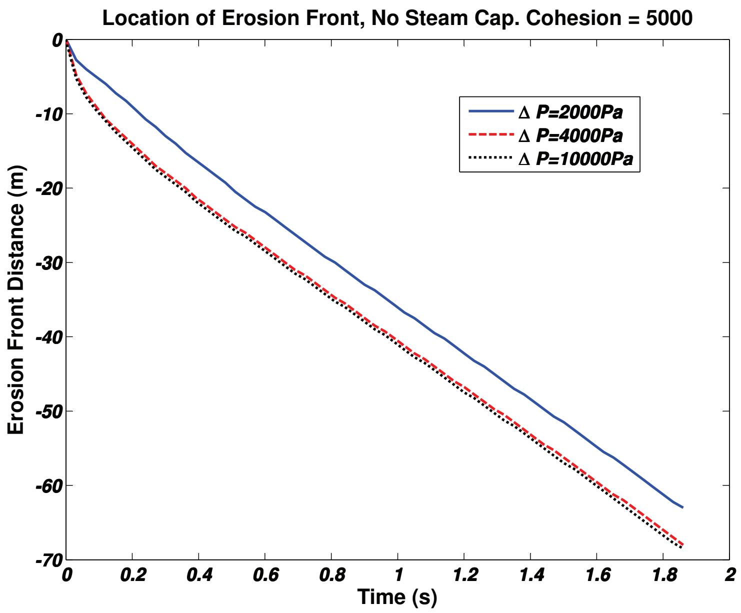

Figure 9.11: *Location of erosion front with no steam cap or crack. The front perpetually 'mines' into the geothermal reservoir.*

9.11 shows the distance the erosion front has travelled into the geothermal reservoir. Note that this figure does not represent the base of the eruption jet, rather it represents the deepest point where the initiation condition, Equation 8.35, has been met. This 'mining' of the reservoir allows rock particles to begin to be displaced and will eventually be ejected above the ground surface into an eruption jet. For the case of no steam cap/crack, that is, for fully liquid reservoir conditions, the erosion front perpetually travels into the geothermal reservoir. The expansion of liquid water to steam continually drives the eruption, as found in Section 9.1. The initial pressure difference at the surface has some effect when ΔP is close to the minimum required, but minimal effect as we increase ΔP above the critical value of pressure difference.

9.3.2 Effect of the Crack/Steam Cap for Small Pressure Differences

We repeat the simulation with new values of $z_v = 2m$, $10m$, $25m$ as representative values. We look at the case of $\Delta P = 2000Pa$, which is just enough pressure difference to initiate an eruption given fully liquid reservoir conditions. The upper graph of Figure 9.12 shows the distance that the solid phase has travelled above the ground surface in the eruption jet. The lower graph is a plot of the distance the erosion front travels into the geothermal reservoir. The lower graph is comparable to Figure 9.11. The results show,

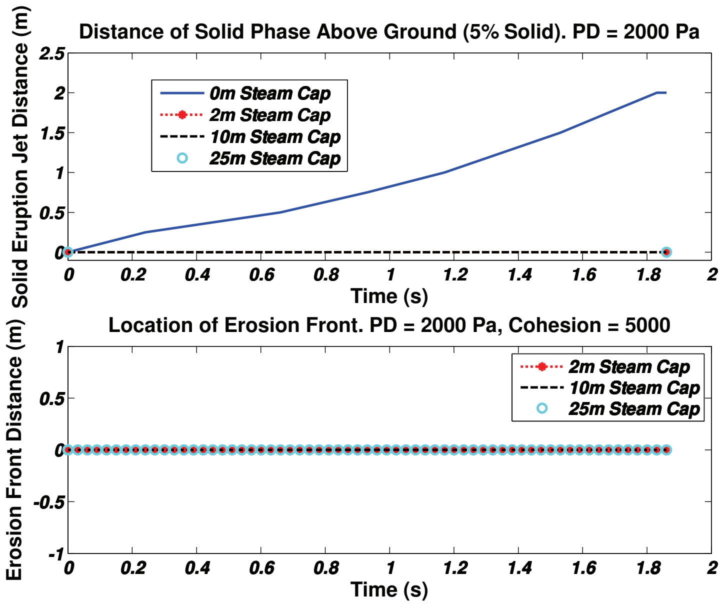

Figure 9.12: *Eruption jet and erosion front behaviour in the prescence of a steam cap or crack. For small pressure differences the eruption is stifled due to lack of boiling.*

for the pressure difference investigated, that the presence of any steam cap or crack completely stifles any eruption. There is only solid material ejected in the case of no steam cap and no erosion front forms. This is due to the lack of boiling in the steam cap zone. Boiling essentially drives a hydrothermal eruption, providing the force necessary to overcome the gravitational and cohesive strength of the rock. Hence for small pressure differences, the presence of steam destroys any eruption. On the contrary, when there is no steam cap, the upper graph shows that solid material is ejected and Figure 9.11 shows that a self perpetuating boiling front forms.

9.3.3 Effect of the Crack/Steam Cap for Larger Pressure Differences

We repeat the simulations of Section 9.3.2 but now with $\Delta P = 4000Pa$, $10000Pa$. This test aims to see the effect of increased force on the porous medium due to rapidly escaping steam from the steam cap or from the crack. Figure 9.13 shows the distance solid material has been ejected in the eruption jet for the two values of pressure difference and the various steam cap and crack sizes. Figure 9.14 is the distance the erosion front has traveled into the geothermal reservoir, as is Figure 9.15, for the various steam cap and crack sizes. The graphs of Figure 9.13 now show that for both the pressure

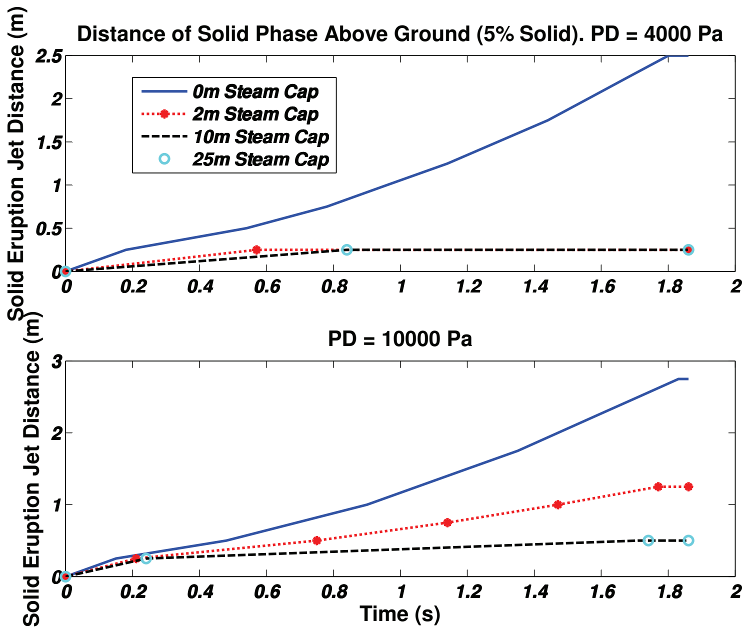

Figure 9.13: *Distance of ejection of solid material*

differences trialed, there is ejection of solid material in the eruption jet for all steam cap and crack sizes. This is due to the increased presure difference, hence force. With this increased force, the steam in the cap region is able to flow more rapidly and provide more drag force on the porous medium, hence satisfying the initiation condition. Notice that the ejection rate is still lower than that for a fully liquid filled reservoir. Notice also that in the $\Delta P = 10000Pa$ case the $2m$ steam cap or the crack are able to eject material further. Figure 9.14 shows the distance the erosion front has been

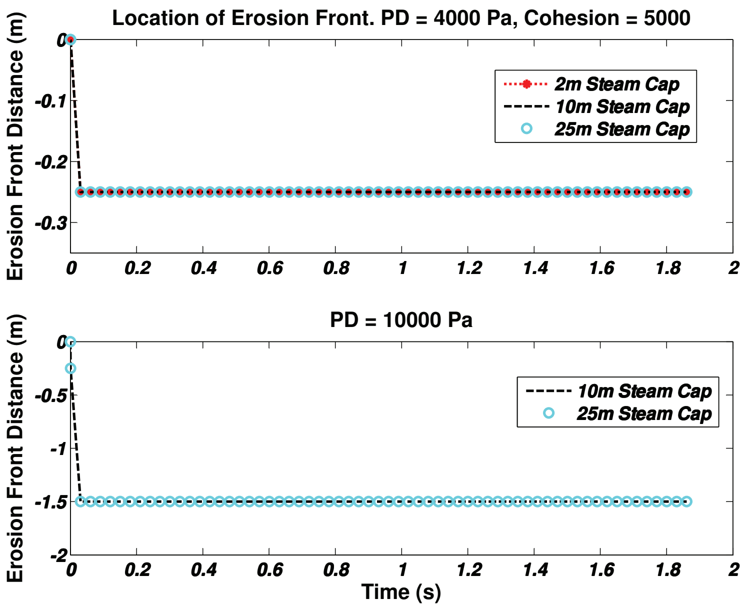

Figure 9.14: *Distance of erosion into the geothermal reservoir by steam only*

able to travel into the geothermal reservoir. Notice that the extra pressure difference has meant that there is now some mining into the reservoir by the steam. The distance travelled into the reservoir is a function of the initial pressure difference, and has a stopping distance. That is, the erosion does not continue as in the fully liquid reservoir case, but only has enough force to erode a certain distance into the reservoir. Again, this is due to the lack of boiling to continue to provide the force neccessary to drive the eruption. Note however that in the lower figure, for $\Delta P = 10000Pa$, that the $2m$ steam cap is not plotted. This is because this is the subject of Figure 9.15. Figure 9.15 shows that for $\Delta P = 10000Pa$ and steam cap or crack size of $2m$, the erosion front is able to perpetuate into the geothermal reservoir, as in the case of a fully liquid reservoir. The reason for this change in behaviour (as opposed to the erosion stopping at a certain distance as in Figure 9.14) is that the erosion front formed by the steam mining is able to meet up with the fully liquid part of the reservoir (in this case $2m$ below the ground surface) and hence, boiling of the liquid water is able to take over. This is a crucial observation; this means that for a large enough pressure difference a perpetuating erosion front may be able to form even in the presence of a steam cap or if a crack

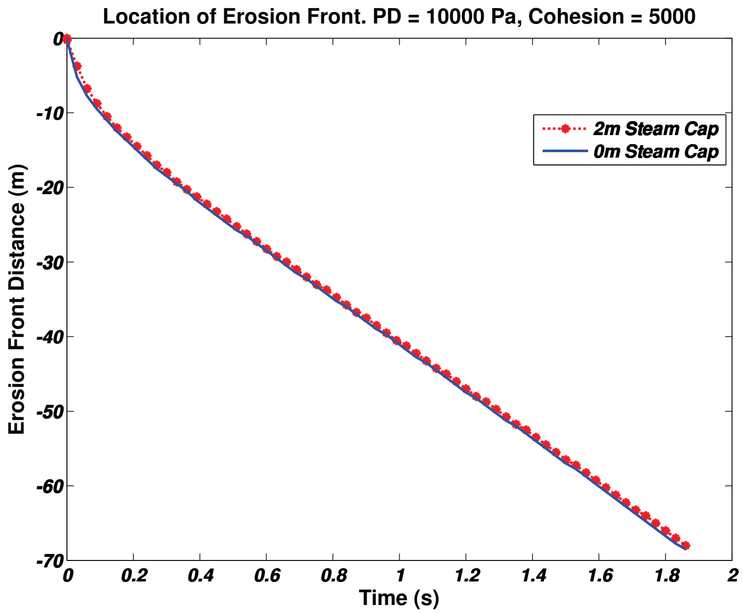

Figure 9.15: *The 2m steam cap and crack now propogates an erosion front into the geothermal reservoir.*

develops. The large size of this neccessary pressure difference means that it is unlikely that a system with a steam cap could generate enough force to perpetuate an eruption, however, a rapidly forming crack in a liquid filled reservoir would have little trouble providing this size of pressure drop. This will be the subject of investigation in the next section. Note that even though this is so, Figure 9.13 shows that fully liquid reservoir conditions still lead to larger amounts of ejected material.

9.3.4 The Maximum Amount of Steam Erosion for a Given Pressure Difference

The investigations of Section 9.3.3 showed that for increasing initial pressure difference, ΔP, the steam was able to flow quickly enough to erode down into the geothermal reservoir. However, this erosion would stop at a certain depth unless it made close contact with the liquid part of the underground reservoir, where boiling was able to take over and the erosion would continue deep into the geothermal reservoir. This test shows the maximum erosion into the geothermal reservoir that can be achieved with steam mining only. Figure 9.16 is a plot of the maximum erosion distance for a steam filled reser-

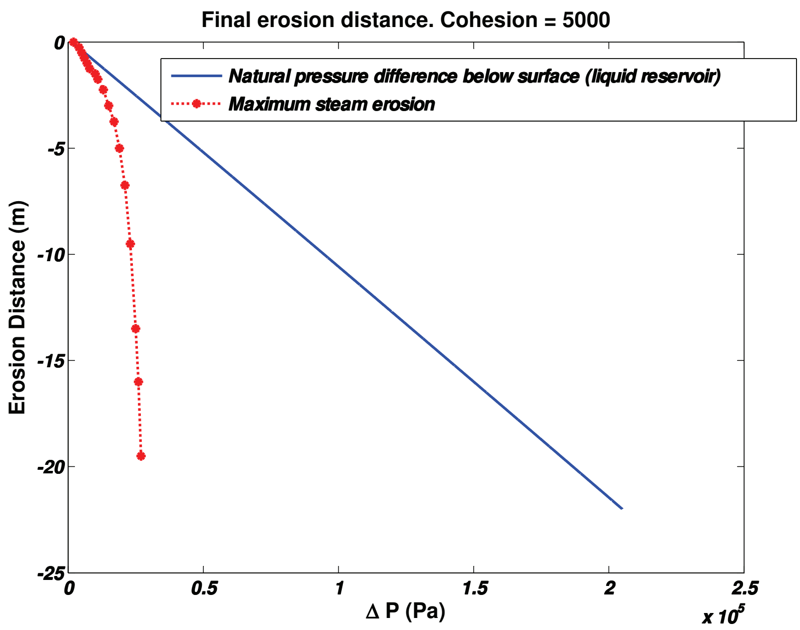

Figure 9.16: *The maximum erosion distance by steam erosion only is always less than the natural pressure difference due to liquid filled reservoir conditions.*

voir. Also plotted is the natural pressure difference of a liquid filled reservoir. This natural pressure difference is relevant in the cracking case, but not in the steam cap case. Since a steam cap develops slowly, the natural pressure difference is able to adapt. However, in the cracking case, the pressure decrease is rapid, so that there is no time for the system to come to new equilibrium. The graph shows that the pressure difference required to erode a certain distance into the geothermal reservoir by steam erosion only is always less than the natural pressure difference for a liquid filled reservoir. This is a significant result, since for a crack of any size the pressure difference required for an eruption to propagate into the geothermal reservoir as in Figure 9.15 is easily achievable due to the presence of the natural pressure difference of a liquid filled reservoir. Stated another way, the pressure difference between point A and point B in Figure 9.10 is always large enough to propagate an eruption due to cracking.

This result causes us to conclude that a steam cap type eruption is unlikely, since the large pressure differences required are unlikely to be realistic. However, in the case of rapid cracking, the pressure difference is all but guaranteed due to the natural pressure difference formed during liquid filled reservoir conditions. Therefore, we conclude that rapid cracking could potentially cause a self propogating natural hydrothermal eruption. It should be noted however that Figure 9.13 shows that even though this is a likely cause of an eruption, liquid filled reservoir conditions always produce larger eruptions for a given presure difference.

9.4 Conclusions

In this chapter simulations of the initiation of hydrothermal eruptions and the effects of steam caps and the development of rapidly forming cracks have been performed. Through our investigations in Section 9 we conclude that the geometry of the reservoir plays a key role in the pressure conditions required to initiate a hydrothermal eruption. The porosity was found to be the most important factor in determining the pressure difference required for initiation, since the slope on the log - log graph of Figure 9.1 was steeper than the slope from the log - log permeability graph of Figure 9.2. The permeability was still an important factor however, as was the cohesion of the porous medium. Furthermore, it was shown that even though it is easier to initiate an eruption in vapour dominated reservoirs, that eruption will dissipate quickly and will certainly be smaller than an eruption in a liquid dominated reservoir. In this way, we have shown that the amount of boiling is of greatest importance in a hydrothermal eruption, which is further evidence to support the progressive flashing mathematical model for a hydrothermal eruption.

In Section 9.2 we have simulated the effect of a steam cap and cracking of the porous medium. The presence of a pure steam phase in the form of a steam cap or crack was shown to significantly reduce the size of an eruption both in the above ground eruption jet and also in the below ground erosion front. We showed that the erosion front can only reach a limited depth below the ground and does not propagate further into the reservoir without a liquid phase. Importantly, we showed that if the pressure difference is great enough for the steam erosion to reach the liquid section of the reservoir (i.e small steam cap depths) then boiling of the geothermal liquid will take over at this point and the eruption will propagate. However, the pressure differences required for this to occur, even for small steam cap depths, render an eruption with a steam cap highly unlikely to propagate. The situation with rock cracking is different, however. We showed that the pressue difference required, large though it is, is less than the natural pressure difference for a liquid filled reservoir. This means that rapidly developing cracks (such as may be formed during an earthquake, or from fluidisation of the earth) could realise this required pressure difference, hence resulting in a propogating hydrothermal eruption. This cracking eruption would be smaller than a similar eruption with a liquid filled reservoir, but is still a realistic candidate for the cause of a natural hydrothermal eruption.

Chapter 10

Summary, Conclusions, and Future Work

10.1 Summary and Conclusions

Previously, all mathematical modelling work on hydrothermal eruptions has focussed on quasi-steady flow. The eruption was assumed to be already initiated, and the modelling begins sometime after this point. Furthermore, there had been no model which accounted for both above ground and below ground flow, instead there were two separate models to account for the two situations. The objective of this thesis has been to develop a model which is able to simulate the initiation of a hydrothermal eruption, thereby informing us of necessary conditions to trigger an eruption. In addition, this thesis also aimed to combine the two separate models for above and below ground flow into one unifying model. The main contributions of this thesis are:

- the development of a shock tube model able to simulate the initiation of a hydrothermal eruption including accounting for a three phase flow and flow through porous media,
- the creation of a new finite volume based numerical method which is able to simulate the advection of three fluids,
- an estimation of pressure differences needed to initiate an eruption,
- details of how the geometry of the geothermal reservoir affects the

needed pressure difference to initiate an eruption,

- the simulation of a steam cap and rapid cracking in a geothermal system.

Hydrothermal eruption phenomenon around the world and their potential hazards were introduced in Chapter 1. Chapter 2 summarised previous modelling work done on hydrothermal eruptions as well as examining the shock tube model for a volcanic eruption. This included a summary of potential causes of eruptions and a presentation of the accepted conceptual model. The basic numerical methods used to solve a shock tube type model were the subject of Chapter 3. Chapter 4 begins the new work of this thesis. This chapter introduces the governing equations for a multi-phase flow, including nozzling effects and the evolution of volume fractions of phases. A two phase numerical solver is advanced to three phases and is tested against standard simulations. In Chapter 5 the method is modified to bring the water phases back onto the boiling point with depth curve and to quantify how much boiling has occurred in a given time step, while in Chapter 6 the set of equations and the numerical method are modified to handle vertical flow. The full numerical method for a hydrothermal eruption without the presence of porous medium is also summarised in Chapter 6. In Chapter 7 simulations are performed for the initiation of a hydrothermal eruption in a liquid reservoir in the absence of porous media. The distance that the eruption jet travelled was found to be highly dependent on the initial pressure difference, but traveled much slower than the flashing front. The amount of boiling was shown to be the dominant factor in how large an eruption became. The governing equations and numerical method was then modified to include flow through a porous medium in Chapter 8. Viscous dissipation due to drag on the porous medium was included, as was the lift provided to the porous medium by the moving fluid. Nozzling due to changes in the porosity of the medium was also taken into account - an important development since this allows more realistic geometries to be explored. The full numerical method was also summarised and a 'lift off' condition was presented where the upwards forces from the flowing fluid were balanced against gravitational and cohesive forces in the porous medium. Finally, in Chapter 9, simulations are run to model a hydrothermal eruption in a porous geothermal reservoir. It was concluded that the geometry of the reservoir plays a key role in the required pressure difference to initiate a hydrothermal eruption. The porosity, permeability and the cohesion of the porous medium were found to be important parameters in determining the likelihood of an eruption. It was also shown that it is possible to initiate an eruption with lower pressure difference in vapour dominated reservoirs, but in this situation an eruption will dissipate quicker and will be smaller than an eruption in a liquid dominated reservoir. The amount of boiling was again shown to be of greatest importance in a hydrothermal eruption. Simulations of a steam cap and cracking of the porous medium were also performed. The presence of a pure steam phase in the form of a steam cap or crack was shown to significantly reduce the size of an eruption. Importantly, it was shown that if the pressure difference is great enough for the steam erosion to reach the liquid section of the reservoir an eruption will propagate further down into the reservoir. It was concluded that the pressure differences required for this to occur render a system with a steam cap highly unlikely to propagate. It was also shown that the pressue difference required to initiate an eruption through cracking of the porous medium is less than the natural pressure difference for a liquid filled reservoir. Hence it was concluded that rapidly developing cracks could result in a propogating hydrothermal eruption.

In summary, our investigations lead us to reach the following important conclusions:

- The amount of boiling is extremely important in a hydrothermal eruption. More boiling leads to larger upwards forces, hence larger eruptions. Also, boiling is essential for an eruption to propagate over longer time periods. An increase in the amount of water boiled can be achieved by larger pressure differences at the air - water interface.

- Geothermal reservoirs with high porosity, low permeability, and low cohesive soil forces are at higher risk of a hydrothermal eruption. The most influential of these is porosity.

- Liquid reservoir conditions give the greatest potential for large eruptions.
- Systems with steam caps are unlikely to experience a progressive flashing hydrothermal eruption. There are areas of the world where the underground reservoirs are vapour dominated and hydrothermal eruptions have occured. We suggest this is likely caused by some other effect such as liquefaction of the ground by pressures exceeding lithostatic.
- Systems at risk of rapid cracking (e.g. areas near earthquake fault lines) are at a higher risk of a hydrothermal eruption.

We believe that the work of this thesis significantly contributes to the knowledge of the initiation of hydrothermal eruption phenomena. This is the first mathematical model able to simulate the initiation of a hydrothermal eruption. In addition, the model is able to account for changing porosity in the geothermal reservoir via the nozzling terms.

10.2 Future Work

Some questions arising from our simulations lead to potential future work on hydrothermal eruptions. In Chapter 7 simulations showed that the flashing front travels very quickly into the reservoir. The results of Chapter 9 also show that the erosion front travels into the geothermal reservoir slower than the flashing front, yet still at a quick pace. This raises the question: if deep parts of the reservoir are being rapidly tapped, how do some eruptions last hours, even days? Is there some sort of water recharge allowing the replenishment of the liquid water for further boiling, prolonging the eruption? The next step in answering these questions involves extending the shock tube model to a 'shock tank', that is, extending the shock tube to $2D$, see Figure 10.1. Extending the model to two dimensions will allow for potential liquid water recharge, which is likely to be the main factor in long lasting eruptions. Also, a 2-D model should be able to simulate the development of any craters formed by an eruption. There are multidimensional versions of the multi phase Euler equations, so extension to the shock tube equations of this thesis should be possible but will be computationally intensive.

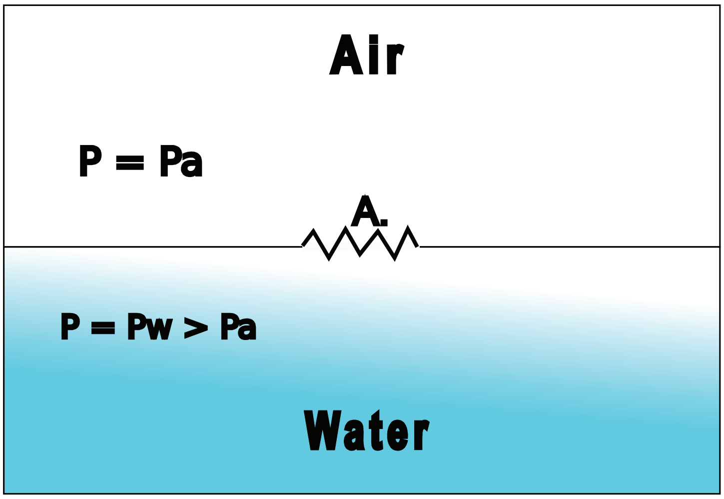

Figure 10.1: *A schematic of the shock tank setup. A large 2D liquid reservoir at boiling point conditions is separated from the atmosphere with some pressure jump $\Delta P = P_W - P_A$, $P_W > P_A$. At some weak point, A in the figure, the higher pressure liquid is exposed to the lower pressure atmosphere, triggering an eruption.*

Further work may also be done in advancing the numerical method used to solve the shock tube problem. The methods of this thesis are by design first order, since Godunov theory was used. Methods exist in literature based on MUSCL and ADER approaches which allow numerical solvers to attain higher order, see for example [72]. Extension to higher dimensions will lead to more efficient computing time (the simulations of this thesis often took a long time to run), allowing for predictions of hydrothermal eruptions at later times using the shock tube model.

Since this thesis focussed on the initiation of a hydrothermal eruption, only short time simulations were performed (i.e. < 3 sec after eruption initiation). Future work could also include longer time simulations in an effort to try to understand terminating mechanisms of an eruption. This will require accounting for air entrainment as in [49] and buoyancy terms as in [74]. Furthermore, any long time simulations would need to include heat transfer terms between the fluids and the porous medium. This would have the effect of transforming our equations from hyperbolic to parabolic, hence the numerical method would need to be modified. The current shock tube model also allows for non-homogeneous geometries, such as discontinuous porosity, by the nozzling terms. Further investigation into the effect of non-homogeneous porosity in the geothermal reservoir could lead to possible terminating mechanisms of an eruption. Imagine an erosion front traveling down into a high porosity reservoir. If this erosion front then meets an area of low porosity, it may not have enough lift force to be able to overcome the extra forces associated with the change. In this way, the eruption will begin to be strangled, and will probably terminate. It is also possible with the shock tube model, to have a situation where immediately underneath the ground surface we have liquid reservoir conditions, then at some depth d_s, we have a steam layer. This could also act to terminate an eruption, since there will be no boiling in the steam zone to drive the eruption.

Further work on simulations of cracking could incude a crack that does not extend all the way to the surface, but transmits pressures to its top which exceed lithostatic. This may cause liquefaction of the porous medium above the crack causing the medium to be effectively cohesionless. Hence the initiation condition of Equation 8.35 may be satisfied and a hydrothermal eruption may be able to break the ground surface.

Another potential source of future research is trying to simplify the shock tube model. In this thesis we had three fluids: air, steam, and liquid water. It may be possible to combine the two gas phases and simulate a two phase flow, rather than using a three phase/component solver as in this work. Any simplification will need to treat carefully the equations of state.

The most important source of future work lies in a controlled lab experiment of a hydrothermal eruption. Due to the difficulty in predicting such eruptions, no data is available about the thermodynamic state of the geothermal system just before an eruption, nor do we have any idea of the pressure drop by the tiggering mechanism of an eruption. The conclusions drawn in this thesis will need to be verified experimentally in a controlled environment. A qualitative lab experiment was performed in [70], but any new experiment will need to be quantitative so as to verify or vilify our predictions with data. Such an experiment will be difficult due to the rapid speed that the boiling and eruption fronts move through the geothermal reservoir. This was also shown in [70], where an experiment utilising NMR techniquies was attempted.

Nomenclature

ρ density, kg/m^3

u fluid velocity, m/s

P pressure, Pa

s specific entropy, $J/kg/K$

e internal energy, J

E total energy, J

T temperature, K

μ dynamic viscosity, $Pa.s$

R specific gas constant, $J/kg/K$

V_I interface velocity, m/s

v volume, m^3

P_I interface pressure, Pa

h specific enthalpy, J/kg

c speed of sound, m/s

d_p particle diameter, m

g acceleration due to gravity, m/s^2

ω interaction weight,

δ solid profile constant,

D drag term, $kg/m^2/s^2$

L lift term, $kg/m^2/s^2$

N_{ozz} nozzling term,

Ω border length,

S wave speed, m/s

$\mathbf{U}$ vector of conserved variables,

$\mathbf{F}$ vector of fluxes,

$\mathbf{F}_{LAG}$ vector of Lagrangian fluxes,

$\mathbf{Q}$ average value of $\mathbf{U}$,

$\nu = 1/\rho$ specific volume, m^3/kg

$\phi_{v,l}$ volume fraction of phase of water,

$\chi_{a,w}$ volume fraction of fluid,

$\Phi_{v,l}$ volume fraction of vapour/liquid in water phase,

ϵ porosity of the porous medium,

k permeability of the porous medium, m^2

C_{pm} cohesion of porous medium, Pa/m

c_F Ergun coefficient,

t time, s

z vertical coordinate, m

x horizontal coordinate, m

$\Delta x, \Delta z$ length of horizontal, vertical cell, m

Δt time step, s

Subscripts/Superscripts

f fluid,

v vapour phase,

l liquid phase,

a air,

w water,

s solid,

0 pertaining to time $t = 0$,

F flashing front,

E eruption jet,

$*$ middle,

L left,

R right,

sat at saturation point,

$I+$ interaction border on right side of cell,

$I-$ interaction border on left side of cell,

Bibliography

[1] National Geographic: Explorer - valley of ten thousand smokes on the Alaskan peninsula. Technical report, National Georaphic Television, videocassette, 1994.

[2] W. T. Lee A. C. Fowler, Bettina Scheu and M. J. McGuinness. A theoretical model of the explosive fragmentation of vesicular magma. *Proc. R. Soc. A*, 466:731–752, 2009.

[3] R. Abgrall and V. Perrier. Asymptotic expansion of a multiscale numerical scheme for compressible multiphase flows. *SIAM Journal on Multiscale Modeling and Simulation*, 5:84–115, 2006.

[4] R. Abgrall and R. Saurel. Discrete equations for physical and numerical compressible multiphase mixtures. *Journal of Computational Physics*, 186:361–396, 2003.

[5] M. Alidibirov and D.B. Dingwell. Three fragmentation mechanisms for highly viscous magma under rapid decompression. *Journal of Volcanology and Geothermal Research*, 100:413–421, 2000.

[6] R.A. Allis. Thermal history of the Karapiti area, Wairakei. Technical report, Report 137, DSIR Geophysics Division, 1979.

[7] R.A. Allis. The 9th april 1983 steam eruption at Craters of the Moon thermal area, Wairakei. Technical report, Report 196, DSIR Geophysics Division, 1983.

[8] N. Andrianov, R. Saurel, and G. Warnecke. A simple method for compressible multiphase mixtures and interfaces. *International Journal for Numerical Methods in Fluids*, 41:109–131, 2003.

[9] M.R. Baer and J.W. Nunziato. A two-phase mixture theory for the deflagration-to-detonation transition (DDT) in reactive granular materials. *International Journal of Multiphase Flow*, 12:861–889, 1986.

[10] Hon. R. Barker. Natural hazards 2006. Technical report, NIWA and GNS, 2006.

[11] Hon. R. Barker. Natural hazards 2007. Technical report, NIWA and GNS, 2007.

[12] P. Batten, N. Clarke, C. Lambert, and D.M. Causon. On the choice of wavespeeds for the HLLC Riemann solver. *SIAM Journal of Scientific Computing*, 18 (6):1553–1570, 1997.

[13] J.B. Bdzil, R. Menikoff, S.F. Son, A.K. Kapila, and D.S. Stewart. Two-phase modeling of deflagration-to-detonation transition in granular materials: A critical examination of modeling issues. *Physics of Fluids*, 11 (2):378–402, 1999.

[14] B.J. Bercich. Mathematical modelling of natural hydrothermal eruptions. Report, Department of Engineering Science, School of Engineering, University of Auckland, September 1990.

[15] P.F. Bixley and P.R.L. Browne. Hydrothermal eruption potential in geothermal development. In *Conference Proceedings: (10th) New Zealand Geothermal Workshop 1988, pp. 195-198*. University of Auckland, 2006.

[16] C.E. Brennen. *Fundamentals of Multiphase Flow*. Cambridge University Press, 2005.

[17] P.R.L. Browne and J.V. Lawless. Characteristics of hydrothermal eruptions, with examples from New Zealand and elsewhere. In *Earth-Science Reviews*, pages 299–331. Elsevier Science B.V, 2001.

[18] J.A. Burgos C.A.E. Bruno and S. Ayala. Agua Shuca hydrothermal eruption. *Geothermal Resources Council Bulletin*, 21:361–369, 1992.

[19] C.E. Castro and E.F. Toro. Godunov schemes for compressible multiphase flows. In *European Conference on Computational Fluid Dynamics*, 2006.

[20] C.H. Chang and M.S. Liou. A robust and accurate approach to computing compressible multiphase flow: Stratified flow model and AUSM+ -up scheme. *Journal of Computational Physics*, 225:840–873, 2007.

[21] C.J. Chapman. *High Speed Flow.* Cambridge University Press, 2000.

[22] R.L. Christiansen. Preliminary assessment of volcanic and hydrothermal hazards in Yellowstone National Park and vicinity. Technical report, USGS, 2007.

[23] M.T. Cochran and J.M. Powers. Computation of compaction in compressible granular material. *Mechanics Research Communications*, 35:96–103, 2008.

[24] R.J. Collar. Hydrothermal eruptions in the Rotokawa Geothermal System, Taupo Volcanic Zone, New Zealand. Technical report, Report GIR 14, Geothermal Institute, University of Auckland, 1985.

[25] V. Deledicque and M.V. Papalexandris. An exact riemann solver for compressible two-phase flow models containing non-conservative products. *Journal of Computational Physics*, 222:217–245, 2007.

[26] M. Drela, A. Merchant, and J. Peraire. Elimination of spurious loss in Euler equation computations. *AIAA JOURNAL*, 38 (3):411–417, 2000.

[27] D.A. Drew. Mathematical modeling of two-phase flow. *Annual Reviews in Fluid Mechanics*, 15:261–291, 1983.

[28] E.D. Fernandez-Nieto, D. Bresch, and J. Monnier. A consistent intermediate wave speed for a well-balanced HLLC solver. *Comptes Rendus Mathematique*, 346:795–800, 2008.

[29] F.G. Ghangir, A.F. Nowakowski, F.C.G.A. Nicolleau, and T.M. Michelitsch. The application of HLLC numerical solver to the reduced multiphase model. *Proceeding of the World Academy of Science, Engineering anf Technology*, 30:302–308, 2008.

[30] S.K. Godunov. A difference method for numerical calculation of discontinuous solutions of the equations of hydrodynamics. *Mat. Sb. (N.S.)*, 47 (89):271–306, 1959.

[31] K.A. Gonthier and J.M. Powers. A high-resolution numerical method for a two-phase model of deflagration-to-detonation transition. *Journal of Computational Physics*, 163:376–433, 2000.

[32] J. W. Hedenquist and R. W. Henley. Hydrothermal eruptions in the Waiotapu geothermal system, New Zealand: Their origin, associated breccias and relation to precious metal mineralization. *Economic Geology*, 80:1640–1668, 1985.

[33] B F Houghton and I A Nairn. The 1976 - 1982 strombolian and phreatomagmatic eruptions of White Island, New Zealand: eruptive and depositional mechanisms at a 'wet' volcano. *Bulletin of Volcanology*, 54:25–49, 1991.

[34] A.W. Hurst J. Vandemeulebrouck and B.j. Scott. The effects of hydrothermal eruptions and a tectonic earthquake on a cycling crater lake (Inferno Crater Lake, Waimangu, New Zealand). *Journal of Volcanology and Geothermal Research*, 178:271–275, 2008.

[35] D.E. White J.P.J. Muffler and A.H. Truesdell. Hydrothermal explosion craters in Yellowstone National Park. *Geological Society of America Bulletin*, 82:723–740, 1971.

[36] T. Koyaguchi and N.K. Mitani. An analysis of volcanic explosions on the basis of the shock-tube model. Technical report, Kyoto University, 2004.

[37] T. Koyaguchi and N.K. Mitani. A theoretical model for fragmentation of viscous bubbly magmas in shock tubes. *Journal of Geophysical Research*, 110:1–21, 2005.

[38] G. Chiodini R. Cioni M. Fytikas L. Marini, C. Principe and G. Marinelli. Hydrothermal eruptions of Nisyros (Dodecanese, Greece). past events

and present hazard. *Journal of Volcanology and Geothermal Research*, 56:71–94, 1993.

[39] M.H. Lallemand and R. Saurel. Pressure relaxation procedures for multiphase compressible flows. Technical report, INRIA, 2000.

[40] R.J. LeVeque. *Finite Volume Methods for Hyperbolic Problems.* Cambridge University Press, 2002.

[41] M.S. Liou, L. Nguyen, T.G. Theofanous, and C.H. Chang. How to solve compressible multifluid equations: a simple, robust and accurate method. *AIAA Journal*, 46 (9):2345–2356, 2008.

[42] E. F. Lloyd. The hot springs and hydrothermal eruptions of Waiotapu. *New Zealand Journal of Geology and Geophysics*, 2:141–176, 1959.

[43] E.F. Lloyd and R.F. Keam. Trinity Terrace hydrothermal eruption, Waimangu, New Zealand. *New Zealand Journal of Science*, 17:511–528, 1974.

[44] K.M. Luketina. The history and application of geyser theory. Technical report, Post-Graduate Diploma of Science Dissertation, Auckland University, 1996.

[45] L.G. Mastin. Thermodynamics of gas and steam-blast eruptions. *Bulletin of Volcanology*, 57:85–98, 1995.

[46] R. McKibbin. An attempt at modelling hydrothermal eruptions. In *Proceedings of the 11th New Zealand Geothermal Workshop 1989*, pages 267–273. University of Auckland, 1989.

[47] R. McKibbin. Could non-condensible gases affect hydrothermal eruptions? In *Conference Proceedings: (18th) New Zealand Geothermal Workshop, November 1996.* University of Auckland, 1996.

[48] R. McKibbin. Modelling deposition of hydrothermal eruption ejecta. In *Conference Proceedings: (28th) New Zealand Geothermal Workshop & NZGA seminar, 15-17 November 2006.* University of Auckland, 2006.

[49] R. McKibbin and T.A. Smith. Hydrothermal eruption jets: Air entrainment and cooling. In *Conference Proceedings: (28th) New Zealand Geothermal Workshop & NZGA seminar, 15-17 November 2006*. University of Auckland, 2006.

[50] R. McKibbin, T.A. Smith, and L. Fullard. Components and phases: Modelling progressive hydrothermal eruptions. *The ANZIAM Journal*, 50:365–380, 2009.

[51] T. Miyoshi and K. Kusano. A multi-state HLL approximate Riemann solver for ideal magnetohydrodynamics. *Journal of Computational Physics*, 208:315–344, 2005.

[52] S.T. Munkejord and M. Papin. The effect of interfacial pressure in the discrete-equation multiphase model. *Computers and Fluids*, 36:742–757, 2007.

[53] A. Namiki and M. Manga. Response of a bubble bearing viscoelastic fluid to rapid decompression: Implications for explosive volcanic eruptions. *Earth and Planetary Science Letters*, 236:269–284, 2005.

[54] C.E. Nelson and D.L. Giles. Hydrothermal eruption mechanisms and hot spring gold deposits. *Economic Geology*, 80:1633–1639, 1985.

[55] G.A. Pinhasi, A. Ullmann, and A. Dayan. 1D plane numerical model for boiling liquid expanding vapor explosion (BLEVE). *International Journal of Heat and Mass Transfer*, 50:4780–4795, 2007.

[56] J.M. Powers. Two-phase viscous modeling of compaction of granular materials. *Physics of Fluids*, 16 (8):2975–2990, 2004.

[57] L. Qiang, F. Jian-hu, C. Ti-min, and H. Chun-bo. Difference scheme for two-phase flow. *Applied Mathematics and Mechanics*, 25:536–545, 2004.

[58] C.G. Cunningham R.O. Fournier, J. M. Thompson and R.A. Hutchinson. Conditions leading to a recent small hydrothermal explosion at Yellowstone National Park. *Geological Society of America Bulletin*, 103:1114–1120, 1991.

[59] R. Robert and C. Rosier. Long range predictability of atmospheric flows. *Nonlinear Processes in Geophysics*, 8:55–67, 2001.

[60] D. Rochette and S. Clain. Two-dimensional computation of gas flow in a porous bed characterized by a porosity jump. *Journal of Computational Physics*, 219:104–119, 2006.

[61] P.L. Roe. Approximate Riemann solvers, parameter vectors, and difference schemes. *Journal of Computational Physics*, 43 (2):357–372, 1981.

[62] G.F.C. Rogers and Y.R. Mayhew. Thermodynamic and transport properties of fluids. Technical report, Basil Blackwell Publisher, 1983.

[63] B. J. Scott S. F. Simmons, M. Keywood and R. F. Keam. Irreversible change of the Rotomahana-Waimangu hydrothermal system (New Zealand) as a consequence of a volcanic eruption. *Geology*, 21:643–646, 1993.

[64] R. Saurel and R. Abgrall. A multiphase Godunov method for compressible multifluid and multiphase flows. *Journal of Computational Physics*, 150:425–467, 1999.

[65] R. Saurel and O. Lemetayer. A multiphase model for cmpressible flows with interfaces, shocks, detonation waves and cavitation. *Journal of Fluid Mechanics*, 431:239–271, 2001.

[66] R. Saurel, F Petitpas, and R. Abgrall. Modelling phase transition in metastable liquids: Application to cavitating and flashing flows. *Journal of Fluid Mechanics*, 607:313–350, 2008.

[67] B.J. Scott. Calorimetry and hydrothermal eruptions, Waimangu hydrothermal field, 1971 - 1990. In *Proceedings of the 14th New Zealand Geothermal Workshop 1992*, pages 247–251. University of Auckland, 1992.

[68] B.J. Scott and A.D. Cody. The 20 june 1981 hydrothermal explosion at Tauhara geothermal field, Taupo. Technical report, Report 103, DSIR Report NZGS, 1982.

[69] G.E. Sigvaldason. Recent hydrothermal explosion craters in an old hyaloclastite flow, central Iceland. *Journal of Volcanology and Geothermal Research*, 54:53–63, 1992.

[70] T.A. Smith. *Mathematical modelling of underground flow processes in hydrothermal eruptions.* PhD thesis, Massey University, Palmerston North, New Zealand, 2000.

[71] T.A. Smith and R. McKibbin. An investigation of boiling processes in hydrothermal eruptions. In *Proceedings of the 21st New Zealand Geothermal Workshop 1999*, pages 699–704. University of Auckland, 1999.

[72] E.F. Toro. *Riemann Solvers and Numerical Methods for Fluid Dynamics: A Practical Introduction.* Springer-Verlag Telos, 1997.

[73] E.F. Toro, M. Spruce, and W. Speares. Restoration of the contact surface in the HLL-Riemann solver. *Shock Waves*, 4:25–34, 1994.

[74] J.S. Turner. Buoyant plumes and thermals. *Annual Review of Fluid Mechanics*, 1:29–44, 1969.

[75] A.W. Vreman. Macroscopic theory of multicomponent flows: Irreversibility and well-posed equations. *PHYSICA D-NONLINEAR PHENOMENA*, 225:94–111, 2007.

[76] G.J. Weir, R.M. Young, and P.N. McGavin. A simple model for Geyser Flat, Whakarewarewa. *Geothermics*, 21:281–304, 1992.

[77] D.L. Lopez M.J. Carr W.I. Rose, J.J. Bommer and J.J. Major. *Natural Hazards in El Salvador.* The Geological Society of America, Boulder, Colorado, 2004.

[78] K.H. Wohletz, T.R. McGetchin, M.T. Sandford II, and E.M. Jones. Hydrodynamic aspects of caldera-forming eruptions: Numerical models. *Journal of Geophysical Research*, 89:8269–8285, 1984.

[79] K.H. Wohletz and G.A. Valentine. Computer simulations of explosive volcanic eruptions. Technical report, Earth and Environmental Sciences Division, Los Alamos National Laboratory, 1990.